TAMPEREEN TEKNILLINEN YLIOPISTO
TAMPERE UNIVERSITY OF TECHNOLOGY

MARKKU YLÖNEN

CAVITATION EROSION CHARACTERIZATION OF A FRANCIS TURBINE RUNNER BLADE MATERIAL

Master of Science Thesis

Examiners: Professor Pentti Saarenrinne and Docent Juha Miettinen
Examiners and topic approved by the Faculty Council of the Faculty of Natural Sciences
on 7th October 2015

ABSTRACT

Markku Ylönen: Cavitation Erosion Characterization of Francis Turbine Runner Blade Material
Tampere University of Technology
Master of Science Thesis, 116 pages, 2 Appendix pages
March 2016
Master's Degree Program in Environmental and Energy Engineering
Major: Power Plant and Combustion Engineering
Examiners: Professor Pentti Saarenrinne and Docent Juha Miettinen

Keywords: cavitation erosion, acoustic emission, cavitation detection, material cavitation resistance, Francis turbine

In this study, the cavitation erosion resistance was characterized for a steel type used in Francis turbine runner blades. The goal of the study was to define the cavitation erosion rate of the runner blade steel and to compare the results to those of previously studied materials. The previously studied materials were aluminium alloy 7075, nickel aluminium bronze alloy C95400 and stainless steels A2205 and 304L. The material was tested in a cavitation tunnel in which sheet and cloud cavitation appears in the test section. Acoustic emission signal was measured from the sample experiencing cavitation erosion.

Cavitation erosion can be divided into four distinct stages; the incubation period, the acceleration period, the deceleration period and the steady state period. Each of these periods is connected to the material response of a sample in a cavitation field. The material response is linked to the stage of work hardening and material cavity formation, as cavitation modifies the material surface. The cavitation tunnel used in this study circulates water and it has variable upstream and downstream pressures. The test section is a radially diverging channel in which cavitation inception occurs in the beginning of the radial section and cavitation closure occurs several millimeters downstream. The sample was cylindrical with one face experiencing cavitation.

The cavitation erosion evolution was measured with a contact profilometer. The volume loss and the maximum depth of penetration were calculated from the surface profiles and they were compared to results from other materials. The acoustic emission results were compared with the erosion evolution. Material characteristics were obtained by elemental analysis, by macroscopic compression tests, by nanoindentation tests and by split Hopkinson pressure bar tests.

The results show that the studied steel is as resistant to cavitation erosion as aluminium alloy 7075 and less resistant to cavitation erosion than nickel aluminium bronze alloy C95400 and stainless steels A2205 and 304L. The reason for the lower resistance compared to the stainless steels is corrosion, lower quality level or both. The voltage root mean square value of the acoustic emission signal reduced with increasing cumulative erosion time. Acoustic emission monitoring was found to be a potential method in estimating cavitation erosion evolution in hydraulic machines.

TIIVISTELMÄ

Markku Ylönen: Kavitaatioeroosion karakterisointi Francis-turbiinin juoksupyörän materiaalille
Tampereen teknillinen yliopisto
Diplomityö, 116 sivua, 2 liitesivua
Maaliskuu 2016
Ympäristö- ja energiatekniikan diplomi-insinöörin koulutusohjelma
Pääaine: Voimalaitos- ja polttotekniikka
Tarkastajat: professori Pentti Saarenrinne ja dosentti Juha Miettinen

Avainsanat: kavitaatioeroosio, akustinen emissio, kavitaation havaitseminen, materiaalin kavitaatiokestävyys, Francis-turbiinin juoksupyörä

Tässä työssä tutkittiin Francis-turbiinin juoksupyörän siivessä käytettävän terästyypin kavitaatiokestävyyttä. Työn tavoitteena oli tutkia materiaalin eroosionopeutta sekä verrata sitä aiemmin tutkittuihin materiaaleihin. Aiemmin tutkitut materiaalit olivat alumiiniseos 7075, nikkeli alumiini pronssiseos C95400 sekä ruostumattomat teräkset A2205 ja 304L. Materiaalia tutkittiin kavitaatiotunnelissa joka tuottaa taso- sekä pilvimäistä kavitaatiota testausosiossaan. Näytekappaleesta mitattiin akustista emissiota kun se oli kavitaatioeroosion vaikutuksen alaisena.

Kavitaatioeroosiolla on neljä toisistaan erotettavaa vaihetta: alkuvaihe, kiihtymisvaihe, hidastumisvaihe sekä tasaisen eroosionopeuden vaihe. Jokainen vaihe on yhteydessä materiaalin kavitaatiovasteeseen. Tämä vaste on yhteydessä materiaalin muokkauslujittumisen sekä onkaloiden syntymisen tasoihin, koska kavitaatio muokkaa materiaalin pintaa. Tutkimuksessa käytetty kavitaatiotunneli kierrättää vettä ja sen ylä- sekä alavirran paineita voidaan muuttaa. Testausosio on radiaalisesti laajeneva kanava, jossa kavitaatio syntyy radiaalisen osion alussa ja romahtaa muutaman millimetrin päässä alavirtaan. Näytekappale oli sylinterimäinen ja sen yksi sivu altistui kavitaatioeroosiolle.

Kavitaatioeroosion eteneminen mitattiin kontaktiprofilometrillä. Pintaprofiileista laskettiin tilavuushäviö sekä suurin eroosiosyvyys ja näitä tuloksia verrattiin toisten materiaalien vastaaviin tuloksiin. Akustisen emission mittaustuloksia verrattiin eroosion kehittymiseen. Materiaalin ominaisuudet selvitettiin alkuaineanalyysillä, makroskooppisilla puristustesteillä, nanoindentaatiolla sekä split Hopkinson pressure bar -testeillä.

Tulokset osoittavat, että tutkittu teräslaatu on kavitaatiokestävyydeltään yhtä hyvä kuin alumiiniseos 7075, mutta huonompi kuin nikkeli alumiini pronssiseos C95400 tai ruostumattomat teräkset A2205 sekä 304L. Syy ruostumatonta terästä heikompaan kestävyyteen on joko korroosiossa, matalammassa laatutasossa tai molemmissa. Akustisen emission signaalin ulostulojännitteen neliöllisen keskiarvon kokonaiskeskiarvon havaittiin laskevan kavitaatioeroosion edetessä. Tämän havainnon vuoksi akustisen emission arvioitiin olevan potentiaalinen menetelmä hydraulisten koneiden kavitaatioeroosion vaiheiden tunnistamiseen.

PREFACE

This Master of Science thesis was written as a part of a larger project called “Nopeutettu elinkaaren määritys” or “Accelerated life cycle estimation”. The project was managed by Tampere University of Technology with Professor Pentti Saarenrinne and Docent Juha Miettinen as the responsible persons. The project was funded by Tekes – the Finnish Funding Agency for Technology and Innovation, by companies and by Tampere University of Technology. The companies that funded the project are: Fortum Power and Heat Oy, Sandvik Mining and Constructions Oy, Teollisuuden Voima Oyj and Valtra Oy Ab. Neurovision Oy and Oliotalo Oy supported the project with knowledge and technology.

The work in this thesis was carried out with a significant collaboration with the French National Center for Scientific Research (CNRS). The author did all the experiments linked to this thesis in the LEGI (Laboratoire des Ecoulements Géophysiques et Industriels) and the SIMaP (Science et Ingénierie des Matériaux et Procédés) laboratories in Saint-Martin d’Hères, France.

I want to thank Professor Pentti Saarenrinne and Docent Juha Miettinen for trusting me enough to hire me for the project and for their help and support in the process of completing my thesis. I want to thank Jean-Pierre Franc, the director of research of LEGI and Marc Fivel, the director of research of SIMaP-GPM2 for their invaluable aid and support in the scientific content of my research. Especially I want to thank Michel Riondet, the technical engineer responsible for the test setup, for the practical every day aid in using and understanding the cavitation tunnel used in this study.

I also want to thank all the funders of the project and especially Fortum Power and Heat Oy for providing the interesting research topic. I want to thank my colleagues in LEGI for the everyday scientific and non-scientific communication we had. My special thanks go to my future wife Jenni Niska, who carried me through the exhausting process of finishing my thesis.

Saint Martin d’Hères, France, 24.2.2016

Markku Ylönen

CONTENTS

LIST OF FIGURES AND TABLES

LIST OF SYMBOLS AND ABBREVIATIONS

A	Area
A'	Amplitude
$A(h)$	Projected contact area in function of height
C	Strain rate dependency constant
c	Wave velocity
C_L	Longitudinal wave velocity
c_L	Speed of sound in a liquid
C_R	Rayleigh wave velocity
C_T	Transverse wave velocity
D	Pit diameter
d	Displacement in compression or traction testing
d_{nozzle}	Nozzle diameter
D^*	Characteristic pit diameter
$\overline{D}$	Normalized pit diameter
$\underline{d}, \underline{p}$	Unit vectors for wave movement direction
$\frac{d}{dR}$	First derivative in respect to radius
$\frac{d}{dt}$	First derivative in respect to time
E	Young’s modulus
E_r	Reduced Young’s modulus
E_{ind}	Indenter Young’s modulus
$\dot{E}$	Steady state erosion rate
F	Force
f	Frequency
Fr	Felicity ratio
f_s	Shedding frequency
g	Gravitation acceleration for free fall
H	Hydraulic head
h	Height
H_{ro}	Runner outlet hydraulic head
H_T	Total head over a hydraulic machine
H_{ti}	Turbine inlet hydraulic head
$\underline{h_k}$	Erosion depth vector
ΔH	Head loss
ΔH_{o-d}	Head loss between runner outlet and downstream setting level
i, j, k	Indexes
K	Spring stiffness per unit area
k_w	Weibull distribution shape parameter
K'	Strain hardening constant
k'	Erosion rate-incubation time dependency constant
L	Sample height
l_c	Sheet cavity length
L_H	Maximum hardened layer thickness
l_H	Hardened layer thickness
L_0	Initial sample height
m	Mass per unit area

N	Pitting rate
n	Strain hardening exponent
N_{tot}	Total amount of measurement points
n_V	Amount of signal measurement points
$N*$	Characteristic pitting rate
$\bar{N}$	Normalized pitting rate
P	Pressure
P_{AE}	Structure loading when acoustic emission is observed
P_c	Critical pressure
P_D	Downstream setting pressure
P_g	Gas pressure
P_{g0}	Initial gas pressure
$P_{initial}$	Initial structure loading
P_{ro}	Runner outlet pressure
P_l	Liquid pressure
P_{peak}	Bubble collapse peak pressure
P_{ti}	Turbine inlet pressure
P_v	Saturated vapour pressure
P_∞	Reference pressure
ΔP	Pressure difference
r	Radius
r_c	Critical bubble radius
r_0	Bubble initial radius
Δr	Radial resolution
S	Nanoindentation curve fit parameter
S_c	Contact area
$S_{c,0}$	Initial contact area
S_{st}	Structure length
$S_{st,0}$	Initial structure length
St	Strouhal number
ΔS	Structure length difference
t	Time
T_i	Incubation period duration
$t*$	Characteristic time in volume loss
$t'*$	Non-dimensional time in re-entrant jet formation
$\bar{t}$	Normalized time
Δt	Time difference
$\underline{u}$	Displacement vector
$\underline{\ddot{u}}$	Acceleration vector
V	Velocity
V_D	Downstream setting velocity
V_{def}	Deformation velocity
V_{ro}	Runner outlet velocity
V_t	Test section flow velocity
V_{ti}	Turbine inlet velocity
V_∞	Reference velocity
V_{loss}	Volume loss
V_i	Signal output voltage
V_{RMS}	Root mean square voltage

V^*_{loss}	Characteristic volume loss
$\overline{V_{loss}}$	Normalized volume loss
x	General location variable
$\dot{x}$	First time derivative of displacement i.e. velocity
$\underline{x}$	Position vector
Δx	Profilometer x-resolution
y	General height variable
Y_D	Downstream setting level
Y_{ro}	Runner outlet level
y_{radial}	Test section height
Y_{ti}	Turbine inlet level
Δy	Profilometer y-resolution
Z	Cavitation bubble stand-off distance
z	General depth variable
Z_s	Normalized bubble stand-off distance
z_0	Reference depth
r_{max}	Maximum radius of a cavitation bubble

α	Exponent obtained from cavitation and liquid impingement data
β	Angle for sample orientation
γ	Surface tension parameter
ε	Strain
ε_p	Plastic strain
ε_s	Surface strain
ε_{true}	True strain
$\dot{\varepsilon}$	Strain rate
$\dot{\varepsilon}_0$	Reference strain rate
θ	Strain hardening profile shape factor
λ, μ_L	Lame’s elastic constants
v	Poisson’s ratio
v_{ind}	Indenter Poisson’s ratio
ρ	Density
ρ_g	Gas density
ρ_l	Liquid density
σ	Stress
σ_c	Cavitation number
σ_m	Mean amplitude of impact stresses
σ_T	Thoma number
σ_{true}	True stress
σ_{T0}	Critical Thoma number
σ_U	Ultimate stress
σ_y	Yield stress
$\sigma_{y,ref}$	Reference yield stress
τ	Coverage time

∇	Gradient operator
∇^2	Laplace operator
AE	Acoustic emission
FEM	Finite element method
FFT	Fast Fourier transform
MDPR	Mean depth of penetration rate
NPSH	Net positive suction head
$NPSH_{ro}$	Runner outlet net positive suction head
PIV	Particle image velocimetry
PREVERO	Cavitation tunnel name: prévision de l’érosion
PZT	Piezoelectric
RMS	Root mean square
SHPB	Split Hopkinson pressure bar

1. INTRODUCTION

Liquid evaporation due to pressure drop in constant temperature is called cavitation. Cavitation may be observed either in a static or in a flowing liquid. The equilibrium pressure where as much liquid evaporates as gas condenses is called the saturated vapour pressure, which is often considered as the critical pressure limit for cavitation. The limit is not always saturated vapour pressure, as the liquid nuclei content has an effect on the liquid vaporisation. In a liquid flow, the flow static pressure may drop below the critical pressure for cavitation due to changes in flow geometry or due to flow vorticity. Cavitation bubbles forming in a liquid flow collapse when the flow static pressure recovers to a value higher than the critical pressure.

Collapsing cavitation bubbles produce pressure peaks and they may damage wall material, if the collapse happens close enough to the wall. Cavitation erosion is an important erosion mechanism in hydraulic machinery. In a Francis turbine, the runner blades experience cavitation erosion, especially when the turbine is operated outside its optimal operation point. Cavitation in Francis turbines was studied by Avellan [1], by Kumar and Saini [2] by Bourdon et al. [3], by Escaler et al. [4] and numerically by Guo et al. [5]. In this study, the cavitation erosion resistance of a steel type used in Francis turbine runner blades was tested and calculated and it was compared to materials previously studied in the same erosion testing setup. The comparison materials were aluminium alloy 7075, nickel aluminium bronze alloy C95400 and stainless steels A2205 and 304L.

Cavitation erosion can be divided into four periods when a virgin surface is studied; the incubation period, the acceleration period, the deceleration period and the steady-state period. In the incubation period, material deformation is dominated by plastic deformation and in the advanced periods, the deformation is dominated by crack propagation and fracture. In this study, the erosion was created in a cavitation tunnel circulating water through a radially diverging test section. The erosion evolution was measured with a contact profilometer. Acoustic emission was measured from the sample experiencing cavitation erosion and the results were combined with the erosion evolution. Material mechanical properties were obtained by elemental analysis, by macroscopic compression tests, by nanoindentation tests and by split Hopkinson pressure bar tests.

There are two ways to reduce cavitation erosion in hydraulic machinery: by designing the flow channels so that either less cavitation occurs or that it occurs where it never meets a surface and by using materials that are more resistant to cavitation. This is why knowledge about cavitation erosion resistances of materials is crucial in erosion prevention and modelling. An estimate of the stage of cavitation in an operating hydraulic machine may be used to plan future operation and maintenance. The estimate is not easy to make for a complex machine as cavitation may occur in several forms, such as travelling bubbles, sheets, clouds and cavitating vortices. In Figure 1.1, cavitation damage is seen in the Imatra power plant unit G2 Francis turbine runner blades. The runner blades in the unit G2 are made of stainless steel. The steel studied in this thesis was from Imatra power plant unit G4, which was decommissioned in 2014 and replaced with a similar stainless steel runner as in the unit G2.

Figure 1.1. *Cavitation erosion damage in the Imatra power plant G2 unit runner blades.*

Cavitation erosion testing may be done with several different types of test setups. The test setup in this study was the PREVERO cavitation tunnel in the LEGI laboratory. The same cavitation tunnel was used by Franc et al. [6; 7], by Roy et al. [8; 9] and by Deplancke et al. [10]. The cavitation tunnel creates sheet and cloud cavitation. Hattori et al. [11-14] used a vibratory cavitation apparatus to study and compare the erosion resistances of large amount of materials. Choi et al. [15] and Soyama and Futakawa [16; 17] used a cavitating jet in their studies. According to Karimi and Avellan [18], cavitation tunnels and rotational cavitation apparatus correspond better than the vibratory set-up to the forms of cavitation in Francis turbines.

Elastic waves travelling through solid material and originating from material deformation are called acoustic emission. It has been studied as a way to detect and identify cavitation by Boorsma et al. [19; 20] in marine applications, by Schmidt et al. [21] in a pump-turbine model, by Courbiere [22] in liquid sodium pumps and nozzles and by Yongyong [23] in the vibratory cavitation testing apparatus. Wolff et al. [24] tried to create a model that would use acoustic emission data to predict material loss in a Francis turbine, although they were not able to confirm the results. The erosion rate in a running hydraulic machine is complex to model as the erosion measurements cannot be made during operation.

Chapter 2 presents some theoretical insights of cavitation and cavitation erosion. It also presents the methods to measure and calculate erosion rates from the eroded sample surface. Chapter 3 presents the basics of acoustic emission and acoustic emission measurement. The experiment setup used in this study is presented in Chapter 4. It consists of material characterisation, cavitation testing and acoustic emission testing. The results for material mechanical properties, erosion evolution and acoustic emission are presented in Chapter 5. In Chapter 6, the erosion evolution and the mechanical properties of the runner blade steel is compared to those of the comparison materials and the erosion evolution of the runner blade steel is compared to acoustic emission signal evolution. The conclusions are presented in Chapter 7.

Erosion evolution and cavitation erosion resistance were divided into two categories: the incubation period length and the final erosion rate. The incubation period duration corresponds to the time required for the material to show significant surface deformation in a cavitation field. The final erosion rate corresponds to the erosion rate when cavitation erosion has been influencing the material for a long time. Both of these values for the runner blade steel were similar to those of the aluminium alloy 7075. Compared to nickel aluminium bronze C95400 and stainless steels A2205 and 304L, runner blade steel and aluminium alloy 7075 were weaker in terms of cavitation erosion resistance. Cavitation erosion resistance was observed to increase with increasing yield stress, except for the runner blade steel.

Acoustic emission signal strength decreased as the cavitation erosion developed. The frequency content of the signal showed some amplitude peaks in certain frequencies in the incubation period that did not show in the advanced erosion periods. These two observations prove that acoustic emission is a potential method for cavitation erosion evolution monitoring.

2. CAVITATION

2.1 Basic concepts

In Chapter 2.1, the basic concepts of cavitation, cavitation erosion and cavitation study are presented. Further chapters present the phenomenon in more detail and in a way that is more related to the present study.

2.1.1 Definition and occurrence

The phase change from liquid to gas is observed in everyday life through boiling. Boiling occurs when sufficient energy in the form of heat is brought to a liquid, causing the liquid temperature to reach the saturated vapour temperature and the liquid to change its phase. The thermodynamic state change in a liquid to reach boiling is normally an isobaric process and for it to reach cavitation an isothermal process. The saturated vapour pressure p_v is a function of temperature and for water at 100 ºC temperature it is 101330 Pa [25]. The phase change may also be caused by pressure dropping at constant temperature to saturated vapour pressure or a critical value near it. This phenomenon is called cavitation. Saturated vapour pressure for water at 19.85 ^{o}C is 2315 Pa [25]. [26; 27]

Cavitation in a liquid flow is caused by a sufficiently large pressure drop leading to the growth and the subsequent collapse of microscopic vapour bubbles. This is called hydrodynamic cavitation, though often referred as cavitation. The bubbles form in a low-pressure region and they collapse as they proceed to a higher pressure region. The bubbles start to form as the pressure reaches a certain critical value typically near to, but not exactly the saturated vapour pressure. Bubble formation also requires cavitation nuclei, which are typically either microbubbles of gaseous non-dissolved substances or surface formations such as cracks. Cavitation can be detected in various ways, the main ones being visual detection, sound, acoustic emission (AE) and cavitation damage. [26; 28; 29]

In hydrodynamic cavitation, both bubble growth and collapse are processes with a short timescale, the duration of both of them being several microseconds. The timescale may be larger in applications such as underwater explosions. The explosive nature of a bubble collapse causes one or several pressure impulses, which may cause material damage if the collapse occurs near a surface. [1; 29]

Low pressures in a flow field occur in regions where the flow changes its direction or velocity. For example, nozzles and valves are potential cavitation sources as they cause acceleration and deceleration in liquid flow. Rapid changes in flow direction may cause flow separation or turbulence, leading to static or transient low-pressure regions. Rotating structures, as well as any other transient structures, are potential causes for pressure fluctuations. Turbine guide vanes, runner blades or other flow directing structures may experience cavitation, especially in their leading edges. [4; 29]

In engineering applications, cavitation rarely occurs as single bubbles travelling through pressure regions. Bubbles tend to form in groups in several possible ways, depending on flow field properties, such as geometry, liquid quality and hydrodynamic conditions. Different types of cavitation are typical to certain flow fields and boundary structures. They will be discussed in Chapter 2.4.

2.1.2 Cavitation number

A cavitation number is a basic dimensionless number to characterize the tendency of a flow to cavitate. It cannot be used as a direct indicator to predict cavitation, but it is a useful quantity for studying it. The cavitation number is defined as the difference between the flow reference pressure and the liquid vapour pressure divided by the flow kinetic energy per volume: [26; 27; 29]

$$\sigma_c = \frac{P_\infty - P_v}{\frac{1}{2}\rho_l {V_\infty}^2} \tag{2.1}$$

where σ_c is the cavitation number, P_∞ is the flow reference pressure, P_v is the saturated vapour pressure, ρ_l is the liquid density and V_∞ is the flow reference velocity. The reference values P_∞ and V_∞ are values upstream from the point where cavitation begins. Pressure and velocity both have different values in the point where there is cavitation, so the reference values can be interpreted as local values with no cavitation.

Cavitation increases as the cavitation number decreases. However, the exact value where cavitation starts to occur depends on the testing facility or on the application. The cavitation number is useful in cavitation study as flows with the same cavitation number usually show some identical characteristics in terms of cavitation.

Another important dimensionless number in cavitation research is the Thoma number or the plant cavitation number σ_T, which is generally used in flow machine cavitation study. The significance of the Thoma number σ_T is the same as of the cavitation number σ_c and the difference is only in the usage. The cavitation number is a general number to determine cavitation tendency and the Thoma number is a number to determine cavitation tendency in a hydraulic machine. The Thoma number is defined as the ratio between the net positive suction head $NPSH$ and the total head H_T over the hydraulic machine:

$$\sigma_T = \frac{NPSH}{H_T} \tag{2.2}$$

Hydraulic head of a liquid flow is calculated from the liquid potential energy, the kinetic energy and the static pressure as the equivalent liquid column height. The hydraulic head of a liquid flow is calculated as: [30; 31]

$$H = \frac{P_l}{\rho_l g} + \frac{V_l^2}{2g} + Y \tag{2.3}$$

where P_l is the liquid absolute pressure, V_l is the liquid velocity, g is the free fall acceleration, ρ_l is the liquid density and Y is the height variable. All the values for hydraulic head are local values and the height variable depends on the chosen reference height. The total head H_T over a hydraulic turbine is calculated as the head difference over it:

$$H_T = \frac{P_{ti}}{\rho_l g} + \frac{V_{ti}^2}{2g} + Y_{ti} - \frac{P_{ro}}{\rho_l g} + \frac{V_{ro}^2}{2g} + Y_{ro} = H_{ti} - H_{ro} \tag{2.4}$$

where P_{ti} is the pressure, V_{ti} is the velocity and Y_{ti} is the level in the turbine inlet and P_{ro} is the pressure, V_{ro} is the velocity and Y_{ro} is the level in the runner outlet. H_{ti} is the hydraulic head in the turbine inlet and H_{ro} is the hydraulic head in the turbine runner outlet.

The definition of the net positive suction head *NPSH* is dependent on the application. It is defined as the head in the point where cavitation first occurs. In a pump, this point is in the suction side, in the runner inlet. In a hydraulic turbine, this point is the discharge side, in the runner outlet. The *NPSH* in a turbine runner outlet is calculated as: [30]

$$NPSH_{ro} = \left(\frac{P_{ro}}{\rho g} + \frac{V_{ro}^2}{2g}\right) - \frac{P_v}{\rho g} \tag{2.5}$$

In hydraulic turbine design, the values in the runner outlet may be calculated using the water levels upstream and downstream. With the use of Bernoulli's equation, the $NPSH_{ro}$ can be calculated with the downstream water setting level:

$$\frac{P_{ro}}{\rho g} + \frac{V_{ro}^2}{2g} + Y_{ro} = \frac{P_d}{\rho g} + \frac{V_d^2}{2g} + Y_d + \Delta H_{0-d} \tag{2.6}$$

where P_d is the pressure, V_d is the velocity and Y_d is the height in the downstream setting level, Y_{ro} is the runner outlet level and $\Delta H_{o\text{-}d}$ is the head loss due to friction between the runner outlet and the downstream setting level. Head loss ΔH is a term equivalent to pressure loss in a liquid flow. It is due to friction in the flow and it is dependent on the source of friction. The sources are for example pipe walls, turbulent dissipation and bends in the piping. Combining equations 2.5 and 2.6 gives:

$$NPSH_{ro} = \frac{P_d}{\rho g} + \frac{V_d^2}{2g} + (Y_d - Y_{ro}) - \frac{P_v}{\rho g} + \Delta H_{0-d} \tag{2.7}$$

The downstream setting velocity V_d is generally negligible [1].

As the Thoma number decreases, the risk of cavitation increases. Typically in machine design, cavitation curves are calculated for different running situations with a constant efficiency and a certain guide vane opening angle. The turbine efficiency remains constant until a certain value σ_{T0}, after which it starts to drop with the decreasing Thoma number. Cavitation happens also before σ_{T0}, but designing a turbine with no cavitation leads to unacceptable drops in performance. Some types of cavitation are more dependent on the Thoma number than others, which means that it is not the only tool required for advanced cavitation prediction and study. [1; 2; 4]

2.1.3 Cavitation nuclei and bubble formation

Saturated vapour pressure is a pressure in which vapour is in a thermodynamic equilibrium with its condensed form; liquid or solid. This definition proposes that in pressures below saturated vapour pressure, liquid starts to evaporate more than the gaseous form condenses. Evaporation does not always start from the point where pressure reaches saturated vapour pressure, because a pure liquid can sustain large tensions. Generally, the pressure in a liquid flow needs to be lower than the vapour pressure to for a vapour bubble to form. In some cases, the pressure limit may be higher if there is enough time for dissolved gas to diffuse through bubble walls. [27]

The liquid static pressure in a container or in a flow may drop below saturated vapour pressure, if there are no nucleation sites for vapour to form. The difference between liquid pressure and liquid vapour pressure is called tension. The values for tension are negative pressure values, pure liquids reaching relatively high negative absolute pressures. The most known application to reach such a state is the Berthelot tube, first used by Marcellin Berthelot in 1850 [32]. Tension is something that may be explained by molecular interactions and it will not be discussed in detail in this study. It is explained in detail by Brennen [27].

A Berthelot tube is a sealed tube filled with liquid in vacuum conditions. The tube does not need to be full of water. The water needs to be degassed and the container must have a clean and smooth surface. The tube is heated to a certain temperature, with the pressure increasing, and then cooled. As the liquid cools, the adhesion to walls holds the liquid when it is contracting, leading to a negative absolute pressure. This metastable state may hold in a static vessel up to several days and the negative pressure values vary from 0 MPa to values as low as -100 MPa. [33-35]

Nucleation is a process which triggers a phase change through the formation of microscopic nuclei of the new phase in the initial phase. Nucleation may be either homogenous or heterogeneous. Homogenous nucleation occurs in a pure substance in conditions where phase change is possible. In cavitation theory, this means vapour bubbles forming in pure liquid. Homogenous nucleation usually requires high tensions. Heterogeneous nucleation occurs in fluid discontinuities, in dissolved gases, in particles or in other disturbances in the pure liquid continuum. Heterogeneous nucleation is the main nucleation mechanism in most cases, as the nucleation barrier is lower than that of homogenous nucleation. The nucleation barrier is a quantity that is linked to the nucleation rate; the higher the barrier, the lower the nucleation rate. [36]

Homogeneous nucleation practically never occurs in engineering applications because of the high tension required. Heterogeneous nucleation is the main process of cavitation bubble formation, as liquids outside limited laboratory conditions contain a large distribution of impurities, as well as dissolved and non-dissolved gases. Nucleation may also occur in wall structures and any discontinuities in the fluid flow.

Nucleation sites for cavitation to occur are abundant in engineering applications and most cavitation studies, if one considers the relation between the homogenous and the heterogeneous nucleation. Nuclei distribution may still play a big role in cavitation characteristics. With low values of nuclei density, cavitation may be suppressed and with high values of nuclei density, the nuclei may affect the flow field. [27; 37]

Cavitation inception means the beginning of the occurrence of cavitation bubbles. As described earlier, the inception typically begins at pressures lower than that of the saturated vapour pressure. A basic correction to the pressure leading to cavitation inception can be reached by assuming a static equilibrium in a bubble nucleus and a spherical nucleus containing non-condensable gas with a partial pressure P_g and vapour with a partial pressure P_v. With these assumptions, a balance equation for the bubble surface can be obtained: [27-29]

$$P_L = P_v + P_g - \frac{2\gamma}{r} \tag{2.8}$$

where P_L is the local liquid pressure, γ is the surface tension parameter and r is the bubble radius.

Assuming also a negligible diffusion of gas, fast vaporisation of liquid and a slowly changing flow field leading to the isothermal compression law, it is possible to calculate critical values for pressure and bubble radius. Isothermal compression of gas can be expressed as:

$$\frac{P}{\rho} = constant \tag{2.9}$$

leading to:

$$P_g = P_{g0}\left(\frac{r_0}{r}\right)^3 \tag{2.10}$$

where P_{g0} is the initial partial pressure of gas and r_0 is the initial bubble radius. Equation 2.8 combined with equation 2.10 leads to static equilibrium curves of spherical bubbles for different initial radii and partial pressures:

$$P_l(r) = P_v + P_{g0}\left(\frac{r_0}{r}\right)^3 - \frac{2\gamma}{r} \tag{2.11}$$

where $P_l(r)$ is the liquid pressure in function of radius. Pressure curves for several initial values of r_0 and a constant P_{g0} as a function of bubble radius r are plotted in Figure 2.1.

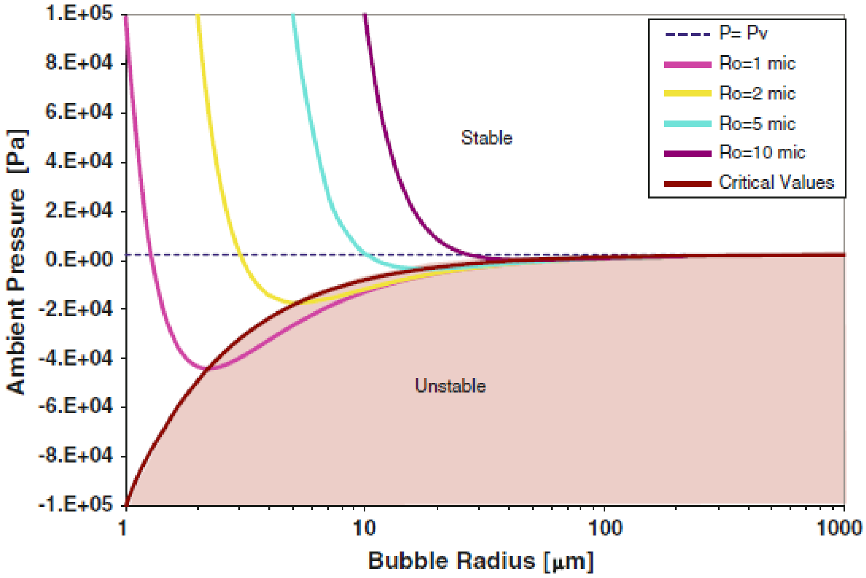

Figure 2.1. *Static equilibrium curves for several initial values of R_0 and for a constant P_{g0}. [29]*

The minimum value for equation 2.11 may be obtained by solving the zero value of the first radius derivative of equation 2.11:

$$\frac{dP_l(r_c)}{dR} = -3P_{g0}r_0^3 r_C^{-4} + 2\gamma r_c^{-2} = 0 \tag{2.12}$$

$$r_c = \sqrt{\frac{3P_{g0}r_0^3}{2\gamma}} \tag{2.13}$$

$$P_l(r_c) = P_c = P_v - \frac{4\gamma}{3r_c} \tag{2.14}$$

P_c is the critical value for liquid pressure, r_c is the critical bubble radius, r_0 is the initial bubble radius and P_{g0} is the initial partial pressure of the non-condensable gas. If the minimum pressure in a liquid flow is larger than the critical pressure P_c, a bubble grows in the minimum pressure region, but it stays stable and recovers its initial size in the pressure recovery region. If the minimum pressure is lower than the critical pressure, the bubble becomes unstable and grows explosively, collapsing in the pressure recovery region. [26; 29]

This approach does not accurately represent the reality in bubble growth, as the assumptions are not valid in real cavitating flows. It gives a basic idea of how the critical pressure differs from the liquid vapour pressure. In real flows, bubbles do not remain spherical and the compression may not be close to isothermal. In real flows, cavitation often occurs in regions where the flow field changes rapidly, so the assumption of a slowly changing flow field may also not be valid. [27; 29]

2.1.4 Bubble collapse

As a cavitation bubble in a liquid flow grows, the pressure inside the bubble decreases, reaching a value close to the liquid vapour pressure, which is generally much smaller than the average flow pressure. When the bubble moves forward in the flow and when the local static pressure increases, the surface tension of the bubble makes it possible for a pressure difference to form between the bubble interior and the surrounding liquid. The timescale of the bubble collapse is of the magnitude which enables large pressure differences to form, so the bubble collapse can lead to high amplitude pressure waves. [26]

Cavitation may also occur in static liquids, if the liquid is subjected to an oscillating pressure field or if the liquid experiences a sufficiently high strain. Cavitation caused by an oscillating pressure field is called acoustic cavitation. This is widely used in cavitation testing, as it provides a simple and compact way to create cavitating conditions. The most common acoustic cavitation device is the standardized ASTM G32 cavitation erosion vibratory apparatus. The ASTM G32 apparatus is discussed in Chapter 4.6.1. [26; 38; 39]

The bubble collapse process is dependent on the bubble environment. If a perfectly spherical bubble collapses in free liquid, the collapse happens axisymmetrically. All deviations from the spherical form or any disturbances in the surrounding liquid lead to a non-symmetrical collapse of the bubble. A non-symmetric bubble collapse in cavitation has normally two important stages: the re-entrant jet formation and the bubble ring collapse phase. Typical causes for a non-symmetrical collapse are nearby wall structures, adjacent bubbles or other particles and substance interfaces. [26; 27]

The re-entrant jet is formed from the surrounding liquid when a cavitation bubble collapses non-symmetrically. The bubble begins to collapse from a certain point and from this point; the collapse develops with the highest speed. This means that the bubble-liquid interface gains a larger acceleration towards the bubble centre in one side of the bubble than that of the other sides. The liquid jet towards the bubble centre penetrates the bubble and the bubble-water interface on the other side.

If the bubble collapses near a boundary, the re-entrant jet is directed towards it, with the exception when the boundary or wall is sufficiently elastic. The elasticity has to be high compared to most metals for the reverse behaviour. As the re-entrant jet penetrates the bubble, it continues towards the boundary. The liquid between the wall and the closest interface moves away from the re-entrant jet. The jet speed typically is typically of the magnitude of 100 m/s and it may cause material damage. [26; 27; 40; 41]

The reason why the bubble collapses towards the boundary is complex. The non-symmetricity of the surrounding environment of the bubble causes differences in the bubble-water interface, which lead to non-symmetric forces directed towards the bubble centre. As the form of the bubble develops, the non-symmetric effects increase, which lead to accelerating bubble deformation. The first observations to this behaviour were from experiments and the analytical calculation of such behaviour is not possible. Plesset and Chapman [42] were the first to study the collapse of a spherical bubble near a wall with numerical methods. The re-entrant jet formation mechanism is beyond the scope of this study and the jet direction towards the wall will be treated as a given fact.

The next stage in the bubble collapse is the formation and the collapse of a stagnation ring. As the re-entrant jet penetrates the bubble, a ring shaped cavity remains. The cavity ring has high vorticity resulting from the initial re-entrant jet. The ring cavity collapses inside and causes a high amplitude pressure wave. Chahine and Genoux [43] proved that the collapse of a ring shaped bubble causes a higher pressure peak than that of an equivalent spherical bubble. The bubble ring collapse pressure peak to a boundary material close to the collapse may be larger or smaller than that of the re-entrant jet. The magnitudes of both the impulses are case dependent. The pressure impulses will be discussed in more detail in Chapter 2.2. [29]

2.1.5 Cavitation erosion

Cavitation erosion can be divided into four different periods: the incubation or pitting period, the acceleration period, the deceleration period and the steady-state period. Cavitation erosion in a virgin surface begins by the formation of pits caused by plastic deformation. As the surface is covered with pits, material starts to fail as some impacts exceed the rupture stress of the material, causing acceleration in overall mass loss. As the eroded surface forms, deeper pits start to affect bubble dynamics, decelerating overall mass loss. Mass loss rate generally reaches a constant or a pseudo-constant value if the erosion lasts long enough without the structure failing. The erosion periods are discussed in more detail in Chapter 2.5. [15; 26; 44]

A bubble collapsing near a surface may cause material damage if the pressure caused by the collapse exceeds a certain material threshold. For elastic materials, such as metals, plastic deformation occurs if the yield stress is exceeded. Work hardening of a material surface in a period of time eventually causes material failure through rupture. For high yield stress materials, fatigue and crack formation are the main rupture mechanisms and for low yield stress materials, rupture stress may be immediately exceeded by the impacts. The aggressiveness of the erosion depends on material characteristics and on the cavitation field, the relations being complex. [45; 46]

An important quantity in cavitation impacts is the strain rate $\dot{\varepsilon}$. Strain ε is the relative deformation of a structure, either in compression or in tension. Strain is defined as:

$$\varepsilon = \frac{\Delta S_{st,0}}{S_{st,0}} = \frac{S_{st} - S_{st,0}}{S_{st,0}} \tag{2.15}$$

where $S_{st,0}$ is the initial structure length, ΔS_{st} is the change in structure length and S_{st} is the structure length in a given moment. The values for strain in compression are negative and for tension they are positive. Strain rate is defined as the velocity of change in strain:

$$\dot{\varepsilon} = \frac{d\varepsilon}{dt} = \frac{d}{dt}\frac{(S_{st} - S_{st,0})}{S_{st,0}} = \frac{1}{S_{st,0}}\frac{dS_{st}}{dt} = \frac{V_{def}}{S_{st,0}} \tag{2.16}$$

where $\frac{d}{dt}$ is the time derivative operator and V_{def} is the deformation velocity.

The deformation mechanics of a material may be dependent on the strain rate. An important quantity to measure this dependency is the flow stress. Flow stress is defined as the required load maintaining a certain strain rate in a deforming material. For low strain rates, the strain rate has only a small influence on the flow stress and above a certain material dependent limit; the strain rate dependency on the flow stress starts to increase rapidly. The limit for metal alloys is of the order of:

$$\dot{\varepsilon} = 10^3 s^{-1} \tag{2.17}$$

In regard of plasticity mechanisms, strain rates below this limit present dislocation dynamics and thermally activated processes and strain rates above this limit present velocity dependent viscous drag mechanisms. For higher strain rates, the required flow stress increases rapidly, as for the lower strain rates the flow stress required is almost constant. [29; 47]

The strain rate dependency on flow stress varies with different materials. Metal alloys, which are materials widely used in hydraulic machinery, often have high strain rate sensitivity. Cavitation impulses have a relatively short duration and relatively high amplitude in pressure, leading to material strain rates in the transition region of strain rate dependency. This means that some of the cavitation impulses in a cavitation field fall into the category of low strain rate sensitivity and some into the category of high strain rate sensitivity. Because of this behaviour, the strain rate dependency has to be taken into account in cavitation erosion deformation models. [29; 47]

The collapse process of a cavitation bubble near a wall may also be affected by the deforming surface. As the surface is deforming, the flow field in the collapse process changes. A virgin surface with no initial plastic deformation experiences higher changes in strain than a work hardened surface that has already experienced cavitation impacts. The higher amount of deformation typically leads to the damping of the impulse strength so the effective stress to the material surface is smaller. The amount of damping is dependent on the amount of surface deformation, but the effective stress is always smaller than that of a rigid wall.

This two-way interaction has to be taken into account for accurate study of the deformation process in a cavitation impulse. Kalumuck et al. [48] and Chahine and Kalumuck [49] studied this process experimentally and numerically, finding out that the reduction of the effective stress for a deforming wall is significant and should be taken into account. The fluid-wall interaction will be discussed in more detail in Chapter 2.2 [50]

2.2 Cavitation impulses and loadings

In Chapter 2.2, bubble dynamics, pressure peaks, loadings caused by bubble collapse and the methods for predicting these phenomena are discussed in detail. A cavitation bubble collapsing near a surface generally forms at least two distinctive pressure peaks, the first caused by a re-entrant jet and the second by a bubble ring collapse. Either of them may be stronger than the other, depending on the collapse environment. The fluid-structure interaction is also discussed in detail. In Chapter 2.2.1, two methods of studying bubble growth and collapse dynamics are described. In Chapters 2.2.2 and 2.2.3 the information obtained by the two methods is discussed.

2.2.1 Numerical methods: a brief description

Cavitation bubbles generally reach a radius in the magnitude of 100 times the initial nuclei radius [27]. Peak pressures may reach the magnitude of several hundred MPa [51]. Analytical models fail to describe bubble collapses accurately. Numerical modelling of the phenomenon has been widely developed and the modelling provides more information about the complex dynamics.

Two different models for bubble collapse and growth dynamics prediction are briefly presented in this section. These models are not used in this study, but results obtained by them provide information about the bubble collapse process. Bubble dynamics can generally be approximated as incompressible processes, excluding shock wave formation and liquid-liquid or liquid-solid impacts. This leads to a situation where most of the process duration may be approximated as incompressible, leaving some important parts to be treated as compressible [50]. It is also important to couple the collapse dynamics with the material response from the surface, as already described in Chapter 2.1.5.

The first model to be discussed is an incompressible and compressible link procedure to model bubble collapse dynamics. It was reported and used in studies by Hsiao and Chahine [52] and Hsiao et al. [53]. This model assumes that the bubble growth may be modelled as incompressible and that the bubble collapse has to be modelled as compressible from a certain point. Modelling that assumes the gas content in the bubble compressible requires more computing time than that assuming it incompressible.

This type of modelling requires a link procedure to determine from which point the process of a bubble growth-collapse is treated as incompressible and from which point compressible. This type of modelling can also be coupled with a structural code to take into account the effects of the deforming surface. Hsiao et al. [53] used an analytical elastic-plastic model in their report and Hsiao and Chahine [52] used a finite element method (FEM) model in their report. [50]

The aforementioned authors found out that the pressure peaks generated by the re-entrant jet and the bubble ring collapse are higher than the equivalent stress that the deforming material experiences. Choi and Chahine [54] proved that the ratio between these two stresses may be as low as 0.1. Some results calculated by the aforementioned methods and their significance is discussed in Chapter 2.3.1

The second model is called the Modified Ghost Fluid Method (MGFM) and it was proposed and developed by Liu et al. and Xie et al. in references [55-57]. The model is modified from the Ghost Fluid Method (GFM), developed and proposed by Fedkiw et al. [58; 59].

The GFM model uses virtual fluid cells called ghost cells inside a phase interface, to remove the discontinuity in velocity and pressure profiles caused by an interface. Discontinuities may cause numerical oscillations in Euler type solvers. The ghost cells co-exist with the real fluid cells and cause the solver to treat the interface as a continuous fluid, removing the numerical oscillations. GFM model was originally used to treat deforming gas with a moving interface. [58; 59]

The MGFM model has several improvements to the GFM model, making it more suitable for solving fast moving interfaces, such as interfaces in underwater explosions, flame fronts or collapsing cavitation bubbles. Liu et al. [55] added an approximate Riemann solver to predict isobaric values and ghost fluid status. Liu et al. [56] and Xie et al. [57] extended the MGFM model to be able to handle compressible fluid-compressible structure interfaces.

2.2.2 Re-entrant jet dynamics

Bubble collapse dynamics near a rigid surface provide basic information about the re-entrant jet formation and the following bubble ring collapse. In this section, the bubble collapse near a rigid wall is discussed and the effects of a deforming wall are introduced to the re-entrant jet formation process.

The formation of a re-entrant jet begins when the pressure in a flow field is sufficiently high after the cavitation inception. The liquid particles forming the re-entrant initially move to the direction with the lowest resistance, thus increasing the pressure in that particular region. The jet formation begins in the region with the highest pressure. If the bubble collapses near a free surface, the jet direction is away from the free surface and if the collapse happens near a solid boundary, the jet direction is towards the boundary. As already mentioned in Chapter 2.1.4, the physical explanation for the jet orientation is beyond the scope of this study. [26]

As the re-entrant jet begins to form near a solid wall, the moving bubble interface causes the compression of gases inside the bubble and thus accelerates the liquid between the bubble and the boundary. This description is valid only for a non-moving bubble near a boundary. For a moving bubble near a boundary, the collapse mechanics are more complex and they are not addressed in this study. In Figure 2.2, the re-entrant jet formation and the jet impact near a rigid boundary are presented. The process was numerically modelled by Zhang et al. [40]. [26; 41; 60]

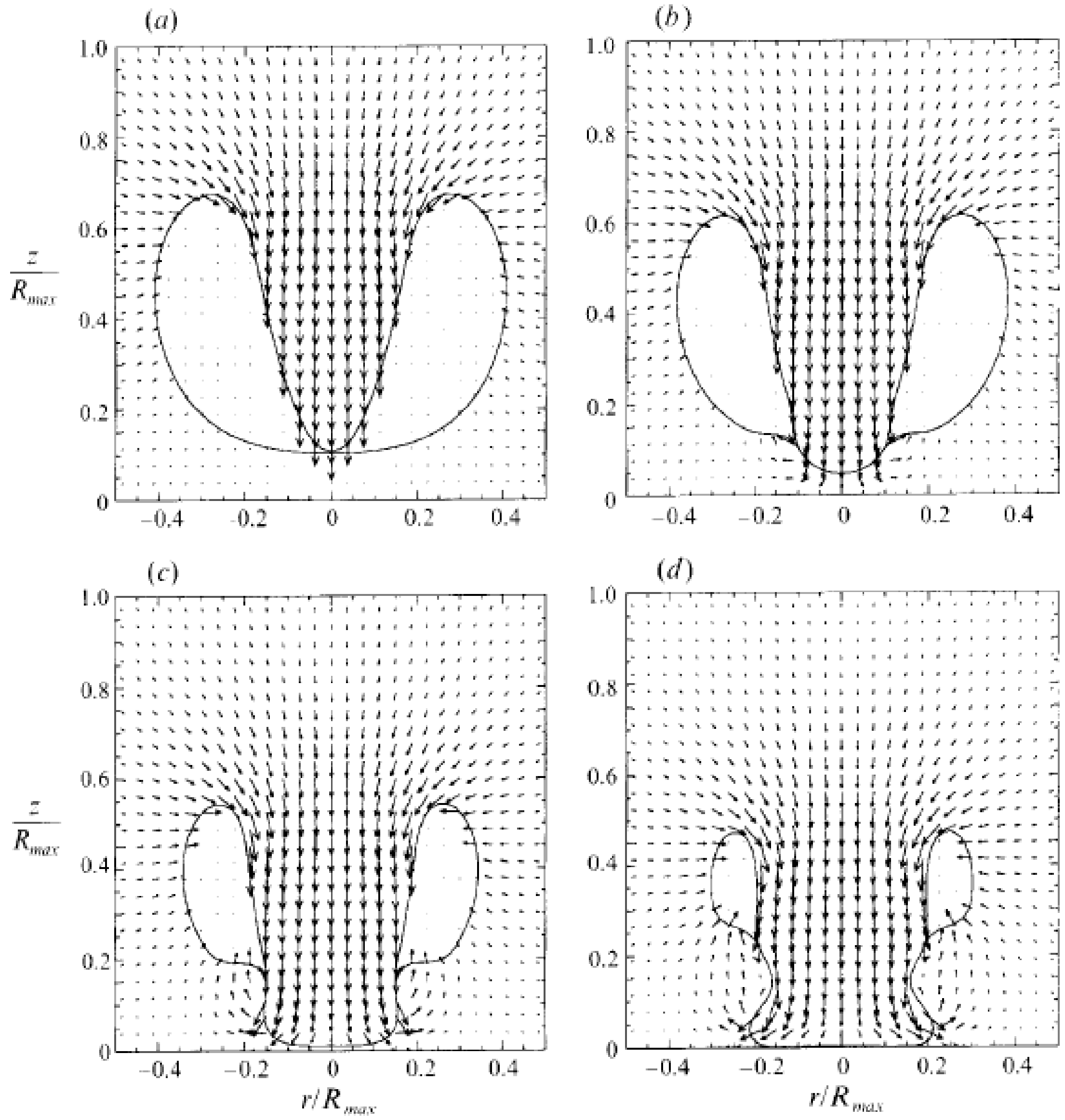

Figure 2.2. *Static bubble re-entrant jet development and impact for non-dimensional time-steps: a: t'*=2.1509 b: t'*=2.16400 c: t'*=2.18074 d: t'*=2.19429. The arrows in the figures represent the liquid flow relative velocity. The velocity increases with increasing arrow length. [40]*

In Figure 2.2, the non-dimensional time t'^* is defined as:

$$t'^* = \frac{t}{r_{max}} \left(\frac{\Delta P}{\rho_l} \right)^{0.5} \tag{2.18}$$

where t is time, r_{max} is the maximum bubble radius for a bubble growing in an infinite fluid and ΔP is the pressure difference between the pressure far from the bubble and the bubble internal pressure, which is assumed to be constant. [40]

The re-entrant jet visualized in Figure 2.2 presents the basic concepts in a bubble collapse even though the modelling was done using many non-valid assumptions regarding a real cavitation situation. As the re-entrant jet forms, the bubble is reduced to a ring bubble. The impact towards the wall generates a circulating flow away from the impact sector and the wall. This leads to a bubble ring with vorticity. [40; 41; 60]

The distance between the bubble centre and the boundary has a significant effect on the re-entrant jet formation and the impact strength. This distance is generally called the stand-off distance and it is made non-dimensional by dividing the distance Z with the maximum bubble radius r_{max}. If the stand-off distance is too small, the re-entrant jet has too little time to develop and accelerate to create a significant impulse and if the stand-off distance is too big, the liquid layer between the bubble and the wall absorbs most of the kinetic energy in the jet. Normalized stand-off distances between 0.5 and 2.0 generally show the most significant phenomena related to bubble collapses and the largest impacts generally occur with values between 0.75 and 1.25. [40; 41; 50; 60]

The deformation or movement of a surface generally reduces the effective pressures generated by a bubble collapse. Chahine and Kalumuck [49] found that a flexible plate experienced as much as 40% lower amplitude shocks than a rigid plate at the highest jet pressure in their water slug experiments. Figure 2.3 shows the evolution of a bubble collapsing near a wall with four different wall elasticities, modelled by a spring-backed membrane model. [61]

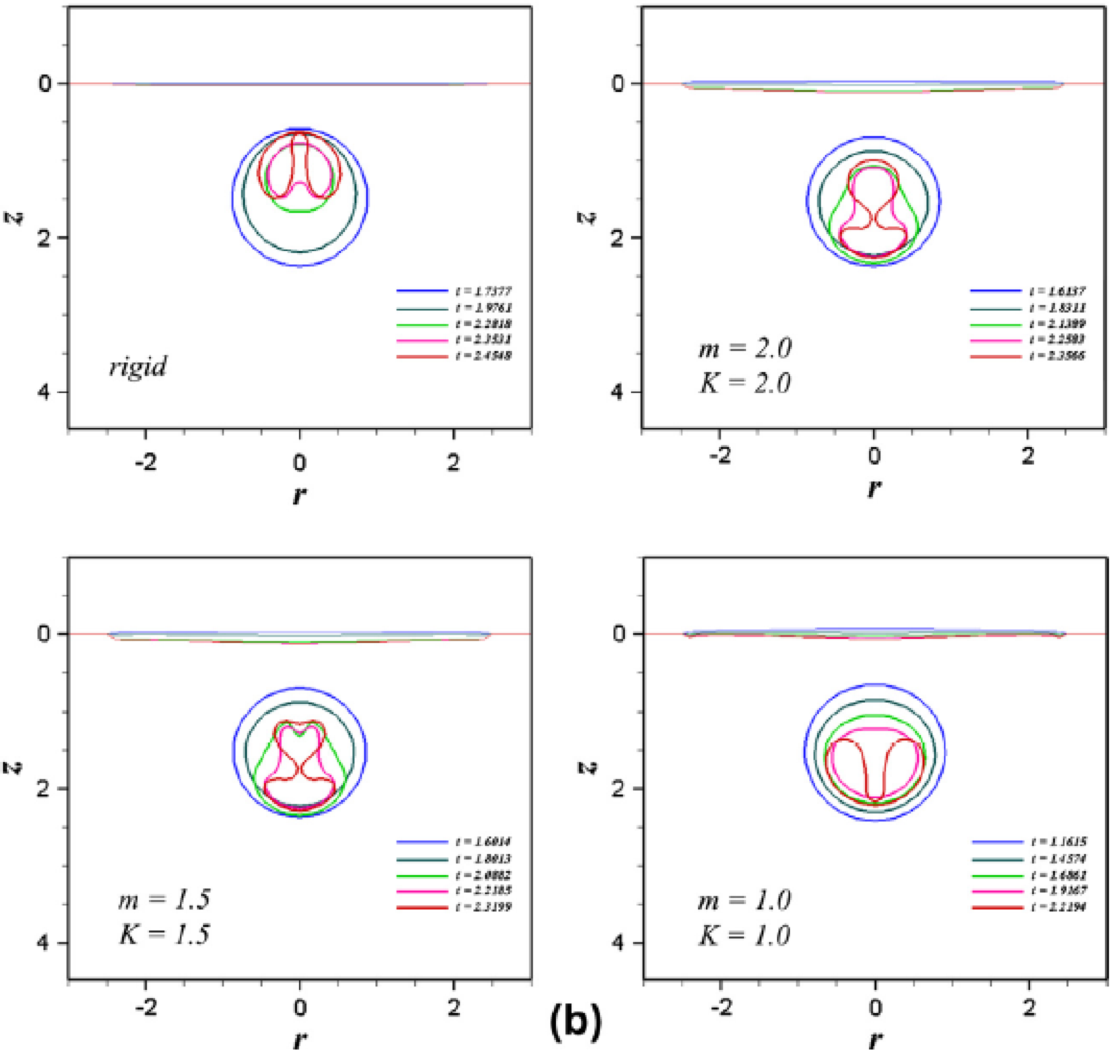

Figure 2.3. *Static bubble collapse near a wall with four different values of wall elasticity modelled by a spring-backed membrane model. The wall is located in the z = 0 level indicated in the figures. [61]*

Figure 2.3 was presented in the report by Madadi-Kandjani and Xionq [61]. The bubble growth did not show any difference in behaviour between different elasticities. The elasticity parameters *m* and *K* present the mass per unit area and spring stiffness per unit area, respectively. Lower values for both parameters represent higher elasticity. For high elasticity, the re-entrant jet may be directed away from the surface and for medium elasticity; the bubble may obtain an hourglass shape. This was also observed by Klaseboer et al. [62] in their study of bubble collapses near an elastic liquid boundary.

2.2.3 Bubble stand-off distance effects

The stand-off distance is the distance between the bubble centre and the boundary near the collapsing bubble. The stand-off distance is typically normalized by dividing the actual distance with the bubble maximum radius. The bubble collapse process is dependent on the stand-off distance. For small distances, the re-entrant jet and the resulting bubble ring do not have time to fully develop so the impact strength is reduced. For large distances, the liquid between the bubble and the wall has a damping effect on the impacts.

The maximum impact pressures resulting from a bubble collapse typically happen with a stand-off distance around 1. This section discusses the effects of stand-off distance to the collapse process for several regions. The stand-off distance has an effect on the re-entrant jet formation and behaviour and also to the resulting bubble vortex ring. The stand-off distance Z_s is defined as:

$$Z_s = \frac{r_{max}}{Z} \tag{2.19}$$

where r_{max} is the bubble maximum radius and Z is the distance from the bubble centre to the boundary.

After the initial re-entrant jet formation and impact towards a surface, only a ring formed bubble remains of a cavitation bubble. The bubble ring contains gas with low pressure and the ring has obtained vorticity from the outward flow caused by the re-entrant jet. The ring collapses because of the pressure difference between the surrounding liquid and the ring, the collapse being stronger than that of an equivalent spherical bubble. The vorticity may cause the collapse to have a delay or to be damped. [43]

Yang et al. [63; 64] conducted particle image velocimetry (PIV) experiments for single bubble collapses with varying stand-off distances. The bubbles were created in a U-shaped rotating platform with a liquid filled tube. The rotation leads to a parabolic pressure distribution, the lowest pressure being in the middle, making it possible to reach saturated vapour pressure and to generate a cavitation bubble. The bubble ring collapse process is classified with the stand-off distance in a similar way as in the aforementioned papers. This classification provides a good distinction between different behaviours.

For a stand-off distance $Z_s \approx 7$, the interaction between the bubble and the wall is negligible. A re-entrant jet is formed due to the instabilities in the flow field and bubble interface or due to the pressure difference in the flow field, as in [63; 64], where the re-entrant jet is formed in the axial direction, not towards the boundary. This type of a collapse causes a Kelvin-Helmholtz type vortex to form. Kelvin-Helmholtz instabilities are caused by a velocity difference between two fluids with a common interface. When the velocity difference is large enough, the flow is called a shear flow, where the interface is unstable, leading to wakes and other turbulent instabilities. The bubble ring caused by the re-entrant jet penetration is eventually torn apart to two or multiple bubbles by the Kelvin-Helmholtz instabilities. [63-65]

For a stand-off distance $Z_s \approx 3$, a Kelvin-Helmholtz type vortex is generated after the re-entrant jet impact towards the boundary. This value is the critical value for a counter-jet to form after the re-entrant jet impact, depending on the pressure pulse causing the bubble collapse. If the pulse is large enough, the vortex touches the boundary, which leads to shock wave formation. The shock wave causes a Richtmeyer-Meshkov type instability, which refers to the formation of non-linear structures, such as bubbles and spikes in an interface between two fluids. The Kelvin-Helmholtz vortex touching the solid boundary causes radial outward splashing and a counter jet to form in the normal direction of the wall. Formation of a stagnation ring is linked to the counter jet phenomenon. If the pressure pulse is not large enough to cause the vortex to touch the boundary, the bubble ring collapse is similar to collapses with a higher stand-off distance. [63; 64; 66]

For a stand-off distance $Z_s \approx 2$ the Kelvin-Helmholtz vortex causes a stagnation ring to form. The stagnation ring is a structure of non-flowing fluid near the solid boundary and it divides the flow into two. The stagnation ring moves towards the solid boundary, compressing the liquid between the bubble and the solid boundary and causing the flows. The outward flow is called splashing and the inward flow a counter jet. The inward flow turns outwards from the solid boundary, counter to the original re-entrant jet. [63; 64]

For stand-off distances $Z_s \approx 1$ and $Z_s = 1$, the space between the bubble and the solid boundary decreases to such a small value that it does not allow a complete Kelvin-Helmholtz vortex to appear. For stand-off distances slightly over 1, the stagnation ring, the counter jet and the splashing are observed, although the bubble ring tends to flatten significantly. For a stand-off distance of exactly 1, a stagnation ring is not formed, and the fluid flow from the re-entrant jet flows outwards radially. For stand-off distance values near 1, the bubble is always flattened and concave shaped. [63; 64]

As the remaining bubble ring collapses, a second pressure wave is formed. The pressures caused by the re-entrant jet and the bubble ring collapse were calculated by Chahine [50] using the incompressible and compressible link method mentioned in sub-Chapter 2.2.1. Figure 2.4 shows the modelled pressure values for different bubble collapse driving pressures. The bubble collapse driving pressure is the artificial pressure around the initial bubble created for the numerical study to cause the bubble to collapse. The first pressure peak is caused by the re-entrant jet impact and the second is caused by the bubble ring collapse pressure wave.

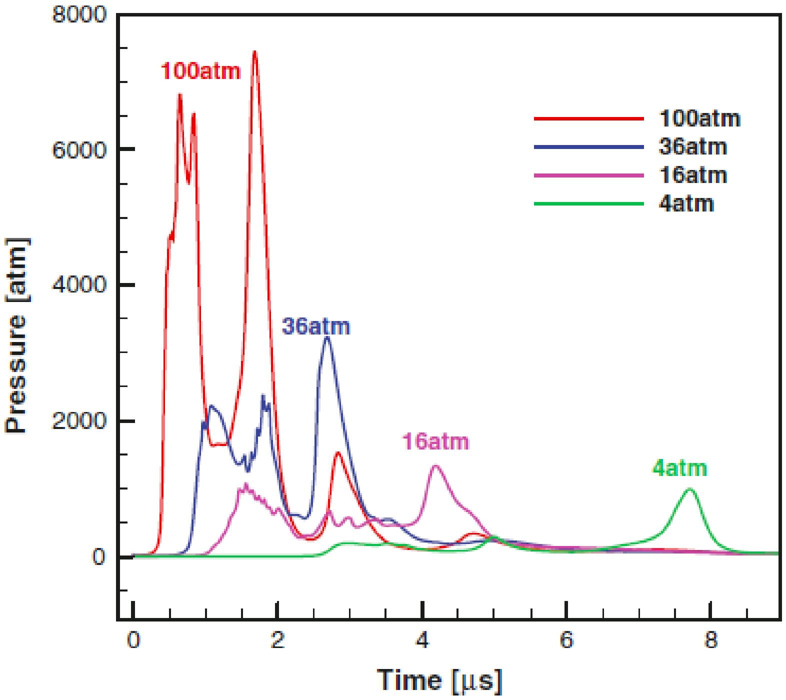

Figure 2.4. *Impact pressure for varying bubble collapse driving pressure, modelled by the incompressible and compressible link model. [50]*

As shown in Figure 2.4, the re-entrant jet and the bubble ring collapse lead to separate pressure peaks. The timescale of the bubble collapse can be easily detected. The time difference between the two pressure peaks is from several hundred nanoseconds to around two microseconds. The pressure peak caused by the bubble ring collapse is higher than that of the re-entrant je. This is not always the case, as the re-entrant jet strength is highly dependent on the flow characteristics and the stand-off distance.

The peak impact pressure is dependent on the physical conditions. The pressure in the surrounding liquid has a large impact on the collapse pressures. Brennen [27] proposed a formula to estimate the peak pressure in a bubble collapse:

$$P_{peak} = \frac{100 r_{max} P_\infty}{Z} \tag{2.20}$$

where P_∞ is the surrounding liquid pressure. This formula does not predict the peak pressure accurately, but it predicts the order of magnitude of the peak pressure.

2.3 Material response

When cavitation bubbles collapse near a surface, the material experiences high amplitude and low duration stresses. Material properties such as ductility, yield stress, strain rate sensitivity and ultimate stress are the key factors in defining the erosion potential of a certain cavitation field. The initial effect of cavitation for a ductile material is plastic deformation, observed as pits in the surface. After the surface is covered with pits, advanced stages of cavitation including material removal take place. In Chapter 2.3, the material effects and an erosion model for cavitation impulses are discussed.

2.3.1 Pit formation

As described in Chapters 2.1.5 and 2.2.1, the pitting of a virgin surface is a complex process. The coupling of material deformation and bubble collapse dynamics is required for correct behaviour prediction. The basic limit of stress for plastic deformation to occur is the material yield stress. Cavitation bubble collapses inducing pressure peaks below this limit cause no damage to the material, excluding possible fatigue effects. According to Knapp et al. [67], cited by Pereira et al. [68], an experimental value for the number of damaging cavitation impacts was found to be one damaging impact for every 30,000 impacts. Hammitt [69] states that only one cavitation impact in 10^4 to 10^6 causes any material damage in a typical cavitating flow.

A pit formed by an individual bubble collapse generally does not have a round shape, but the round shape is often assumed for simplicity in erosion models. As the material undergoes plastic deformation, it either piles up or sinks in around the pit. The ratio between the Young's modulus E and the yield stress σ_y may be used to predict which behaviour to be expected. With high values of E/σ_y, piling up is expected and for low values of E/σ_y sinking in is expected. Metals and other ductile materials have high values of E/σ_y and the cavitation pits are formed as spherical caps. [70]

As discussed in the previous chapters, the collapse of a cavitation bubble is a process with multiple steps. The two main pressure peaks are caused by the re-entrant jet impact and the bubble ring collapse pressure wave. When the material deformation is significant, several other pressure peaks can be detected in numerical simulations and possibly in experiments. Figure 2.5 presents the normal stress component of the first plate element below the material surface in a cavitation bubble collapse impact simulated with a FEM model by Chahine [50].

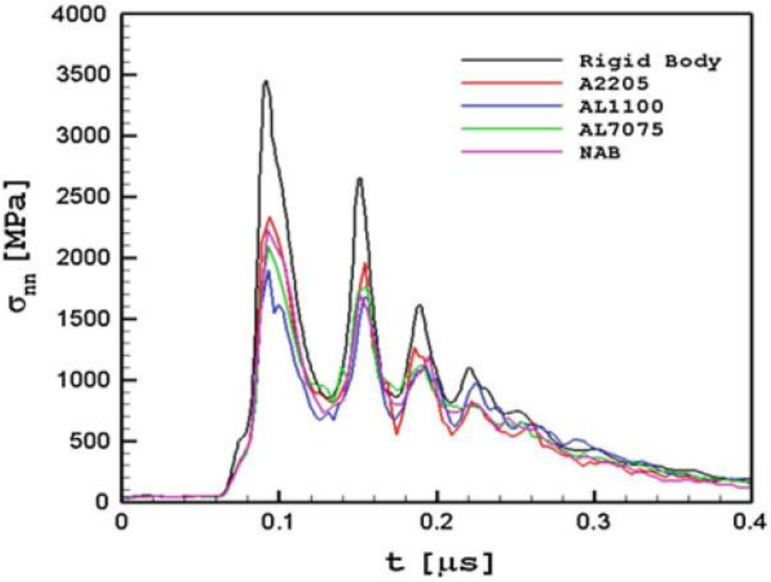

Figure 2.5. *Normal stress component of the first plate element below material surface in a cavitation impact simulated with a FEM-model. Bubble initial radius 400μm, stand-off distance 400μm and collapse driving pressure rise from 0.1 MPa to 10 MPa. [50]*

In Figure 2.5, the first pressure peak is the re-entrant jet impact and the second is the bubble ring collapse pressure wave. After these two peaks, diminishing oscillations can be observed. These oscillations are caused by propagating stress and strain waves. The strain has an elastic part and a plastic part and as the elastic part is reversible; the plastic part remains after the stress has ended. The normal stress component is presented in the figure, though for non-rigid boundaries the radial stresses are often significant, so the equivalent stress is also a parameter of interest. [50]

A cumulative strain model was first proposed by Karimi and Leo [71], and similar models were developed and used by Berchiche et al. [72], by Franc [6; 7] and by Karimi and Franc [46]. The basic idea of such models is to calculate the cavitation erosion progress with the concepts of cumulative strain and work hardening. The energy from cavitation impulses is absorbed to the material and the accumulation of subsequent impacts and strains cause the material to harden. As cumulative strain reaches rupture strain, material is removed and a new surface is subjected to cavitation erosion.

Cavitation impacts have a certain distribution in amplitude and duration. The pits created by these impacts have a certain distribution in depth, diameter and shape. This leads to the requirement of a statistical approach for a cavitation model that addresses cavitation erosion characteristics, such as erosion rates and incubation times. If the flow field remains constant in terms of cavitation, the cavitation field may be characterized by pitting tests. With the cavitation field and material properties, a statistical analysis may be performed to create erosion models for ductile materials.

2.3.2 Erosion modelling

A statistical cumulative strain cavitation erosion model can be created for a material by using cavitation impact test data, as was described in Chapter 2.3.1. This requires several assumptions and characteristic values, which are described in this chapter.

The stress-strain relationship in the region between the yield stress σ_y and the ultimate stress σ_U may be expressed with the Ludwik equation: [6; 72; 73]

$$\sigma = \sigma_y + K'\varepsilon_p^n \tag{2.21}$$

where *K'* (MPa) is the strain hardening constant and *n* (-) is the strain hardening exponent, which both are acquired experimentally. This equation is valid for low strain rates. For cavitation impacts, the strain rates are high. If the strain rate dependency is tested, the Johnson-Cook equation may be used to describe stress-strain relationship with variable strain rate: [9]

$$\sigma = (\sigma_{y,ref} + K'{\varepsilon_p}^n)(1 + Cln\frac{\dot{\varepsilon}}{\dot{\varepsilon}_0}) \tag{2.22}$$

where *C* is the constant obtained from the linear fit of the experimental data in with yield stress σ_y in function of the natural logarithm of strain rate $\dot{\varepsilon}$. The reference strain rate $\dot{\varepsilon}_0$ may be freely chosen and a typical value is 1 1/s. ε_p is the plastic strain, meaning that in the yield point it is zero. $\sigma_{y,ref}$ is the yield stress for the reference strain rate. The yield stress may be written as:

$$\sigma_y = \sigma_{y,ref}(1 + Cln\frac{\dot{\varepsilon}}{\dot{\varepsilon}_0}) \tag{2.23}$$

and

$$\frac{\sigma_y}{\sigma_{y,ref}} = 1 + Cln\frac{\dot{\varepsilon}}{\dot{\varepsilon}_0} \tag{2.24}$$

The reference yield stress $\sigma_{y,ref}$ is found by plotting the yield stresses available in function of the natural logarithm of the relative strain rates. The reference strain rate is found by a linear fit to this data and by finding the yield stress value for the reference strain. By plotting the relative yield stresses and the natural logarithms of the relative strain rates, a linear relation is also found. The slope of the linear fit is the parameter *C*.

A strain profile inside a material may be expressed as: [6]

$$\varepsilon(x) = \varepsilon_s\left[1 - \frac{x}{l_h}\right]^\theta \tag{2.25}$$

where ε_s is the surface strain, x is the depth variable, l_H is the hardened layer thickness and θ is the strain profile shape factor. For a surface that has been work hardened up to the ultimate stress σ_U, the hardened layer thickness is L_H. The values for L_H and θ may be found in material characteristics tables or they may be obtained experimentally.

An experimental quantity called the mean depth of penetration rate *MDPR* is the average erosion penetration rate over the eroding surface. It presents the speed of cavitation in a certain flow field for a certain material. According to Soyama and Futakawa [16], Hammitt [69] and to Zhou and Hammitt [74], the incubation time T is related to the mean depth penetration rate *MDPR* with the following relation:

$$\frac{1}{MDPR} = k'T_i^{\alpha} \tag{2.26}$$

where k' is an experimentally obtained constant value for a certain material and a certain type of test and α is an exponent obtained from cavitation and liquid impact data with a value between 0.6 and 1.0. T_i is the incubation period duration.

The approximate steady state erosion rate for cavitation erosion may be obtained with an energy approach and by assuming successive coverings by cavitation impacts. The method to obtain equation 2.27 is presented by Franc [26] and by Karimi and Franc [46]. The steady-state erosion rate may be presented as follows: [46]

$$\dot{E} = \frac{L}{\tau}\left\{\left(\frac{\sigma_m - \sigma_Y}{\sigma_U - \sigma_Y}\right)^{\frac{1}{n\theta}} - 1\right\} \tag{2.27}$$

where $\dot{E}$ (m/s) is the erosion rate assuming uniform erosion in depth and σ_m is the mean amplitude of impact stresses. This approach provides means to predict erosion rates with material characteristics and only two flow characteristics, the coverage time τ and the mean amplitude of impact stresses σ_m. The mean amplitude of impact stresses is the average pressure amplitude for the cavitation impacts and it is difficult to measure or calculate. Pressure sensors or methods such as the inverse finite element method combined with pitting tests may be used to predict the value of σ_m [8].

The coverage time is defined as the time for the cavitation pits to cover the material surface exactly once, with no pit overlapping. It can be assumed to be relatively material independent, so equation 2.27 provides a prediction of erosion rate with variables that are simply defined as either material dependent or flow dependent.

2.4 Cavitating flow characterization

Cavitation rarely occurs as single bubbles travelling from a low-pressure to a high-pressure region. Usually bubbles form in small or large groups, both in engineering applications and in laboratory test conditions. The type and form of cavitation depends on flow geometry, pressure levels and liquid quality. There are large differences between the erosion and aggressiveness potential of different types of cavitation. In this chapter, the main forms of cavitation are classified in the same way as in the book: *Fundamentals of Cavitation* [26].

2.4.1 Transient isolated bubbles

Transient isolated bubbles represent individual bubbles forming in a flow through cavitation inception mechanisms described in the earlier chapters. The bubbles are scarce enough not to interact significantly with each other. This type of cavitation includes both spherical or non-spherical and symmetric or non-symmetric bubbles. The bubbles appear in a flow in low-pressure regions and the cavitation structures are of unsteady nature.

When cavitation bubbles appear in a liquid flow, they usually do not affect the liquid flow dynamics significantly. Cavitating flows are often treated as single phase flows in terms of flow dynamics. This one-way coupling is not always sufficient, because when the flow void fraction increases sufficiently, the bubbles begin to modify the flow significantly. The bubbles may affect for example the lift or drag experienced by a hydrofoil or other flow structures as the flow density and other values are modified. The need of two-way coupling is highly case dependent and it will not be discussed further in this study. [75]

Transient isolated bubbles or travelling bubble cavitation is a form of cavitation that generally does negligible or little damage to surfaces. It may cause noise or acoustic signals in an engineering application, and even some damage, if the bubbles are numerous enough and they collapse near a solid boundary. [4]

2.4.2 Attached or sheet cavities

Attached or sheet cavities, also called as partial cavities, appear in the low-pressure region of structures in a liquid flow. Typical structures are the leading edges of blades, hydrofoils or guide vanes and also the throats of nozzles. Attached cavities persist in a steady flow and the cavitation inception remains in a fixed region. Cavitation closure remains also in a fixed region, with some possible periodical variation. Cavitation closure is defined as the collapse of the cavitation structure. A sheet cavity follows the flow pattern around the structure and it collapses near the surface, potentially causing damage.

The periodic pattern of a sheet cavity is called a cloud cavity, which is an aggressive type of cavitation that occurs in certain types of sheet cavitation. The sheet cavity is shed by a periodical cavity scale re-entrant jet, forming cavitation clouds. The collapsing cloud forms the cavity scale re-entrant jet. Cloud cavitation is usually the most damaging type of cavitation. [4; 26; 76]

A sheet cavity differs from separate travelling bubbles as it is a continuous or pseudo-continuous vapour-filled wake. A sheet cavitation generally occurs in the region of laminar to turbulent boundary layer transition, when the cavitation number is low enough. If the boundary layer is initially laminar, the cavitation inception typically happens after the region of lowest pressure in the hydrofoil. A sharp edge with a sufficient incident angle causes the boundary layer to be turbulent from the beginning and the cavitation to occur instantly. [77]

The length of the sheet cavity increases as the cavitation number decreases. In the case of a hydrofoil, when the cavity length increases to a value above the foil length, closure happens outside the hydrofoil. This phenomenon is called supercavitation. Cavitation cloud shedding in a hydrofoil happens roughly with a sheet length around the value of one half of the foil chord length. According to Leroux et al. [78], a sheet cavitation becomes unstable when the cavity length is half of the chord length and it becomes more and more unstable as the cavity length increases. [26]

In the region where the sheet cavity oscillates, cloud cavitation is formed by a re-entrant jet in the upstream direction of the main flow. The re-entrant jet is situated between the sheet and the structure boundary and it typically has a velocity close to the external flow velocity. This re-entrant jet differs from the earlier discussed re-entrant jet in an individual bubble collapse, as its size is in the scale of the entire cavity. The most important factor in the re-entrant jet formation is the adverse pressure gradient in the cavitation closure region. A large adverse pressure gradient is typical for short sheet cavities and it promotes re-entrant jet formation. A small adverse pressure gradient is typical for long cavities, which generally do not show cloud cavitation behaviour. Long cavities are sensitive to external fluctuations, showing large oscillations in cavity length. [26]

The Strouhal number *St* for an oscillating sheet/cloud cavitation is defined as: [26]

$$St = \frac{f_s l_c}{V_\infty} \tag{2.28}$$

where f_s is the shedding frequency, l_c is the cavity length and V_∞ is the external flow velocity. In sheet/cloud cavitation, the Strouhal number typically varies between 0.25 and 0.35. The sheet thickness needs be sufficiently large for the cavity to sustain the re-entrant jet without premature breaking. [26]

For a sheet cavity long enough for cloud cavitation not to occur, cavitation surge may be observed. Cavitation surge is an irregular phenomenon caused by rapid changes in sheet length. The sheet length is sensible to upstream pressure variations in a long cavity. Cloud like structures are formed with a frequency typically less than the comparable cloud cavitation shedding frequency. The shedding may also be periodical, for example in the case of a rotating flow structure. [26]

2.4.3 Cavitating vortices

Flow vorticity caused by turbulence or by solid structures may lead to cavitation in the vortex cores with a cavitation number larger than in a non-rotating flow. The pressure in a vortex core is lower than in the other regions of the vortex, making it possible to a cavitating vortex core to form. As the cavitation forms in the vortex core, it is filled with vapour, limiting the pressure to saturated vapour pressure and causing significant changes in the vortex flow field. [26; 27]

Vortex cavitation is a typical form of cavitation in rotating structures, as the rotation provides circulation for the flow continuously. The rotating structure may for example be a propeller or a turbine runner. Circulation may also be caused by a hydrofoil in a flow, especially when flow detachment is observed. In a submerged jet, a toroidal vortex cavity may form around the main flow.

A vortex forming from a hydrofoil tip is called a tip vortex. The tip vortex begins with zero circulation in the leading edge and increasing circulation with increasing distance downstream. A tip vortex with sufficient vorticity may be cavitating. An important form of tip vortex in hydraulic machinery is the tip leakage vortex, which means vortices forming in the space between blade tips and machine casing. This type of cavitation may cause severe damage to the blade tip. [79]

Periodic cavitation, called the Von-Karman vortex shedding, may be observed in the trailing edges of hydraulic machine blades and guide vanes. The rotation of the machine causes periodic shedding of the flow vortices, leading to low pressures and potential cavitation. Inter-blade vortex cavitation is a type of cavitation that occurs in the area between hydraulic machine blades. Secondary vortices are formed when the guide vane and the blade incident angle are in a certain range. These vortices cause cavitation that is attached to the blades and if the cavitation closure is near a surface, cavitation damage may occur. [4]

A typical type of vortex cavitation in water turbines is the draft tube swirl, also called the draft tube vortex rope. It is a potentially cavitating vortex forming downstream from the turbine, caused by the low average pressure and high circulation of the flow. When running a turbine in its design operating point, the draft tube swirl is non-oscillating and when running it in an off-design operating point, the draft tube swirl tends to oscillate with a relatively low frequency, typically 0.25 to 0.35 times the rotating frequency for a hydraulic turbine. The draft tube swirl occurs in the centre of the downstream flow, so cavitation closure does not cause direct damage to structures. The oscillation of a draft tube swirl may cause high amplitude vibrations in a turbine and the cavitation may cause severe noise. The draft tube swirl is a typical feature in Francis turbines. [4; 80]

2.5 Periods in cavitation erosion

Cavitation erosion in ductile materials can generally be divided into four separate periods: the incubation period, the acceleration period, the deceleration period and the steady-state period. Brittle materials, such as ceramics, may show a different kind of behaviour. Cavitation in brittle materials is beyond the scope of this study. [15; 26; 44]

2.5.1 Incubation period

The incubation or pitting period is the period when an initially virgin surface is subjected to cavitation erosion that covers the surface with plastic deformations. For cavitation studies, the initial surface needs to be sufficiently polished, with virtually no initial work hardening. If the surface roughness is too high, pits may not be visible because they are shallow and if the surface is already work hardened, the incubation period cannot be properly studied as cavitation erosion causes similar hardening as surface finishing.

In most engineering applications, surface requirements are not the same as in cavitation research, so studying the incubation period is relevant only for laboratory materials or machines specifically polished for the purpose. Studying the incubation period provides information about material behaviour and makes it possible to create models for erosion in later stages of cavitation.

In cavitation study, it may be assumed that virtually no mass loss happens before the surface is totally covered with pits. Pitting test analysis is based on pit counting, for which there are several methods, such as contact profilometry, optical profilometry, laser profilometry, optical interferometry and scanning electron microscopy [70]. In this study, a contact profilometer was used to measure surface profiles. The method is described in Chapters 2.5.3 and 4.4. All methods require a chosen cut-off depth to exclude material roughness and pit merging and also to count as many pits as possible.

As the cavitation impacts in a cavitation field are not uniform, the cavitation pits have a certain distribution. Franc et al. [70] propose a Weibull distribution for dimensionless pitting rate:

$$\bar{N} = e^{-\bar{D}^{k_w}} \tag{2.29}$$

$$\bar{N} = \frac{N}{N^*} \text{ and } \bar{D} = \frac{D}{D^*} \tag{2.30}$$

where $\overline{N}$ is the normalized pitting rate, N is the pitting rate, N^* is the characteristic pitting rate, $\overline{D}$ is the normalized pit diameter, D is the pit diameter D^* is the characteristic pit diameter and k_w is the Weibull distribution shape parameter. This distribution correlates well with the experimental results obtained from LEGI cavitation tunnel tests (k=1 with some constants added to equation 2.26) and those from cavitating jet tests (k=0.7). [70]

The characteristic pit diameter D^* is defined as the pit diameter with the most contribution to the surface coverage. Pits smaller than D^* are more common than pits of the size of D^*, but their surface area drops so much that they contribute less to the erosion. Pits larger than D^* have a larger surface area but they are less numerous.

The characteristic pitting rate N^* is the rate of pits forming with the characteristic pit diameter D^*. Both these values are derived from statistical pit distributions. Franc et al. [70] measured and analysed several materials eroded in the LEGI cavitation tunnel. They used different driving pressures in their tests to find out the connection between cavitation aggressiveness and material damage.

The characteristic values are dependent on the cavitation field and of the material tested. The coverage time τ is also essential in characterizing the incubation period. It is defined as the time needed for the surface to be totally covered by pits exactly once. Franc et al. [70] found out that in the LEGI cavitation tunnel, the connection between coverage time τ and flow velocity V_t in the test section is: [70]

$$\tau \propto V_t^{-6,5} \tag{2.31}$$

The characteristic pit size is dependent on the flow velocity as: [70]

$$D^* \propto V_t^{0.75}. \tag{2.32}$$

The coverage time is strongly dependent on the flow velocity, which means that the cavitation erosion evolution is also strongly dependent on the flow velocity. The aforementioned authors had a constant cavitation number in their tests. In the LEGI cavitation tunnel, the cavitation number has an effect on the occurrence of cavitation and the radial location of the maximum erosion region.

2.5.2 Acceleration, deceleration and steady-state periods

After the surface is covered with pits, microscopic cracks start to form in the material surface. Work hardened surface does not deform as much as a virgin surface, so it experiences larger equivalent stresses than a virgin surface. For metals, larger cracks form in the grain boundaries and the material begins to rupture. The transition from incubation period to acceleration period is not abrupt, as some material failure occurs even before the surface is totally covered. The acceleration period continues until the mass loss rate reaches a maximum value.

During the acceleration period, the mass loss rate does not increase infinitely. As the cavitation persists, deeper craters are formed in the surface. These deep craters may trap gas or liquid, and this new medium between material surface and bubble collapses starts to damp the pressure peaks. This causes the erosion rate to decelerate.

After sufficient deceleration in the erosion rate has occurred, the rate begins to approach a constant or a pseudo-constant value. The limit where the deceleration period ends and the steady-state period starts needs to be chosen for the research conducted. During steady-state erosion, all the aforementioned processes coexist in a balance, as long as the flow field stays constant and the material surface geometry does not change significantly. The steady-state period may also show non-linear behaviour in some cases. An example of an idealized erosion curve for the ASTM G32 vibratory erosion testing set-up is presented in Figure 2.6. [44]

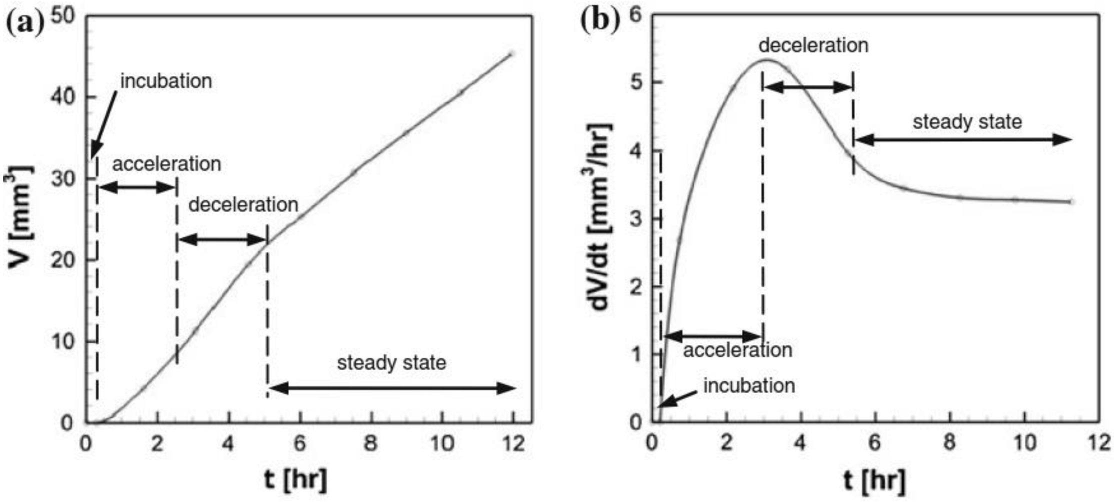

Figure 2.6. *The typical erosion and erosion rate curve for an ASTM G32 device. Curve (a) is for the volume loss and curve (b) is for the volume loss rate. [44]*

The cavitation erosion curve is for most ductile materials an S-shaped curve, if the incubation period is excluded, as observable in Figure 2.6. The volume loss curve may be presented as: [15; 44]

$$\overline{V_{loss}} = 1 - e^{\bar{t}^2} + \frac{1}{e}\bar{t}^{1.2} \tag{2.33}$$

$$\overline{V_{loss}} = \frac{V_{loss}}{V_{loss}^{*}} \tag{2.34}$$

and

$$\bar{t} = \frac{t-T}{t^*} \tag{2.35}$$

The values t^* and V^*_{loss} are material and flow field characteristic values and T is the incubation period duration. $\bar{V}$ and $\bar{t}$ are the dimensionless values for volume loss and time, respectively. The volume loss at $t\text{-}T\text{=}t^*$ equals to V^*_{loss}, which by twice deriving equation 2.33 in time leads to the definition: t^* equals to 4/3 times the time to reach maximum erosion rate. By defining the flow and material characteristic values correctly, the mass loss curves for most materials fall in the same dimensionless curve. [15; 44]

2.5.3 Erosion measurement and calculation

Mass loss in cavitation erosion research may be calculated either by weighing a sample or through volume loss by measuring the changes in the sample surface between erosion periods in the test rig. The weighing method is used in the ASTM G32 vibratory apparatus and in some other cavitation testing apparatus. In this study, the volume loss method is used as the sample mass loss is not easy to measure directly.

The mass loss is in the order of several milligrams as the mass of the entire sample is about 1.2 kg. This means that weighing the sample is an uncertain method as the mass loss due to cavitation erosion may be of the same order as the uncertainty caused by the interaction with the environment. The sample surface measurement provides also other important information about the cavitation erosion development.

As the erosion develops in the sample, the sample surface deforms and starts to rupture. The sample surface may be measured with a profilometer and the resulted profiles may be used to describe the erosion evolution and to compare the erosion behaviour to different materials. If the cavitation erosion area in a sample surface is well defined, a two-dimensional analysis of the surface may be sufficient in erosion calculation.

In cavitation erosion testing, the sample is subjected to cavitation erosion multiple times for certain durations and the sample is measured between these erosion periods. The length of these erosion periods are defined by experience or by assumptions regarding the test setup. In the volume loss method, the sample surface is measured between the erosion periods so that the erosion evolution in time domain may be calculated. The surface is measured with a surface profilometer. In this study, a contact profilometer was used and the surface of the sample was measured along different lines in the radial direction of the circle shaped sample.

A profilometer provides three-dimensional data points. In this study, the planar directions of a surface are referred as x- and y- directions and the erosion depth direction is referred as the z- direction. In this chapter, the index k is used to describe the cumulative erosion time, where $k = 0$ means the time step before erosion and $k = 1$ means the time step index after the first period of erosion in the cavitation tunnel and so on. The volume loss $V_{loss,k}$ for a certain surface and for a certain value of erosion time may be calculated from:

$$V_{loss,k} = -\int_{y_0}^{y}\int_{x_0}^{x_1}(z_k(x,y) - z_{0,k})dxdy \tag{2.36}$$

where y_0, x_0, y_1 and x_1 are chosen surface dimensions to be analysed, z is the depth variable and z_0 is the chosen zero depth level. A profilometer provides a finite amount of data points, so practically the volume loss is calculated as a sum over the analysed surface:

$$V_{loss,k} \approx \sum_{i=1}^{n_y}\sum_{j=1}^{n_x}(z_{i,j} - z_0)\Delta x\Delta y \tag{2.37}$$

where Δx and Δy are the measurement resolutions and n_x and n_y are the amounts of measurement points in x and y –directions and $z_{i,j}$ is the local depth value for a certain measurement point. In theoretical analysis, the zero depth level z_0 should also be a local value as the initial surface of a material is never flat. In this study, however, the surface profile was measured with a contact profilometer that has no means to accurately place the sample in exactly the same position and location in all measurements.

For the circle shaped surface in this study, the volume loss over the sample may be expressed in a two-dimensional circular coordinate system as:

$$V_{loss,k} = -\int_{0}^{2\pi}\int_{r_0}^{r_1}(z(r,\beta) - z_0)drd\beta \tag{2.38}$$

where r the is radius and β is the angle in radians in the two-dimensional circular surface. The volume loss is calculated assuming that the erosion profile is constant with all values of the angle β. The calculation does not give the actual volume loss of the sample. The result is the volume loss if the sample would have eroded uniformly. The whole eroded surface could be measured and the true volume loss could be calculated, but in this study the measurement was limited to several radial lines because of profilometer limitations. With these assumptions, equation 2.38 may be written as:

$$V_{loss,k} = -2\pi\int_{r_0}^{r_1}(z(r) - z_0)dr \tag{2.39}$$

and in the sum form:

$$V_{loss,k} \approx 2\pi\sum_{j=1}^{n_r}(z_j - z_0)\Delta r \tag{2.40}$$

where Δr is the resolution in the radial direction. It is equal to Δx as the profile measurements were made in a Cartesian coordinate system, but the actual volume loss calculation is done in the two-dimensional circular coordinate system. The volume loss is calculated between each cavitation erosion period and the values are used to create the curves for volume loss in function of time.

The other studied option was to calculate surface loss along the measured profile. This method does not take into account that in addition to cavitation effects, also the geometric effects have an influence on the eroded profile. The volume loss over the entire sample does not address this problem, though the problem is not relevant if the results are used only to compare materials. The geometric effect in the bubble number density is visualized in Figure 2.7.

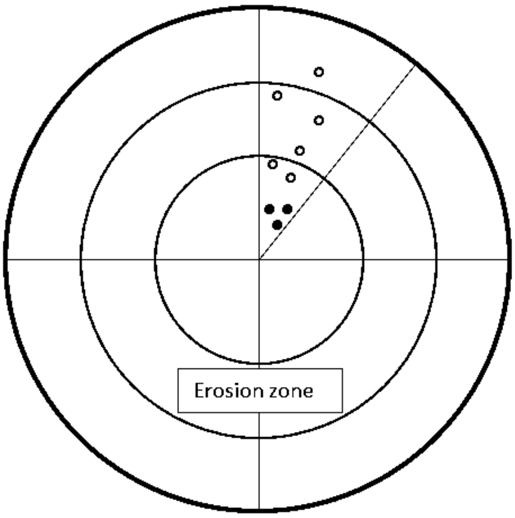

***Figure 2.7**. Visualization of the geometric effect on bubble number density. Filled circles present initial bubbles and the non-filled circles present two potential bubble collapse patterns.*

Due to the geometry effect, the bubble number density decreases with increasing radius. However, the flow velocity decreases also with the increasing radius. This means that the velocity decreasing effect may cause packing of the bubbles as the radius increases. This mechanism may cancel the geometry effect, though further analysis was not made in this study. The pressure increases as the radius increases. This means that the collapse intensity may also increase with radius.

These effects are difficult to take into account in the calculations, so the volume loss needs to be calculated over the whole eroded area. The radius in the maximum erosion zone may not be the same as the radius in the maximum intensity of the cavitation.

In this study, four different sample orientations were always measured to compare results. For all these four orientations, five different positions were used in the *y*-direction. These five measurement lines were 1 µm apart from each other and they were averaged to provide one two-dimensional profile. The averaging procedure for each point in the *x*-direction may be expressed as:

$$z_{i,avg} = \frac{\sum_{j=1}^{n_y} z_{i,y}}{n_y} \tag{2.41}$$

The zero depth level value that the profilometer provides may not be assumed as constant between the measurements. In this study, the actual erosion zone in the sample surface is well defined. The sample surface has a small vertical slope. The slope in the measurements was always less than 10 µm for a distance of 30 mm. The erosion zone length in this study was defined as 8 mm.

With a linear slope assumption, a suitable zero level is the average displacement outside the erosion zone. As the erosion zone is well defined, it may be assumed that there is no erosion outside the erosion zone. The absolute values provided by the profilometer may change between measurements, but the average form of the sample in the non-eroded region remains practically unchanged. The profilometer data has some errors, but with the averaging method, the errors are not significant.

With the averaging method, the zero level for each measurement may be defined as:

$$z_0 = \frac{\sum_{i=1}^{n_1} z_{i,avg} + \sum_{i=n_2}^{n_3} z_{i,avg}}{N_{tot}} \tag{2.42}$$

where n_1 is the index in the beginning of the erosion zone, n_2 is the index in the end of the erosion zone, n_3 is the index in the end of the measurement zone and N_{tot} is the total amount of measurement points outside the eroded region.

With the averaged zero level z_0 for each measurement; the volume loss evolution may be traced in time domain. The volume loss rate in time domain may be defined as:

$$\frac{dV_{loss,k}}{dt} \approx \frac{\Delta V_k}{\Delta t_k} = \frac{2\pi \left. \sum_{j=1}^{n_r} (z_j - z_0)\Delta r \right|_k - 2\pi \left. \sum_{j=1}^{n_r} (z_j - z_0)\Delta r \right|_{k-1}}{t_k - t_{k-1}} \tag{2.43}$$

where $\Delta t_k = t_k - t_{k-1}$ is the time difference between the end and the beginning of measurement number k. The value 0 for the index k corresponds to the measurement of the initial non-eroded surface.

The cavitation erosion in this study has a maximum depth for a certain value of radius. The erosion depth gradually decreases to both radial directions from the maximum point. The evolution of the maximum erosion depth is also traced in time domain to characterize the cavitation behaviour of a material. The volume loss rate and the erosion depth rate usually correspond to each other when comparing materials, but there may be differences between materials.

A single value of profilometer depth data may not be assumed reliable, so the maximum erosion depth has to be an averaged value. The erosion depth along the radial measurement may be averaged with a number of depth values. Along the profile, an average starting from all the data points and up to a chosen amount of data points may be calculated. The largest value may be chosen for the maximum erosion depth value. In this study, the amount of data points for the averaging procedure was chosen so that it corresponds to a length of 200 µm. This value was found to provide reliable values, leaving out the measurement errors but still describing the erosion profile reliably.

The erosion depth vector for measurement number *k* is defined as:

$$\underline{h_k} = \left(\frac{\sum_{i=1}^{datapoints} z_{i,k}}{datapoints}, \frac{\sum_{i=2}^{datapoints+1} z_{i,k}}{datapoints} \dots \frac{\sum_{i=(n_X-datapoints)}^{n_X} z_{i,k}}{datapoints} \right) \tag{2.44}$$

and the maximum erosion depth for measurement *k* is defined as:

$$h_{max,k} = maximum(-\underline{h_k}) \tag{2.45}$$

In equation 2.44, *datapoints* is the chosen amount of data points corresponding to the averaging length.

The maximum erosion depth rate is calculated as:

$$\frac{dh_{max,k}}{dt} \approx \frac{\Delta h_{max,k}}{\Delta t_k} = \frac{h_{max,k} - h_{max,k-1}}{t_k - t_{k-1}} \tag{2.46}$$

Values for both the volume loss and the maximum erosion depth are initially non-zero due to the profilometer measurement procedure. The initial volume loss and maximum erosion depth may be normalized to zero by subtracting the values of the non-eroded sample from all calculated volume loss and erosion depth values.

3. ACOUSTIC EMISSION

3.1 Definition

Chapter 3 describes the basic phenomena linked to acoustic emission (AE) technique. Acoustic emission is defined as the spontaneously released elastic energy that is emitted from materials undergoing deformation. Acoustic emission measurements in the cavitation test were made to study if there is a link between the stage of erosion and the acoustic emission signal.

Acoustic emission may lead to audible noise in some cases, such as in tin cry, but the audible noise is not called acoustic emission. Tin cry is the noise caused by mechanical twinning in pure tin during plastic deformation. These audible noises were the first use of acoustic emission, though the term was defined in 1961 by Schofield. Kaiser's Doktor-Ingenieur dissertation in the year 1950 is considered as the first publication with the use of the modern acoustic emission technique. [81-83]

The difference between acoustic emission and sonic waves is that acoustic emission is defined as elastic waves in a solid medium and that sonic waves are audible or inaudible waves in a gaseous medium. Acoustic emission sensors are placed in contact with the solid medium and the signal is detected from the movement of the solid surface. The movement is detected by a piezoelectric crystal and the output signal is electric. The contact type AE sensor is most commonly used, though non-contact sensors are also available. [81]

Acoustic emission measurements are widely used in structure monitoring. It is a non-destructive method to detect and locate material defects in a structure under loading. The signals are emitted when, under loading, the cracks in a material propagate or when plastic deformation occurs. It reveals defects before they are visible and it provides means to analyse large structures with low cost. [84]

Compared to the ultrasonic method, the acoustic emission method is faster because it analyses the whole structure with one measurement, though it does not provide as much information on the possible defects. Another advantage is that with the AE-method and the stress history of a structure, structural changes may be detected. If a structure is subjected to a certain loading, no further AE-signals are to be expected with loadings inferior to the initial loading. This effect is called the Kaiser effect, named in honour of Joseph Kaiser. [83-85]

In this study, the goal was to find a relation between measured AE and the ongoing cavitation erosion in the test setup. The signal content was expected to differ in the incubation period, the acceleration period, the deceleration period and the steady-state period of cavitation erosion. In the incubation period, mostly continuous signal from plastic deformation was expected and in further erosion periods with significant mass loss, discontinuous signals from crack propagation were expected.

3.2 Acoustic emission sources

Acoustic emission is emitted in a material when stored strain energy is released. This is related to plastic deformation and crack propagation. Possible acoustic emission sources in plastic deformation are twinning and dislocation movement and in rupture; crack propagation. Phase transformations and chemical actions may also act as sources of acoustic emission. These mechanisms have a dynamic, a local and an irreversible nature. [85; 86]

The elastic waves or acoustic emission signals may be classified as continuous signals caused by plastic deformation, phase transformation or friction mechanisms, and as discontinuous signals, also called as burst signals, caused by material failure mechanisms. The failure mechanisms are typically crack propagation and crack evolution. The difference between these signal types is that the discontinuous type has a distinctly discreet nature with higher signal amplitude than that of the continuous type. [86]

The continuous acoustic emission has a finite duration and typically constant or near-constant average amplitude. The plastic deformations causing continuous acoustic emission may only be detected if the signal amplitude is high enough. A single moving dislocation is not detectable. According to Máthis and Chmelík [86], 100 moving dislocations or 10,000 concurrent annihilation of dislocation pairs are required to generate detectable acoustic emission in an ideal situation. Naturally this depends on the material, but the quantities presented give an idea of the event density required. Table 3.1 presents the continuous acoustic emission sources and their significance.

Table 3.1. *Acoustic emission signal sources and intensities. [86]*

Mechanism of plastic deformation	**Strength of AE signal**
Frank-Read source	Strong
Twin nucleation	Strong
Yield phenomenon	Strong
Cutting of coherent precipitates by dislocations	Strong
Orowan bowing	Weak
Twin growth and thickening	Negligible
Grain boundary sliding without cracking	Negligible

The intensities of different AE sources vary with different materials and conditions. The background noise may be at the same level of amplitude as the continuous acoustic emission, so proper thresholding and data analysis is required to distinguish noise from target signal. A material experiencing strain has the largest AE-signal amplitude just above the ultimate strain [82]. According to Spanner et al. [87], a typical frequency range for acoustic emission measurements is from 10 kHz to 1 MHz, though some measurements prove that signals may be recorded at over 50 MHz frequency.

The discontinuous acoustic emission signals from crack propagation or sudden pressure pulses are fairly easily detected as their amplitudes are typically far larger than that of the background noise. When measuring discontinuous AE, measurement triggering is typically used. Acoustic emission waveform data requires lots of space so the background noise is not measured unless the triggering condition is met. Measurements in engineering applications may contain both the continuous and discontinuous type of signals, so the thresholding and triggering conditions are case-sensitive.

Figure 3.1 shows the two types of acoustic emission signals. The discontinuous signals are also called as burst signals.

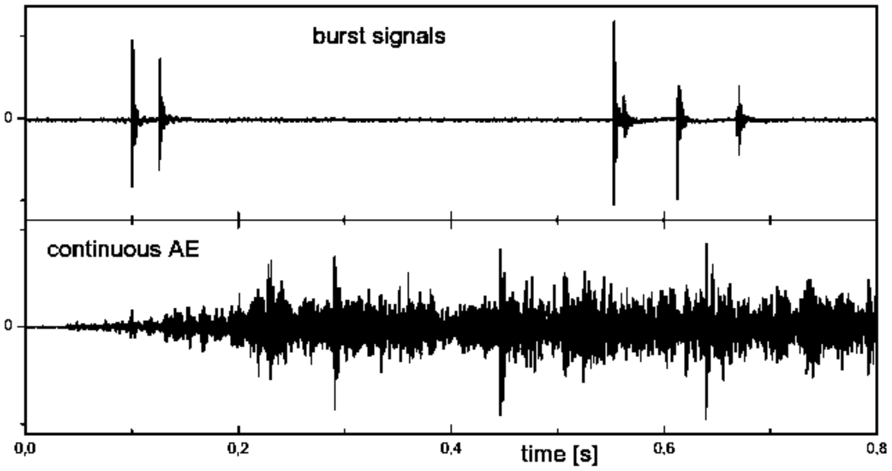

Figure 3.1. *The difference between discontinuous and continuous acoustic emission signals. [84]*

In this study, acoustic emission was measured from a sample that is experiencing cavitation erosion. Generally in acoustic emission testing, cavitation is considered as signal noise. However in this study, it is the actual target parameter to be measured. The acoustic signal from cavitation has high amplitude and it is difficult to separate continuous signals and discrete discontinuous signals with small difference in time.

The Kaiser effect, already mentioned in Chapter 3.1, is a phenomenon used in structure surveillance. A structure that has never been subjected to a load emits acoustic signals when it is loaded for the first time, even if it is defect-free. A defect-free structure, however, does not emit acoustic signals when the first load is removed and when a similar load is applied the second time. Applied loads that are smaller than the first load and that cause acoustic emission may be interpreted as defects in the material that has appeared after the first loading. This is called the Felicity effect. The Felicity ratio Fr is defined as: [84; 85]

$$Fr = \frac{P_{AE}}{P_{initial}} \tag{3.1}$$

where P_{AE} is the loading where acoustic emission occurs and $P_{initial}$ is initial structure loading. If the Felicity ratio is equal to or larger than 1, new defects in a structure are not observed. If it is below 1, material degradation in some form has occurred between the loadings. The first loading can be done when the structure is first put to operation and the second one after a suitable period of time. If the Felicity ratio is found to be below 1, the structure may be decommissioned, repaired or at least inspected. The Kaiser effect is not applicable in this study, but it is an important concept in the acoustic emission technique. [84; 85]

3.3 Acoustic emission wave propagation

As the acoustic emission signal is defined as elastic waves in a solid material, the wave propagation and attenuation mechanics are important features to be studied. The form of a stress wave remains constant only in an infinite, isotropic, ideally elastic and homogenous medium. In this type of medium, only two types of stress waves can exist; longitudinal stress waves and transverse stress waves, also called as shear waves. In Figure 3.2, the differences between these two wave types are illustrated. [88; 89]

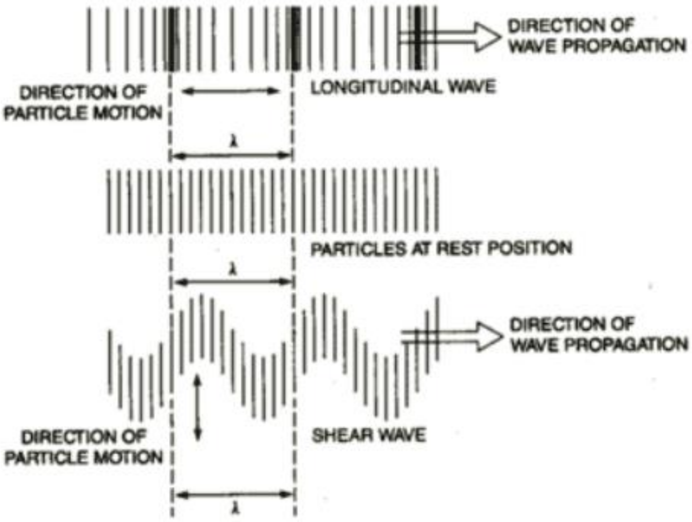

Figure 3.2. *The differences between longitudinal and transverse stress waves. Transverse waves are also called as shear waves. [90]*

In the longitudinal wave the particle motion is either codirectional or opposite than the direction of wave propagation. In the transverse wave, the particle motion is perpendicular to the direction of wave propagation. [89]

The displacement vector $\underline{u}$ of a propagating wave is defined as: [91]

$$\underline{u} = f(x\underline{p} - ct)\underline{d} \tag{3.2}$$

where *f* is the external force applied to the medium, $\underline{x}$ is the position vector, $\underline{p}$ and $\underline{d}$ are unit vectors defining the movement direction, *c* is the speed of the propagating wave and *t* is time. The differential equation of motion for the displacement vector $\bar{u}$ is of the form: [91]

$$\mu_L \nabla^2 \underline{u} + (\lambda + \mu_L)\nabla\nabla \cdot \underline{u} = \rho \underline{\ddot{u}} \tag{3.3}$$

where μ_L and λ are Lame's elastic constants and ρ_m is the material density. ∇^2 is the Laplace operator ∇ is the gradient operator and the Lame's elastic constants are defined as: [91]

$$\mu_L = \frac{E}{2(1-\nu)} \tag{3.4}$$

and

$$\lambda = \frac{E\nu}{(1+\nu)(1-2\nu)} \tag{3.5}$$

where *E* is the material Young's modulus and *v* is the material Poisson's ratio. The solution of equation 3.3 gives as a result the velocities and types of the two aforementioned waves in the infinite, homogenous, isotropic and ideally elastic medium. The speed of the longitudinal wave is always larger than that of a transverse wave. The ratio between the velocities of the longitudinal wave and the transverse wave is: [91]

$$\frac{C_L}{C_T} = \left(\frac{\lambda + 2\mu_L}{\mu_L}\right)^{\frac{1}{2}} = \left[\frac{2(1-\nu)}{1-2\nu}\right]^{\frac{1}{2}} \tag{3.6}$$

where C_L is the velocity of a longitudinal wave and C_T is the velocity of a transverse wave. Equations 3.2 to 3.6 describe the wave motion in an ideal situation, which is not the case in practical acoustic emission measurement or in any real situation. When a free surface exists in the system, additional types of waves are observed. One example is the Rayleigh wave.

The Rayleigh wave is a surface wave that travels in the boundary of a free surface and an elastic half-space. It is also strongly confined to the boundary. The displacement caused by a Rayleigh wave decreases exponentially with the distance from the free surface. The velocity of a Rayleigh wave can be approximated as: [91]

$$C_R = \frac{0.862+1.14\nu}{1+\nu} C_T \tag{3.7}$$

where C_R is the velocity of a Rayleigh wave. The wave velocities may be used to characterize the types of waves traveling in a material. This is an important subject in acoustic emission theory and in characterizing the acoustic emission sources. However, this will not be further studied in this thesis, as the acoustic emission is not the main point of focus.

3.4 Important features in acoustic emission signals

Acoustic emission measurement devices do not generally store the complete waveform of the signal. The complete waveform signal takes about 1 GB/min of hard-disk space, depending on the sampling frequency, so it cannot be used in continuous surveillance for a long time [86]. It also takes relatively much computing time to post-process large amounts of raw data. This is why the raw data signal is pre-processed in continuous surveillance. According to Spanner et al. [87] following parameters are typically extracted from an acoustic emission signal: the emission event, event pulse count, event energy, signal amplitude, signal duration and signal rise time.

The acoustic emission event is defined as an acoustic signal exceeding the threshold strength value once or multiple times, presumably originating from one single source. The event starts when the threshold value is exceeded and it ends when the signal amplitude goes below the threshold value for the last time. A typical burst type signal oscillates several times around zero with amplitude over the threshold value, reaching maximum amplitude and then diminishing to a value below the threshold. In Figure 3.3, the typical extracted parameters from a single acoustic emission event are presented.

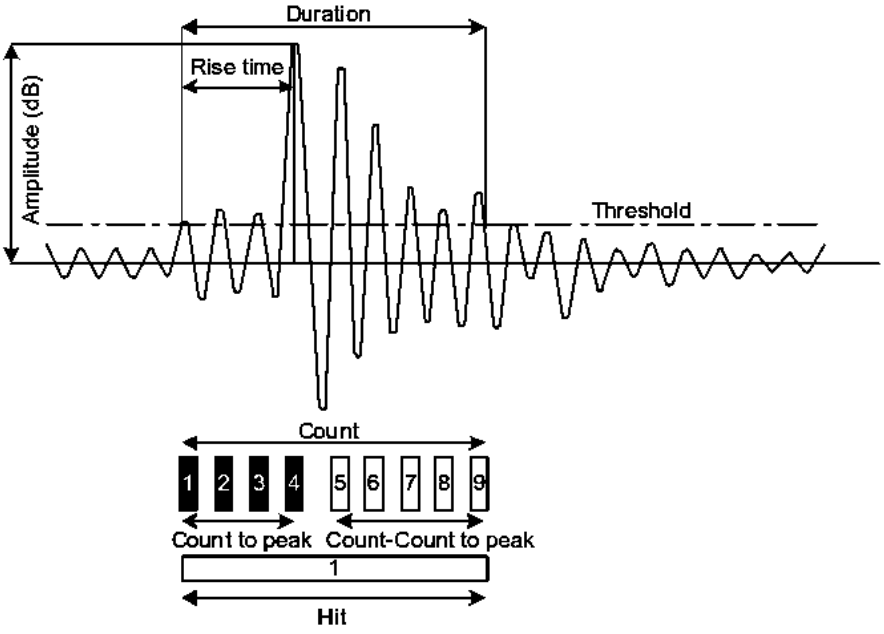

Figure 3.3. *Typical extracted parameters from an acoustic emission event. [92]*

For a continuous signal, the following features may be calculated from the signal data: root mean square value of the signal, frequency content of the signal and other statistical data that is needed. The root mean square (RMS) value of the signal means is calculated as the square root of the average of the squared values of the signal output voltage:

$$V_{RMS} = \sqrt{\frac{1}{n_V}\sum_{i=1}^{n_V} V_i^2} \tag{3.8}$$

where V_i is the output voltage of the signal and n_V is the amount of measurement points in the signal to be analysed. The root mean square voltage can be used to calculate the electric power of a signal. The root mean square voltage of a signal corresponds to the actual signal source better than the average of the absolute amplitude values. Increase in the root mean square voltage corresponds to increase in the signal source strength.

The frequency content of a signal is obtained with a Fourier transform, typically using the fast Fourier transform (FFT) algorithm. The FFT-analysis provides the amplitudes of each signal frequency. In an acoustic emission signal, one type of event typically emits a signal in a certain frequency range, so the frequency content may be used to classify the type of events occurring in the target material.

The FFT-analysis allows the filtering of frequencies that are expected to be caused by noise coming from various sources. The disturbing noise may be from electromagnetic disturbances, from different kinds of frictional vibrations or from different flow phenomena if there is a liquid flow in the sensor measurement area. Cavitation is normally considered as noise in an acoustic emission signal, but for this study, it is one of the signals to be studied. Acoustic emission events typically have a relatively high frequency, so high-pass filtering may be used to exclude frequencies lower than those from the sources that are interesting for the study.

3.5 Acoustic emission measurement

The acoustic emission sensors are typically cylindrical and they have one electrical output for the signal. They consist of a piezoelectric (PZT) element, a connector, housing and a wear-plate. The surface of the wear-plate is the one that touches the structure to be analysed and the piezoelectric element is the component that turns the surface movement signal to electrical signal. The size of an acoustic emission sensor is of the order of some centimetres both in diameter and height. The typical and simplified structure of an acoustic emission sensor can be seen in Figure 3.4.

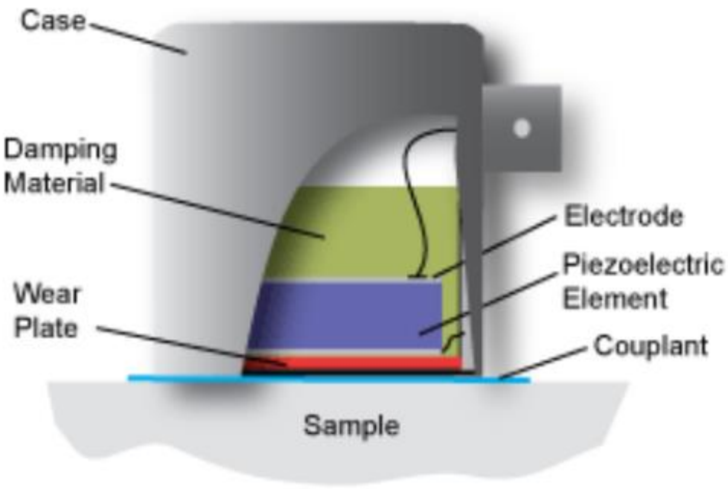

Figure 3.4. *The structure of an acoustic emission sensor. [93]*

Acoustic emission sensors may be classified into two main categories; resonance type sensors and broadband type sensors. A third acoustic emission measurement method is the laser surface displacement measurement method, but it will not be further discussed in this study. The resonance type sensor has one or several resonance frequencies to which the sensor sensitivity is higher than to other frequencies. The broadband type sensor has an approximately constant sensitivity in a large frequency range. The frequency range and the resonance frequencies are sensor specific. [94]

The resonance type sensor is used when there is an estimate for the frequency content of the expected signal and when the signal strength is relatively weak. A resonance type sensor captures small events in a certain frequency range, but it fails to capture separate events with significantly varying frequencies. The resonance frequency is dependent on the piezoelectric crystal mass and the sensor design.

The broadband type sensor is used when a large range of frequencies is expected and when the signal strength is strong enough to be detected with a smaller sensitivity than that of the resonance type sensors. If the signal strength decreases, for example because of a long distance to the signal source or because of material interfaces in the signal path, the broadband type sensor may not be sensitive enough to capture the events. The structure of a broadband sensor is effectively the same as that of the resonance type sensor, the difference being that the broadband sensor is deliberately damped.

The sensor frequency response may differ between sensors of the same type and same manufacturer. This is why all sensors need to be tested separately for their frequency response. The frequency response chart is used to calculate true signal strength from the acquired signal and it is typically provided with the sensor. The resonance frequencies show high amplitude peaks even if they are not actually the frequencies with the largest amplitude in the physical phenomenon.

For the same sensor, signal strength may differ greatly with varying signal path. This is why a calibration is required for the comparability of signals. The acoustic emission sensors that are installed on a surface may be calibrated with several techniques. The goal with each technique is to create a reproducible signal in the target measurement area. With the knowledge from the calibration signal attenuation, the attenuation of the target measurement signal may be calculated.

One way to calibrate an acoustic emission system is metal ball drop tests. Dropping a metal ball from a certain height creates a reproducible signal, if the force and contact time of the ball remain constant. This requires that the material the ball hits is the same between calibration measurements. The signal transmission from the ball drop to the sensor decreases the signal strength, so the signal amplitude may be used to compare the signal paths between tests. [94]

Other possibility is to break something with a near-constant breaking behaviour on the sample. This may be for example a pencil lead or a glass capillary. The pencil lead break signal source is also called as the Hsu-Nielsen source, named after the developers of the testing method. It produces a short duration high amplitude peak and when it is done with the same lead type and same contact angle, the signal stays similar between tests. [87]

The pencil lead break or the Hsu-Nielsen source is considered as a standardized method. It is done with a normal mechanical pencil. The lead that is used in the tests has a hardness of 2H and a diameter of 0.5 mm. The tests are done with a constant lead length outside the mechanical pencil and with a constant contact angle. The lead length and contact angle are not standardized and they need to be chosen for each study separately. The aid of a support may be used to ensure a constant behaviour between lead break events. [87; 95]

4. EXPERIMENT SETUP

4.1 Experiment goals

The main goal of the experiments in this study was to define cavitation erosion resistance of a steel type used in Francis turbine runner blades and to compare the resistance to other materials. The secondary goal was to study if acoustic emission can be used to detect and characterize cavitation in the experimental setup. The sample material was from a decommissioned Francis turbine.

Sample material cavitation erosion evolution was compared to equivalent results obtained from earlier experiments. Further studies will be made with other turbine materials. The experiments made with the PREVERO (prévision de l'érosion) loop high speed cavitation tunnel combined with material nanoindentation tests and compression tests can be used for advanced cavitation erosion testing and modelling. The use of acoustic emission has not been previously studied with the PREVERO cavitation tunnel.

The material sample was cut from a Francis turbine runner blade. The turbine was used in the Imatra hydropower plant in south-eastern Finland. The Imatra power plan is run by Fortum Power and Heat Oy and the turbine in this study was decommissioned in 2014. The Francis turbine in question was manufactured in the year 1930 and it was replaced with a stainless steel turbine. The turbine rated power was 21 MW, the rated head was 24 m, the rated discharge was 120 m^3/s and the rotation speed was 125 rounds per minute.

The interest to study such a material is that similar non-stainless steel turbines are still used in power plants. The comparison of cavitation erosion resistance with the stainless steel turbine materials is useful as steel can be used as a reference material. In further studies, similar experiments will be conducted for at least two different stainless steels used in modern turbines.

4.2 Sample preparation

One sample for cavitation tests and 11 small samples for material characterization were prepared for this study. The samples used in the PREVERO device are 10 cm diameter disks with a 2 cm thickness and they have a screw thread for mounting. For this study, an additional screw thread was added to the samples for acoustic emission sensor mounting. Figure 4.1 shows the dimensions and surface requirements of the samples.

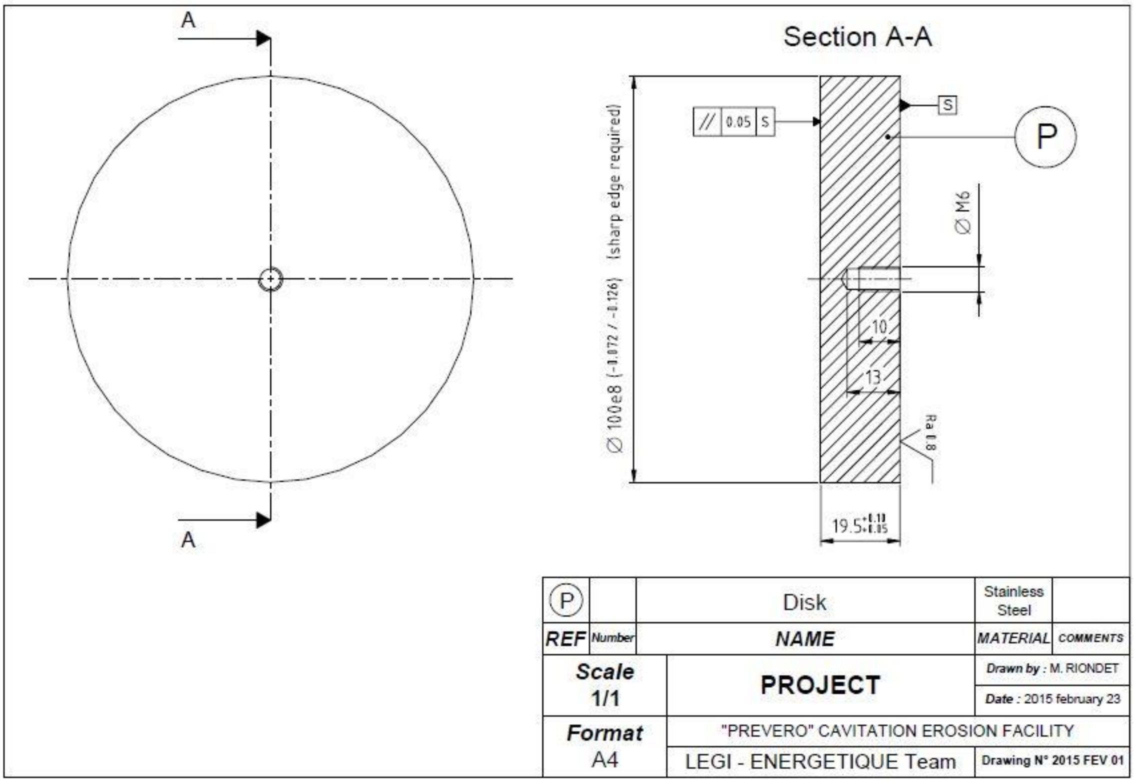

Figure 4.1. Cavitation erosion test sample details. [96]

As seen in Figure 4.1, the sample surface needs to be well polished to remove any hardening that is left from machining the samples, especially if the incubation period is to be studied. Too high surface roughness might cause difficulties in pit counting, as the cavitation pits may be of the same magnitude as of the roughness. The screw thread in Figure 4.1 is used for sample mounting. The acoustic emission sensor used in this study was situated 24.5 mm from the centre and it was mounted with the use of a waveguide that had screw fixing.

The samples were cut and prepared in an external company. The level of polishing reached by the external company was not sufficient, so the samples were further polished in SIMaP (Science et Ingénierie des Matériaux et Procédés) laboratory. The samples were polished with rotating polishing machines using successive diamond pastes. The final superpolishing stage was reached using a 0.03 µm grain colloidal silica suspension and a polishing paper. A mirror type surface was reached.

The 11 small samples used for nanoindentation tests, compression tests and Split Hopkinson pressure bar (SHPB) tests were cylinders with 8 mm diameter and 8 mm height. Five samples were used in the nanoindentation tests and the compression tests and six samples were used in the SHPB tests. The samples for nanoindentation tests and compression tests were polished up to the same surface roughness as the cavitation erosion testing samples. The polished surface was found to be more uniform than in the cavitation samples. This was because the sample size affects the difficulty of the polishing.

4.3 PREVERO high speed cavitation tunnel

The PREVERO high speed cavitation tunnel is a cavitation erosion study apparatus situated in the LEGI (Laboratoire des Ecoulements Géophysiques et Industriels) laboratory. The laboratory is situated in the university campus area of Saint-Martin d'Hères, France. In Chapter 4.3, the operation of the PREVERO cavitation tunnel is presented.

4.3.1 Machine operation

In the PREVERO cavitation tunnel, pressurized water is circulated through a test section by a centrifugal pump. The water circulates from a water tank to a heat exchanger and to the pump. The pump circulates water through measurements of flow rate, pressure difference, absolute pressure and temperature. The water goes through the test section and back to the water tank. Differential pressure is measured over the test section. The test loop is visualised as a flow chart in Figure 4.2 and the test section is visualised in Figure 4.3.

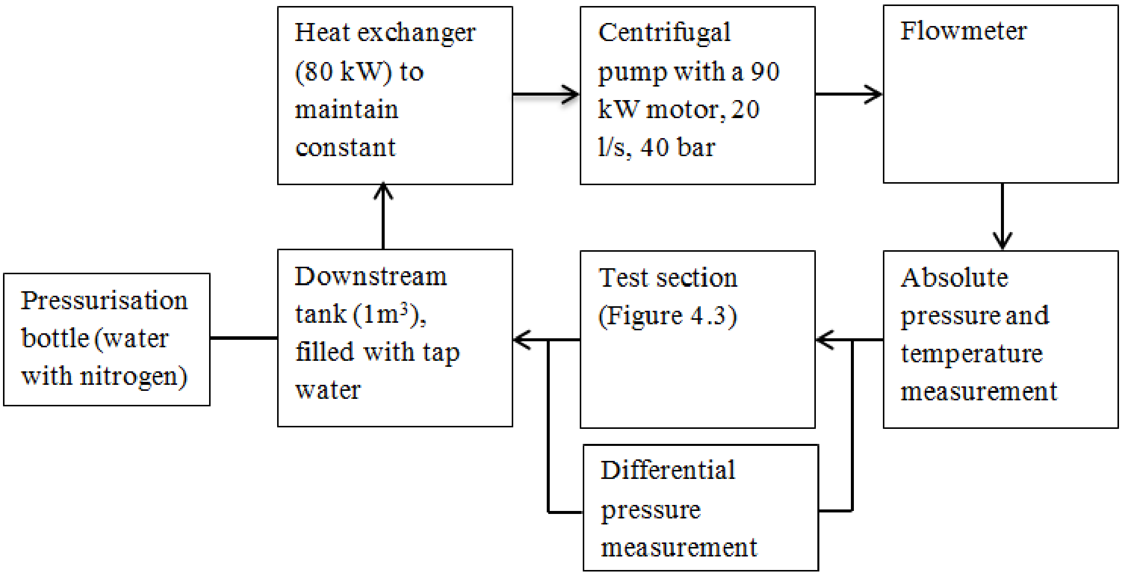

Figure 4.2. *Basic operation principle of the PREVERO cavitation tunnel. The arrows depict the flow direction. Downstream is defined to be after the test section until the pump and upstream is defined to be after the pump until the test section.*

PREVERO cavitation tunnel is operated with a constant temperature, as close to room temperature as the heat exchanger is able to sustain. According to Franc et al. [6], a typical temperature rise is of the order of 0.5 °C for a 5 hour run in the test loop. For a long duration test, the temperature may raise up to 5 °C. The pump is located well below the test section to avoid cavitation in it. The downstream pressure is controlled by a pressurization bottle with nitrogen as the pressuring gas. The upstream pressure is controlled by varying the pump rotation speed with a frequency transformer.

The test section consists of a 16 mm diameter nozzle, pointed towards the material sample. After the nozzle, the test section converges radially in a channel that is 2.5 mm wide. It has four flow collection pipes in the end of the radial section. The test sample is a cylinder with a 100 mm radius and a 19.5 mm thickness, with screw mounting for the sample holder. The sample holder has small screws to adjust the sample in the right plane in the test section. The holder is fixed to the test section and the cavitation tunnel with eight bolts.

The sample is situated in the middle of the radial section so that the high velocity flow from the nozzle hits the sample and forms a stagnation flow that expands radially. The machine is operated so that the flow in the nozzle is non-cavitating and the cavitation inception happens in the beginning of the radial section. The test section is illustrated in Figure 4.3.

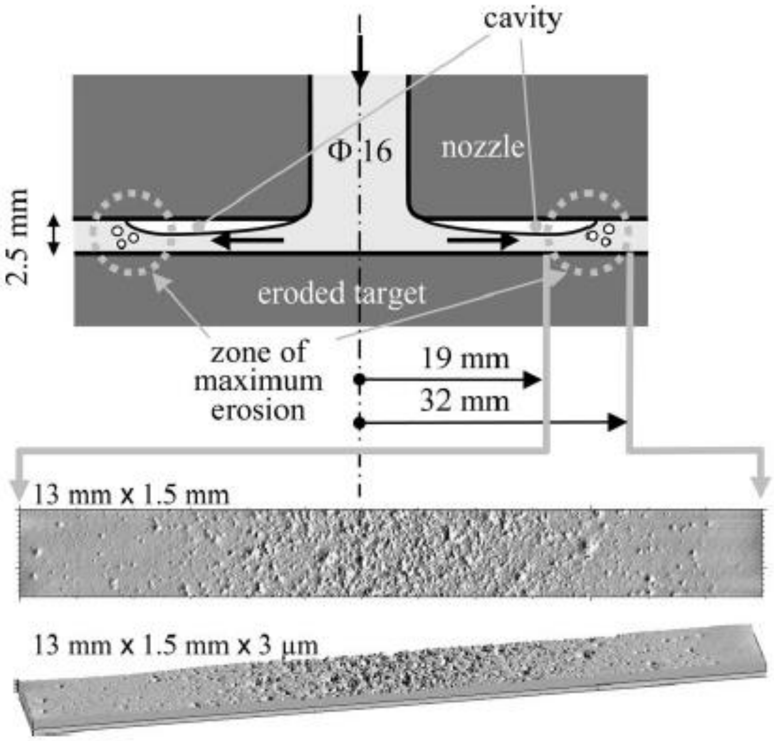

Figure 4.3. *PREVERO cavitation tunnel test section details. [6]*

The highest velocity and the lowest static pressure are located in the point where the flow cross section area is smallest. This point is in the beginning of the radial section after the stagnation point in the middle. From the cavitation inception point, an oscillating sheet cavity is formed. The sheet cavity is of the type that creates cloud cavities, described in Chapter 2.4.2. The cloud shedding frequency of the PREVERO device is unknown.

Equation 4.1 shows the ratio between the nozzle area and the area in the beginning of the radial section:

$$\frac{A_{nozzle}}{A_{radial}} = \frac{\pi(\frac{d_{nozzle}}{2})^2}{\pi d_{nozzle} y_{radial}} = \frac{d_{nozzle}}{4y_{radial}} = \frac{16mm}{4*2.5mm} = 1.6 \tag{4.1}$$

Assuming that the compressibility effects are negligible and using the mass conservation law, the average velocity in the beginning of the radial section is 1.6 times the average velocity in the nozzle. The lowest pressure in the test section appears in the beginning of the radial section, it being the point where cavitation bubbles form. Average pressure increases downstream in the test section and cavitation closure occurs at a point downstream. The point of cavitation closure stays constant with a constant cavitation number. With a cavitation number 0.9, which is the typical operation cavitation number, cavitation closure and maximum damage occurs between radial distances of 19 mm to 32 mm from the centreline. [6]

4.3.2 Measurement parameters

The upstream and downstream pressures are controlled to increase or decrease flow velocity in the nozzle and in the test section. The aggressiveness of the cavitating flow is increased with increasing upstream pressure. The maximum value for the upstream pressure in the device is 4 MPa, which corresponds to a cavity velocity of around 90 m/s [39].

The length of a typical experiment varies greatly with operation parameters and material characteristics. A weak material in terms of cavitation, such as some rubbers, may be tested for several minutes or even less. A strong material in terms of cavitation, such as many steels or metal alloys, may be tested for several hours before damage is visible. If the test is continued up to the mass loss period, the testing times for a strong material may be even up to 150 hours. For almost any test, the erosion profiles are measured several times during the duration of the test, requiring mounting and dismounting of the sample.

The operating parameters of the cavitation tunnel are derived from the cavitation number, which is set to be around 0.9. The parameters have certain tolerances, so the values are not exactly the same between tests. Appendix 1 is the measurement log of the operating parameters in this study. The operating values for non-cavitating region measurements and cavitating region measurements are in the measurement log. The upstream pressure has a maximum fluctuation of 0.2 bars in this study and the cavitation number has a maximum fluctuation of 0.005. The maximum temperature rise during a 4-hour test was 4.6 ℃.

PREVERO device damages the sample surface axisymmetrically, with a ring shaped erosion pattern. In the beginning of the tests, the erosion consists of plastic deformation pits, as explained in Chapters 2.3.1 and 2.5.1 and as the tests go on, the erosion develops towards an increasingly ruptured surface, as explained in Chapters 2.3.2, 2.5.2, 2.5.3 and 2.5.4. The surface is generally analysed with a contact profilometer and for incubation tests, the pits are counted from the profilometer data. For mass loss tests, the mass loss can be calculated from volume loss and material density.

The values of interest are the incubation time T or the coverage time τ, the mean depth of penetration rate *MDPR*, mass loss or volume loss evolution and other values and relations derived from these values. The incubation time may be calculated with a pitting test for a virgin surface, in which the sample is subjected to cavitation for a short period. The mean depth of penetration rate may be calculated from measured surface profiles with an averaging procedure over the eroded surface.

The pitting tests are generally used more to evaluate flow aggressiveness and the erosion evolution tests more to define material cavitation resistance, although they are generally related to each other. Soyama and Futakawa [16] developed a model to predict incubation time with post-incubation measurements for a liquid mercury vessel used in a spallation neutron source and Karimi and Franc [46] proposed a model to predict steady-state erosion rate with incubation time and some material characteristics, as described in Chapter 2.5.2.

4.4 Surface profile measurement

The sample surface was analysed using a Taylor-Hobson model Form Talysurf 50 contact profilometer. The profilometer characteristics are listed in Table 4.1.

Table 4.1. *Profilometer characteristics.*

Maximum resolution, *y*-direction	1 µm
Maximum resolution, *x*-direction	0.5 µm
Resolution, *z*-direction	3.2 nm
Profilometer tip	90° conical tip ending with a 2 µm radius sphere

The profilometer data output is in Cartesian coordinates. x-direction corresponds to the radial direction of the sample, y-direction corresponds to the other planar direction on the surface and z-direction corresponds to the varying depth.

The sample surface profile in the maximum erosion area was measured after each testing period. The circular sample surface was divided into four equal parts by two lines passing through the centre of the circle. The erosion was studied in four directions starting from the centre point: 1: the 0º, 2: the 90º, 3: the 180º and 4: the 270º line. The orientations are visible in the sample photographs in Chapter 5.3.1. The surface profile was always measured along these four lines. For all four lines, five lines with a 1 µm difference in the *y*-direction were measured to exclude possible problems with dust or measurement errors. The five lines close to each other were averaged for the volume loss and erosion depth analysis of the sample.

The surface profile was always measured along the same lines on the sample surface. The profile was measured from 8.5 mm to 38.5 mm in the radial direction from the sample. 60001 measurement points were taken from the 30 mm distance, so the *x*-resolution was 0.5 µm. The *y*-direction was measured from -2 µm position to +2 µm position in five lines so the *y*-resolution was 1 µm.

In the incubation period, surface profiles were also measured with more lines in the *y*-direction to create a continuous surface profile. The surface was always measured around line 3 and the area was 2 mm x 6 mm. In both directions, the maximum resolution was used so in the *x*-direction, there were 12001 measurement points and in the Y-direction, there were 2001 measurement points. Figure 4.4 is the surface profile obtained from the sample after 2 minutes of cavitation erosion.

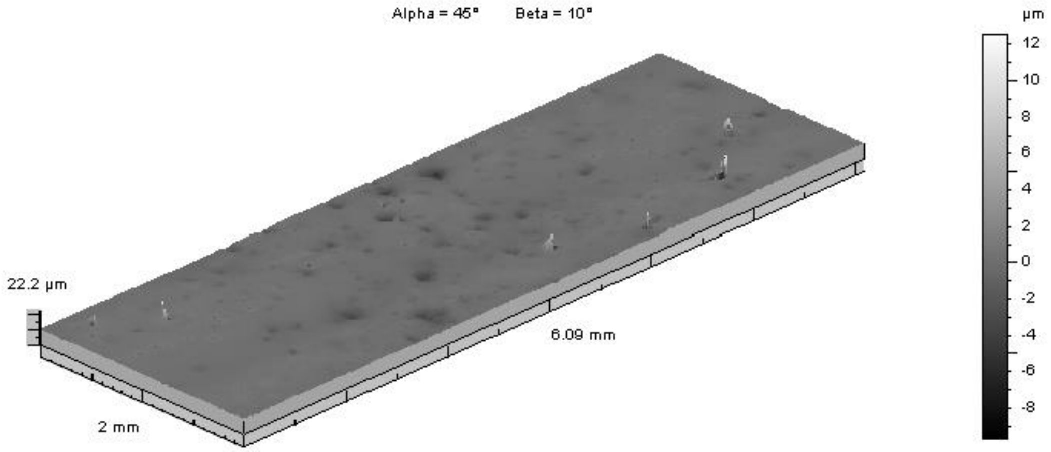

Figure 4.4. *Sample surface after 2 minutes of cavitation erosion in the PREVERO cavitation tunnel.*

In Figure 4.4, five or six pits are detectable. These pits may be assumed to be caused by single cavitation bubble collapses. The incubation period surface profiles could be used for pit counting and incubation period characterization. Pit diameter, volume and count can be calculated with MATLAB, using a specific code. From the pit counting, the pitting rate may be calculated. The pitting rate is defined as:

$$Pitting\ rate = \frac{Pits}{Area*Time} \tag{4.2}$$

The pit radius and depth are not constants so the pitting rate does not give all information for the incubation time calculation. The pit count method was not used in this study, as the erosion evolution was the main focus. The pit count method will be applied in further study and it may be used in material cavitation response modelling. Roy [8; 9] applied this method to calculate single bubble collapse pressures by using an inverse finite element method.

4.5 Acoustic emission measurement

As already mentioned in Chapter 4.2, the acoustic emission sensor was mounted to the material sample with the use of a waveguide, because the sensor could not be fitted directly to the sample surface. The acoustic emission measurement was planned not to interact with the normal PREVERO cavitation tunnel test procedure. The goal of the setup was to capture acoustic emission signals originating from cavitation impacts and material deformation and to attempt to identify different stages and characteristics of cavitation erosion.

4.5.1 Measurement setup

The acoustic emission sensor was a cylinder of a 20 mm diameter and of height between 16 mm and 20 mm depending on the manufacturer, with an electric output in its side and containing a piezoelectric crystal. Several sensors with different frequency responses were used in the experiments to find the best one for the present study. The sensor cannot be mounted directly to the surface of the material sample because of the physical space limitations of the sample holder. The sample holder had a 16 mm hole for instrumentation located 24.5 mm in the radial distance from its centre.

The waveguide was a metal rod attached to a plastic sensor container. The waveguide was fixed to the material sample with a M8 screw thread and the sensor was fixed to the other end of the metal rod with a spring load. The metal rod had a total length of 110.9 mm the length of the M8 screw thread was 9.2 mm. The rod diameter was 12.0 mm. The length of the part of the rod outside the plastic container may be adjusted. Fixing the waveguide to the sensor and the material sample requires grease to reduce signal weakening in all the interfaces in the signal path.

The signal from the sensor was amplified by a Brüel & Kjær AE preamplifier Type 2637 with three possible filters; linear, 200 kHz and 800 kHz. The linear filter can be used in any tests, the 200 kHz filter is suitable for the Brüel & Kjær sensor type 8313 and the 800 kHz filter is suitable for the sensor type 8314 [97]. The 200 kHz filter was also used with the Fujicera 1045S sensor. From the amplifier, the signal goes through a power source and to a data acquisition unit.

The data acquisition unit was an IOtech WaveBook/512 12-bit 1 MHz data acquisition system and it was connected to a computer with a parallel cable. The data was processed with the IOtech WaveView data handling program. The data may be further analysed with most programs able to handle numerical data. The data acquired is raw signal data. In this study, the HBM nCode program was used to post-process the signals. The key parameters derived from the signal data are listed and explained in results in Chapter 5.

The first cavitation erosion experiments in the PREVERO cavitation tunnel proved that the signal strength from the sensor and preamplifier was too high. This signal overflow meant that the results from the first measurements were not useful and that a method to decrease the amplitude had to be applied. An additional resistance unit was placed between the preamplifier power source and the data acquisition unit. The resistance unit has four options: 18 kΩ, 67 kΩ, 118 kΩ and 550 kΩ resistances. The acoustic emission test setup is presented in Figure 4.5.

Data acquisition unit. The unit has an external power source and a grounding cable which are not visible in the picture.

From right to left: signal preamplifier, preamplifier power source and external resistance

Acoustic emission sensor mounted to waveguide

Measurement computer. The data-acquisition is controlled by the IOTech Waveview program.

Sample holder and sample. The waveguide is fixed to the sample through the holder and with a screw thread.

Figure 4.5. *Acoustic emission measurement setup with the sample and the sample holder.*

In Figure 4.5, the signal path may be observed. The area in the sample that is not rusty is the area where cavitation erosion is the strongest. The cavitation bubbles collapse throughout the flow cross-section so all of them do not damage the surface. The bubble collapses that cause material damage were expected to produce a significantly larger signal than those collapses which do not damage the sample.

The signal travels through the sample and the first interface is the waveguide mounting. The interface has metal to metal contact and metal to grease to metal contact. After that, the signal travels through the waveguide. In the end of the waveguide is the sensor, also coupled with grease to decrease signal attenuation.

4.5.2 Sensor characteristics

Several sensors were used and tested in the experiments. The sensors were tested in the beginning of the tests in this study and the most suitable was chosen for the remaining measurements. The sensors and their characteristics are listed in Table 4.2. Only two of the sensors, the Brüel & Kjær type 8313 and the Fujicera type 1045S were used and tested for the cavitation tests.

Table 4.2. *Acoustic emission sensor characteristics.*

Sensor manufacturer	Brüel & Kjær	Brüel & Kjær	Fujicera	PAC
Sensor type	8313	8314	1045S	A3-1668
Serial No.	1689484	1760758	0730	-
Reference sensitivity at (°C)	23	24		
Resonance frequency (kHz)	220	960	-	30
Frequency range (kHz)			200-1300	15-55
Voltage sensitivity (dB, 0 dB=1V/m/s)	64	37	51±3	83
Frequency response in Fig.	4.1	4.1	4.2	-

The frequency responses for each of the sensors are presented in Figures 4.6 and 4.7. The frequency response for the PAC A3 sensor was left out from the study as its best sensitivity is with frequencies under 100 kHz, which is below the expected important frequencies from the acoustic emission testing. For this reason, the sensor was not tested for use in the experiments.

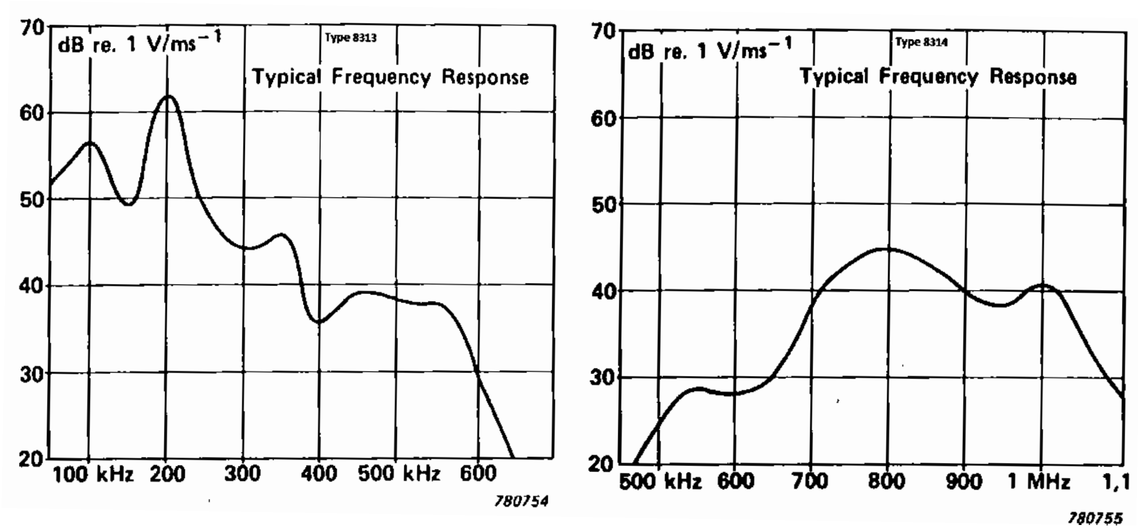

Figure 4.6. *Frequency responses for the Brüel & Kjær 8313 and 8314 AE-sensors. [98]*

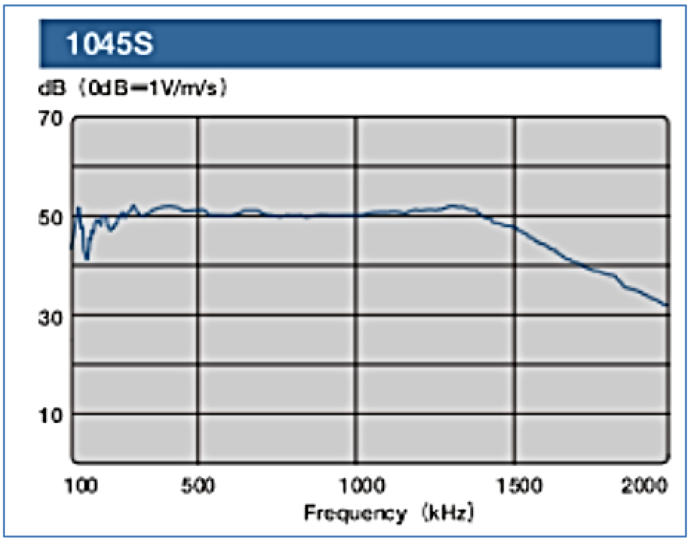

Figure 4.7. *Frequency response for the Fujicera 1045S AE-sensor. [99]*

The frequency response charts show the difference in the sensor types. The Fujicera 1045S sensor has a flat frequency response and the others have higher sensitivities in either one or several frequencies. The Fujicera 1045S sensor may be classified as a broad bandwidth sensor and the other sensors as resonance type sensors.

The data acquisition unit is only able to process frequencies up to 500 kHz. The Brüel & Kjær 8313 sensor was first used in the test, but later on the sensor was changed to Fujicera 1045S. The initial reason to change the sensor was the problems with signal overflow, though the change did not solve this problem. However, the Fujicera 1045S sensor was still used because of its flat frequency response. The flat response makes it easier to analyse the frequency domain results and the signal strength from the tests is strong enough for a flat frequency response sensor.

The Brüel & Kjær 8314 sensor was left out from the tests because its high sensitivity region starts from frequencies around 500 kHz, which is at the upper limit of the data acquisition unit capacity. For a data acquisition unit with a higher frequency range, the Brüel & Kjær 8314 sensor could be used.

4.6 Material characterization tests

The material used in this study was tested for basic material characteristics in addition to the cavitation tests. Nanoindentation and compression tests were conducted on the material to define the low strain rate stress-strain curves. Nanoindentation results are considered to correlate better with cavitation impact results, as the cavitation impacts affect only a small area [8; 100; 101]. Compression tests were conducted to verify the results obtained from the nanoindentation tests and to evaluate material strain rate sensitivity when combined with the Split Hopkinson pressure bar (SPHB).

The material characterization was initially done to be able to predict erosion evolution with equation 2.27. This proved to be too complicated for this study, as it requires more material data and possibly finite element calculation for the mean amplitude of impact stresses. This approach was left for further study and the material properties were used to material classification. The results were also compared with material properties from the previous materials tested in the PREVERO cavitation tunnel. The material properties were compared to the cavitation erosion resistance for the tested material and the compared materials.

4.6.1 Material density

The material density was calculated from the physical dimensions of two of the small cylindrical samples. The sample height and diameter was measured with an electronic caliper with the accuracy of 0.01 mm. The sample mass was measured using a scale with the accuracy of 0.1 mg. The density was calculated to be about 7800 kg/m^3.

4.6.2 Compression tests

Macroscopic compression tests were conducted with a compression device in the SIMaP laboratories. The compression tests were conducted with three different strain rates for three small material samples. The samples were cylinders with 8 mm diameter and 8 mm height, as already described in Chapter 4.2. The measurement parameters are listed in Table 4.3.

Table 4.3. *Compression test measurement parameters.*

Test Nº	**Sample initial diameter (mm)**	**Sample initial height (mm)**	**Strain rate $\dot{\varepsilon}$ (1/s)**	**Maximum force (kN)**	**Data acquisition frequency (Hz)**	**Sample height after compression (mm)**
1	8.20	7.71	$7.795 \cdot 10^{-4}$	75	10	4.17
2	8.24	7.78	10^{-2}	75	100	4.30
3	8.20	7.79	1	75	6144	4.10

The stress-strain curves from each strain rate were compared to observe differences. The strain rates in the compression tests were from 3 to 6 orders of magnitude lower than those of the split Hopkinson pressure bar tests. The results from each of these tests were also compared with the nanoindentation results.

As the sample deforms in a compression test, the contact area to the compressing piston does not remain constant. The data output of the compression test machine used in this test is the force in function of displacement. The zero point of displacement is the displacement where the compressing piston touches the sample. Stress is defined as:

$$\sigma = \frac{F}{S_c} \tag{4.3}$$

where F is the force applied to the sample and S_c is the actual contact area of the applied force. As the sample material is steel, it may be assumed that its density and therefore its volume remain practically constant during the compression test. Also the shape of the sample was observed to remain near constant. There is some visible barrelling of the sample, but it was considered negligible. Barrelling is the effect of the sample cross section area to be increased more in the middle of the sample than in the edges of the sample. Figure 4.8 is the photograph of a non-compressed sample and a compressed sample.

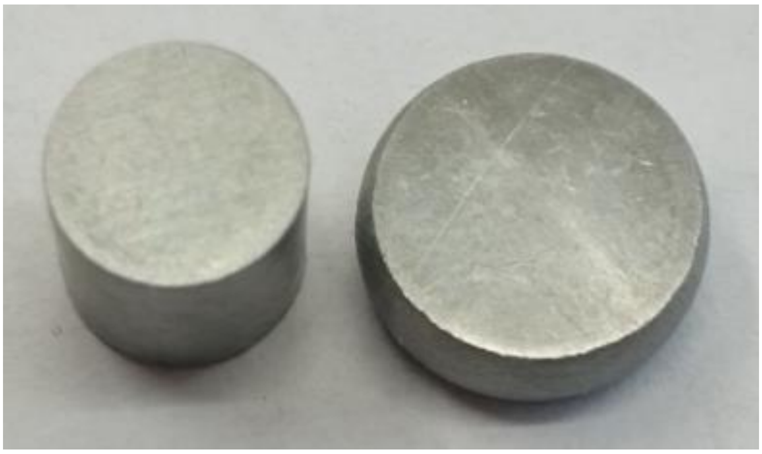

Figure 4.8. *Photograph of a non-compressed sample and a compressed sample.*

In Figure 4.8, the compressed sample is already removed from the compression test device. The barrelling effect may be seen but it is small compared to the total volume of the sample. As the shape may be assumed to remain cylindrical and the material density to be constant, the volume of the sample remains constant:

$$S_{c,o}L_0 = S_cL \tag{4.4}$$

and

$$S_c = \frac{S_{c,0}L_0}{L} = S_{c,0}\frac{L_0}{L_0+d} \tag{4.5}$$

where $Sc_{,0}$ is the initial non-compressed sample contact area, L_0 is the initial sample height and d is the displacement. For compression, the displacement d is a negative value and for traction, it is a positive value. Equation 4.3 combined with equation 4.5 gives the equation for the true stress in compression and in traction testing:

$$\sigma_{true} = \frac{F}{S_0}(1+\frac{d}{L_0}) \tag{4.6}$$

As the displacement d is negative for compression testing, the true stress is always smaller than the so called engineering stress $F/S_{0.}$ Strain is defined in equation 2.15. The general equation for strain does not give the true strain in a compression test or in a traction test with large deformation. The strain in infinitesimal form may be written as:

$$d\varepsilon = \frac{dL}{L} \tag{4.7}$$

By integrating equation 4.7 over the strain distance, true strain is obtained:

$$\varepsilon_{true} = \int_{L_0}^{L} d\varepsilon = \int_{L_0}^{L}\frac{dL}{L} = \ln\left(\frac{L}{L_0}\right) = \ln\left(\frac{L_0+d}{L_0}\right) = \ln\left(1+\frac{d}{L_0}\right) \tag{4.8}$$

The term d/L_0 is called the engineering strain. For compression testing, d is negative so the values for true strain and engineering strain are also negative.

From the compression test output values, it is possible to calculate the values of true stress and true strain and to plot the true stress in function of true strain. Figure 4.9 is an example of such a curve.

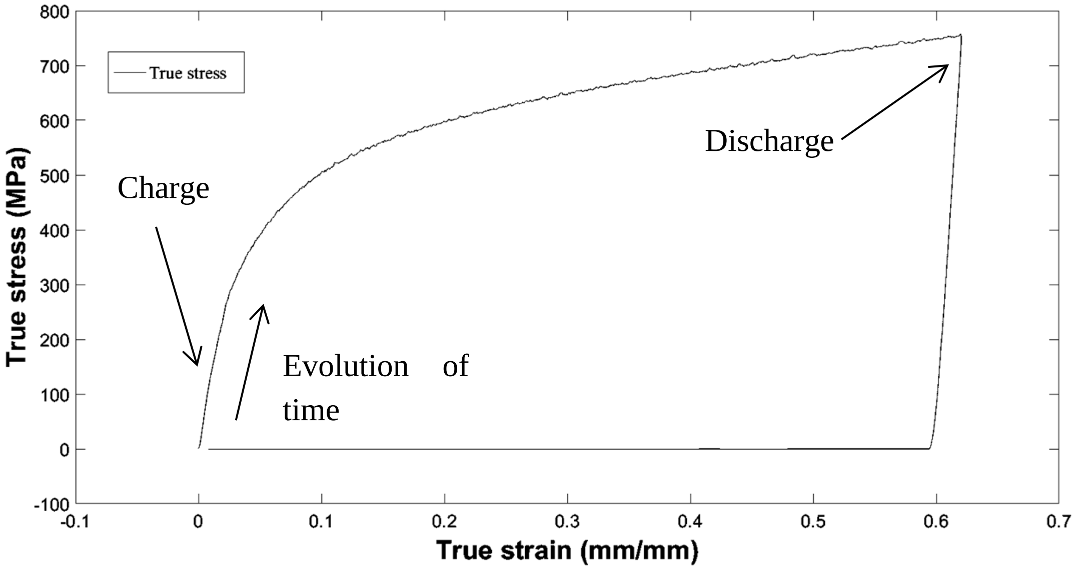

Figure 4.9. *True stress in function of true strain from the compression test with a strain rate of 10^{-2} 1/s. The curve begins from zero loading and the load is increased up to 75 kN load. After this, the load is discharged. This corresponds to the curve data after the maximum true stress.*

The curves from the compression tests had some errors in the beginning of the compressions, probably due to sample surface inequalities. These inequalities lead to uneven loading in the beginning and to values of Young's modulus that are lower than literature values. The Young's modulus is defined as the slope of the linear part of either the charge or discharge curve.

The yield stress was determined visually from the true stress-true strain curves as the stress value in the point where the linear part of the charge part of the curve ends. The visual method is not the most accurate but as the beginning of the curve was faulty due to the inequalities in the sample surface, there was no better option available. The Young's moduli were calculated from the slope of the discharge curves, though the values were not considered to be reliable.

4.6.3 Nanoindentation tests

A single cavitation collapse affects only a small area of a surface. The area is small enough for the collapse pressure to attack only a single phase in a surface that has multiple phases. Grain structures and grain boundaries have different material properties. A material in a cavitation field is thereby mostly eroded in the weakest grain structure. This is why nanoindentation test results correlate better with cavitation erosion results than those of macroscopic compression tests.

The nanoindentation tests were conducted with a MTS Nano Indenter XP in the SIMaP laboratories. The tests were conducted with a spherical indenter of 9.46 μm radius and with two different indent depths, 1 µm and 2 µm. The indenter was a single crystal diamond indenter with a Young's modulus of 1141 GPa and a Poisson's ratio of 0.07.

A testing matrix of 10x10 indents for the 1 µm depth and a testing matrix of 10x3 indents for the 2 µm depth were used. For both the indent depths, the distance between the indents was 40 µm. Only the results from the 2 µm tests were used in the material characterization as the 1 µm depth was not sufficient to pierce the oxide layer that had formed on the sample surface. If the oxide layer is not penetrated, the measurement represents the material properties of the oxide layer, not the actual material. The spherical indenter is used in the tests because its shape resembles the shape of a cavitation load [100].

The pits were photographed using an optical microscope with a magnification up to 100 times. The photographs were used to analyse the surface grain structure of the material and to verify that there are pits in both of the observed surface phases. The photographs could also be used to analyse the material properties, though for this study, this approach was left out. Nanoindenter output data is in the form of load in the function of displacement. The nanoindenter is normally used with a conical tip, so the ready calculated output material properties were not useful when using a spherical tip. For the spherical indenter used in this study, the shape of the load-displacement curve is as in Figure 4.10.

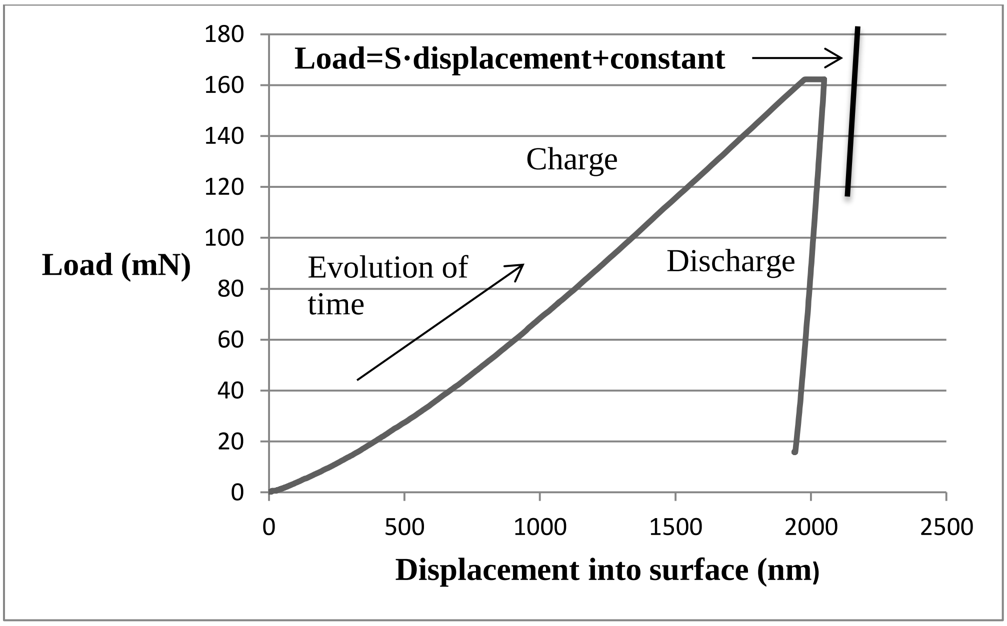

Figure 4.10. *An example of a load-displacement curve obtained from the nanoindentation tests.*

In Figure 4.10, the linear function with the slope *S* is obtained by a linear fit to four or five first points in the discharge section. The discharge section is after the maximum load in the load-displacement curve. The load-displacement data and the curve fit were made using Microsoft Excel in this study. The slope S is defined as: [102]

$$S = \frac{2}{\sqrt{\pi}} E_r \sqrt{A(h)} \tag{4.9}$$

where E_r is the reduced Young's modulus and $A(h)$ is the projected contact area in function of compression height h. The reduced Young's modulus E_r is defined as: [103]

$$\frac{1}{E_r} = \frac{1-\nu^2}{E} + \frac{1-\nu_{ind}^2}{E_{ind}} \tag{4.10}$$

where ν is the material Poisson's ratio, E is the material Young's modulus, ν_{ind} is the indenter Poisson's ratio and E_{ind} is the indenter Young's modulus. In the sample used in this study, two different surface phases with different Young's moduli were observed.

The actual indenter contact area is not exactly the area that a perfect sphere assumption would propose. The indenter deforms during loading and the sphericity is never perfect for a physical object. The test material surface experiences piling up or sinking in, so that the contact area is either bigger than or smaller than the contact area that is calculated without taking this effect into account. The actual contact area may be calculated by modelling the indenter tip and the indenting load and by using a finite element solver. In this study, this method was not applied.

The approximate Young's moduli were calculated with the spherical assumption. With the assumption, the Young's modulus is calculated by combining equations 4.9 and 4.10:

$$E = (1-\nu^2)\left(\frac{2}{\sqrt{\pi}}\frac{\sqrt{A(h)}}{S} - \frac{1-\nu_{ind}^2}{E_{ind}}\right)^{-1} \tag{4.11}$$

The projected contact area in function of height with the perfectly spherical indenter is:

$$A(h) = \pi(2rh - h^2) \tag{4.12}$$

where r is the sphere radius. Equation 4.12 was calculated from sphere geometry.

The reduced Young's moduli from the two separate phases may be compared by dividing S_1 by S_2:

$$\frac{S_1}{S_2} = \frac{\frac{2}{\sqrt{\pi}} E_{r1} \sqrt{A(h)_1}}{\frac{2}{\sqrt{\pi}} E_{r2} \sqrt{A(h)_2}} \approx \frac{E_{r1}}{E_{r2}} \tag{4.13}$$

The contact area is not exactly the same for the indents between the different surface phases of the material. It is though assumed as constant as the Young's moduli for the different phases are expected to be relatively close to each other. Combining equation 4.5 with equation 4.2, the relation between the reduced Young's moduli is:

$$\frac{E_{R1}}{E_{R2}} = \frac{\left(\frac{A}{E_1}+B\right)^{-1}}{\left(\frac{A}{E_2}+B\right)^{-1}} = \frac{\left(\frac{A}{E_2}+B\right)}{\left(\frac{A}{E_1}+B\right)} \tag{4.14}$$

where

$$A = 1 - \nu^2 \tag{4.15}$$

and

$$B = \frac{1-\nu_{ind}^2}{E_{ind}} \tag{4.16}$$

$$\frac{E_{R1}}{E_{R2}}\frac{A}{E_1} + \frac{E_{R1}}{E_{R2}}B = \frac{A}{E_2} + B \tag{4.17}$$

$$\frac{1}{E_1} = \left(\frac{E_{R1}}{E_{R2}}\right)^{-1}\left(\frac{1}{E_2} + \frac{B}{A}\left(1 - \frac{E_{R1}}{E_{R2}}\right)\right) \tag{4.18}$$

and

$$E_1 = \left(\frac{E_{R1}}{E_{R2}}\right)\left(\frac{1}{E_2} + \frac{B}{A}\left(1 - \frac{E_{R1}}{E_{R2}}\right)\right)^{-1} = \left(\frac{E_{R1}}{E_{R2}}\right)\left(\frac{1}{E_2} + \frac{\frac{1-\nu_{ind}^2}{E_{ind}}}{1-\nu^2}\left(1 - \frac{E_{R1}}{E_{R2}}\right)\right)^{-1} \tag{4.19}$$

Equation 4.19 gives the Young's modulus E_1 in the function of E_2, if the ratio between slopes S_1 and S_2 is known. Parameters A and B are used only to reduce the amount of parameters during calculation.

The indentation curve and the shapes of the indents may be used to calculate the Ludwik equation type stress relationship presented in equation 2.21. This was, however, not done for this study as it requires finite element calculation, which was beyond the scope of this thesis. The nanoindentation tests were conducted to identify the surface phases of the sample material and to address the situation of having surface phases with different mechanical properties.

4.6.4 Split Hopkinson pressure bar tests

The Split Hopkinson pressure bar test is a method to conduct compression or traction testing with a high strain rate. A Split Hopkinson pressure bar (SHPB) test may have strain rates in the order of 10^3 1/s. Strain rate has an effect on the material stress-strain behaviour, as described in Chapters 2.1.5 and 2.3.2.

The SPHB testing device consists of two long and symmetric bars, structures to hold these bars aligned, a propulsion device with a strike bar, a momentum trap and strain gauges. The sample is placed between the long bars and the bars have strain gauges installed on them. The propulsion device may use for example compressed gas to create a high velocity to the strike bar that hits the first long bar called the incident bar. The incident bar hits the sample and the sample hits the second bar called the transmitter bar. The transmitter bar hits the momentum trap. In Figure 4.11, the schematics of a typical SHPB test device are presented. [104]

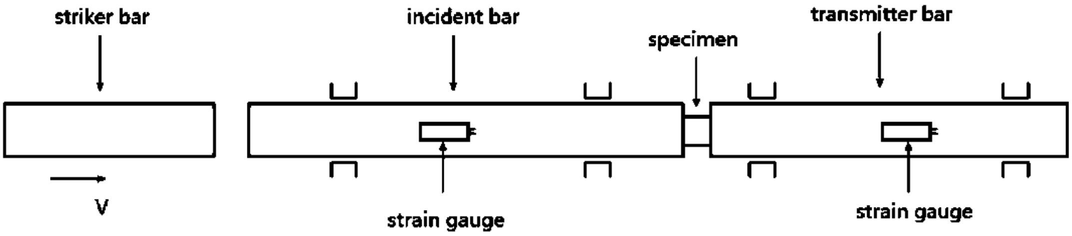

Figure 4.11. *Schematics of a typical SHPB test device. [105]*

The strain gauges measure the incident wave, transmitted wave and reflected wave. These waves are elastic waves traveling through the solid bars. These waves may be used to calculate the stress-strain behaviour of the sample material. In this thesis, the calculation will not be studied in detail as it is not the main focus. Also, the SHPB tests were made by another researcher than the author of this thesis, so the results were used as given. [104]

The SHPB tests in this study were carried out in Tampere University of Technology. They were made with three samples identical to the samples used in the compression tests and with a maximum strain rate of about 2200 1/s. The true stress-true strain curve of a SHPB test is quite similar in shape than that of the compression tests. The curves are presented in Chapter 5.2.4.

Young’s modulus is not extractable from the stress-strain curves as the strain rate is not constant in the sections that would be the section to extract the Young’s modulus in conventional compression or in traction testing. Yield stress is possible to extract from the SHPB data. A linear fit may be applied for the plastic part and for the elastic part of the true stress-true strain curve. The stress value in the intersection of these two linear equations may be considered as the yield stress of the material.

4.7 Alternative cavitation erosion testing setups

Cavitation erosion may be tested in various ways, depending on the problem and test equipment. Hydrofoils or other structures are tested in different types of flow tunnels, but the basic cavitation erosion testing is often done with two standardized methods, the

ASTM G32 vibratory cavitation apparatus and the ASTM G134 cavitating jet apparatus. Different versions of non-standardized rotational disk devices have also been widely used. The PREVERO cavitation tunnel and similar test setups are also used to study cavitation erosion. These four testing methods prove similar results, but with significantly varying magnitude. This proves that cavitation erosion is highly dependent on the flow conditions and the test setups. This chapter presents three optional testing setups.

4.7.1 ASTM G32 vibratory cavitation apparatus

The ASTM G32 vibratory cavitation apparatus is a relatively small and simple way to do cavitation erosion testing. The apparatus consists of a vibrating horn that is submerged into a tank filled with liquid, with the test sample either fixed in the horn or placed below it. The method was first standardized in 1998 and similar methods were already used before. Zhou and Hammitt [74] conducted experiments with a similar test setup before the standardization of the method, obtaining results to predict erosion rates from different material characteristics. Okada et al. [106] found a linear relation between impact loads and cavitation damage both with a vibratory device and a Venturi test channel.

The horn vibrates with a relatively high frequency, leading to large accelerations in the fluid adjacent to the horn. With a sufficiently high frequency, local pressure drops below the saturated vapour pressure or more accurately, the critical value of pressure for cavitation inception. The local pressure rises after the low pressure phase, leading to bubbles collapsing near the sample material.

The ASTM G32 device vibrates with a 20 kHz frequency and with a horn tip motion A' of 25 μm. The vibration provokes a sinusoidal type pressure field: [39]

$$p = \rho_l c_l \dot{x} = -2\pi f \rho_l c_l A' sin(2\pi f t) \tag{4.20}$$

where c_l is the speed of sound in liquid, ρ_l is the liquid density and f is the vibrating frequency. For water, the amplitude factor $2\pi f \rho_l c_l A'$ is 47 MPa, so at ambient pressure the critical values for cavitation inception are easily reached. The cavitation forms as a cloud cavity around the vibrating horn. The cloud cavitation in an ASTM G32 device is relatively aggressive and the typical time intervals between mass measurements are from seconds to several minutes. [18; 39]

Hattori and Nakao [11] observed the removed particles to study erosion mechanisms in an ASTM G32 device. Hattori et al. [12], Hattori and Ishikura [14] and Hattori and Kitagawa [13] conducted experiments with the device and created a database of different materials, comparing their erosion characteristics. Karabenciov et al. [107] compared erosion results for stainless steels with variable chromium and nickel content, though apparently they used an ASTM G32 device with a frequency and amplitude varying from the standard values. The ASTM G32 device was used by Kendrick et al. [108] to compare erosion rates of polymers, elastomers, composite materials and metals for the use of the naval industry.

Karimi and Avellan [18] studied the differences between cavitation test methods. They tested a two-dimensional Francis turbine model, a water tunnel, a vortex cavitation generator (rotational disk device) and a vibratory cavitation apparatus. According to their study, the vortex cavitation generator and the other hydrodynamic cavitation test setups provide results that represent real flow situations better than a vibratory cavitation apparatus. The erosion in a vibratory cavitation apparatus develops uniformly over the surface, having a long incubation time in terms of collapse cycles. [18; 109]

4.7.2 ASTM G134 cavitating liquid jet

The ASTM G134 cavitating liquid jet consists of a pressurized test loop with a nozzle providing high speed liquid flow in a test section that is also filled with liquid. The high speed jet is directed towards the material sample to be tested. Cavitation is created in the shear layer between the high speed liquid flow and the stationary liquid. The bubbles collapse near the sample material, leading to cavitation erosion. The cavitating flow has structures with a relatively high vorticity, leading also to vortex cavitation, which is discussed in Chapter 2.4.3. [39]

The pressure levels in the ASTM G134 setup can be controlled and tests may be done with constant or variable cavitation number. The upstream jet pressure may be as high as 300 MPa and the downstream pressure may be ambient pressure or something between 0.1 MPa and 2 MPa [39].

The nozzle geometry may be varied from the standard geometry to produce different kinds of erosion patterns or aggressiveness. ASTM G134 provides generally relatively high erosion rates, if the jet speed is high. The maximum erosion rates for ASTM G134 are generally higher than those for ASTM G32 or the PREVERO cavitation tunnel. The type of cavitation is more similar to real applications than that of the ASTM G32. [17; 39]

Soyama and Futakawa [16] created a model to predict the incubation time with post-incubation measurements in an ASTM G134 cavitating jet. Hattori et al. [110] developed a way to predict the incubation time with piezoelectric pressure sensor measurements, reaching a moderate accuracy.

4.7.3 Rotational disk apparatus and vortex cavity generator

The rotational disk apparatus and the vortex cavity generator both work with the principle of creation vorticity in a flow with sufficiently low cavitation number. Cavitation inception occurs in the vortex core and cavitation closure occurs a short distance downstream. The sample materials are placed in the closure region. Vortex cavitation is more similar to actual hydraulic machinery cavitation than that of the ASTM G32 [18].

The rotational disk apparatus was used by Osterman et al. [111] to evaluate mass loss period with incubation period pit counting. Liquid flows through holes in the rotating disk to a test chamber that is also filled with liquid. Test samples are placed on the disk downstream from the holes. Cavitation aggressiveness is dependent on the cavitation number controlled by upstream and downstream pressures, the rotation speed of the disk, the placement of the samples and the liquid quality.

The vortex cavity generator was used by Karimi et al. [109] to study the erosion rates of duplex stainless steels. It consists of a liquid flow loop in which there is a test section with rapid changes of flow direction, upstream and downstream tanks, a pump and a rotating valve. The test section has a tangential inlet and an axial outlet, creating vorticity and causing cavitation damage to the material sample. The rotating valve is used to create expansion waves that increase the cavitation aggressiveness. According to Karimi and Avellan, the type of cavitation is of the similar type as that in a Francis turbine. [18]

5. RESULTS

5.1 Introduction to results

There are three different types of results in this study; the mass or volume loss evolution results, the acoustic emission results coupled with the erosion stages and the results from material characterization tests. In Table 5.1, the time intervals and details in the testing schedule are presented.

Table 5.1. *Measurement time intervals and method details.*

Test number	Cumulative time after test (minutes)	Measurement method details
1	0	Initial profiles and pencil lead break tests for acoustic emission. Acoustic emission sensor: Brüel & Kjær 8313
2	2	Surface profiles in 4 directions and in 5 separate lines. Surface profile for a 2 mm times 6 mm area in direction 3. Acoustic emission sensor: Brüel & Kjær 8313
3	4	Change of acoustic emission preamplifier batteries. Change of acoustic emission sensor to Fujicera 1045S. Surface profile for a 2 mm times 6 mm area in direction 3.
4	6	Testing of the acoustic emission data acquisition system with a different voltage range (0-10V). Surface profile for a 2 mm times 6 mm area in direction 3.
5	8	Acoustic emission testing with a supplementary resistance of 18 kΩ between the preamplifier power source and the data acquisition unit. Surface profile for a 2 mm times 6 mm area in direction 3.
6	10	Supplementary resistance of 67 kΩ.
7	12	Supplementary resistance of 118 kΩ.
8	16	Supplementary resistance of 550 kΩ. Testing a different preamplifier with adjustable sensitivity and amplification. Surface profile for a 2 mm times 6 mm area in direction 3.
9	46	Measurements continued with the same test setup as in measurement 8. Surface profile for a 2 mm times 6 mm area in direction 3.
10	286	No changes in setup.
11	540	No changes in setup.
12	780	
13	1020	
14	1260	
15	1500	

Material characterization tests were made with samples not subjected to cavitation erosion. Surface profile measurements were made to the sample material between the cavitation erosion testing periods and the acoustic emission measurements were made both between and during the testing periods.

The measurements up to measurement number 8 were made with a short period of cavitation erosion to learn the appropriate setup for the acoustic emission measurements. The results from the first measurements were not used in the analysis as the amplitude of the signal exceeded the limits of the data acquisition setup. This problem was addressed by changing the sensor type from resonance to broadband type sensor and by adding a supplementary resistance before the data acquisition unit signal input.

In the other test between the cumulative time of 12 and 16 minutes, a different preamplifier was tested, but it was not used later because it had a limit of 100 kHz in maximum signal frequency. This was found to be too low to detect some features in the signal. When the final acoustic emission test setup was found, the measurement procedure was the following: A four hour period of cavitation erosion in the PREVERO cavitation tunnel, in which one minute of acoustic emission signal is recorded three times: once in the beginning, once in the middle and once in the end of the period.

The erosion testing was stopped when the cumulative erosion time was 1500 minutes. After the 1500 minutes of erosion, sample profile with the orientation number 3 had a maximum erosion depth of over 1000 μm, which is over the profilometer measurement limit. If the erosion depth is too large, the surface profile also begins to affect the flow field in the test section. The goal of the test is to have a uniform cavitation field over the erosion time, so changes in the flow field make the results non-comparable.

5.2 Material characterization

For the material characterization, four types of tests were conducted; an elemental analysis, macroscopic compression tests, nanoindentation tests and split Hopkinson pressure bar tests. The elemental analysis was done by an external company and the split Hopkinson pressure bar tests were conducted in a laboratory in Tampere University of Technology, both not by the author of this thesis. The compression tests and nanoindentation tests were done in the SiMAP laboratories. Material strain rate dependency is calculated in the SHPB section in Chapter 5.2.4.

5.2.1 Elemental analysis

An elemental analysis of the sample material was made. In this study, the results are used only for material classification. Figure 5.1 presents the elemental composition of the steel sample.

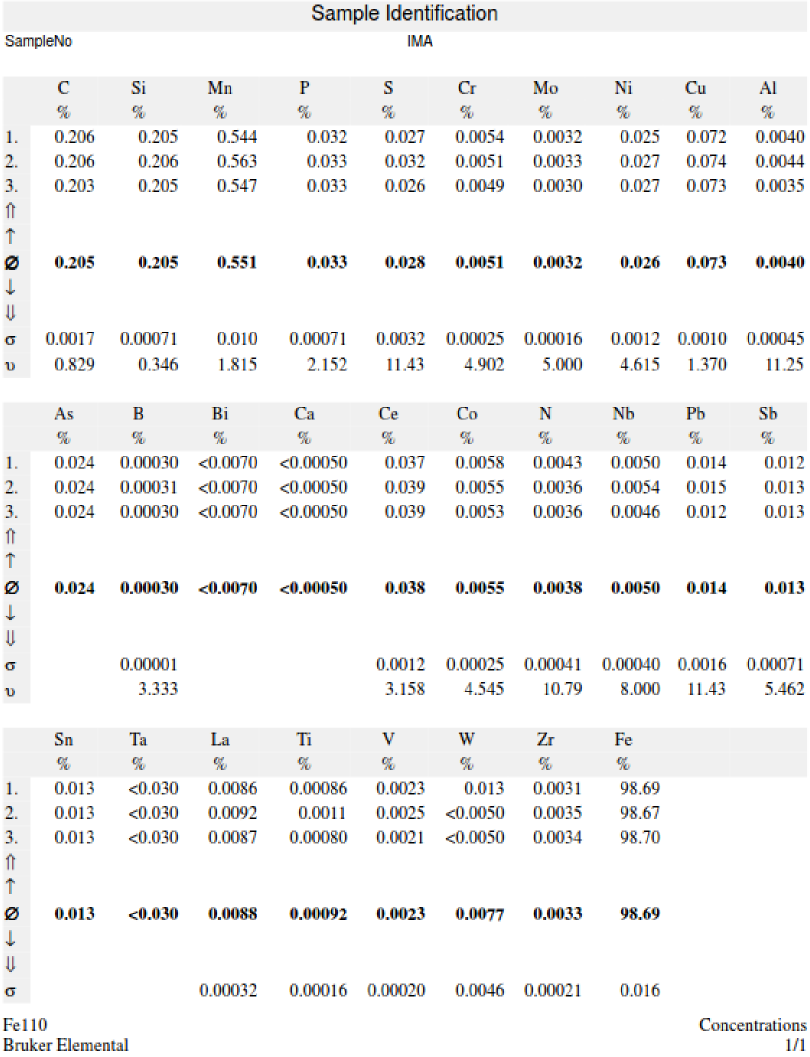

Sample Identification

SampleNo IMA

	C	Si	Mn	P	S	Cr	Mo	Ni	Cu	Al
	%	%	%	%	%	%	%	%	%	%
1.	0.206	0.205	0.544	0.032	0.027	0.0054	0.0032	0.025	0.072	0.0040
2.	0.206	0.206	0.563	0.033	0.032	0.0051	0.0033	0.027	0.074	0.0044
3.	0.203	0.205	0.547	0.033	0.026	0.0049	0.0030	0.027	0.073	0.0035
⇑										
↑										
Ø	**0.205**	**0.205**	**0.551**	**0.033**	**0.028**	**0.0051**	**0.0032**	**0.026**	**0.073**	**0.0040**
↓										
⇓										
σ	0.0017	0.00071	0.010	0.00071	0.0032	0.00025	0.00016	0.0012	0.0010	0.00045
υ	0.829	0.346	1.815	2.152	11.43	4.902	5.000	4.615	1.370	11.25

	As	B	Bi	Ca	Ce	Co	N	Nb	Pb	Sb
	%	%	%	%	%	%	%	%	%	%
1.	0.024	0.00030	<0.0070	<0.00050	0.037	0.0058	0.0043	0.0050	0.014	0.012
2.	0.024	0.00031	<0.0070	<0.00050	0.039	0.0055	0.0036	0.0054	0.015	0.013
3.	0.024	0.00030	<0.0070	<0.00050	0.039	0.0053	0.0036	0.0046	0.012	0.013
⇑										
↑										
Ø	**0.024**	**0.00030**	**<0.0070**	**<0.00050**	**0.038**	**0.0055**	**0.0038**	**0.0050**	**0.014**	**0.013**
↓										
⇓										
σ		0.00001			0.0012	0.00025	0.00041	0.00040	0.0016	0.00071
υ		3.333			3.158	4.545	10.79	8.000	11.43	5.462

	Sn	Ta	La	Ti	V	W	Zr	Fe
	%	%	%	%	%	%	%	%
1.	0.013	<0.030	0.0086	0.00086	0.0023	0.013	0.0031	98.69
2.	0.013	<0.030	0.0092	0.0011	0.0025	<0.0050	0.0035	98.67
3.	0.013	<0.030	0.0087	0.00080	0.0021	<0.0050	0.0034	98.70
⇑								
↑								
Ø	**0.013**	**<0.030**	**0.0088**	**0.00092**	**0.0023**	**0.0077**	**0.0033**	**98.69**
↓								
⇓								
σ			0.00032	0.00016	0.00020	0.0046	0.00021	0.016

Fe110
Bruker Elemental

Concentrations
1/1

Figure 5.1. *Runner blade steel elemental analysis.*

In Figure 5.1, the carbon content of the sample is found to be 0.205 % and the iron content to be 98.69 %. It is a typical composition for low alloy non-stainless steels. No further information about the manufacturing of the sample was found. This was due to the age of the turbine runner blade. No documentation from the manufacturing regarding the material composition or other material properties was found.

5.2.2 Compression tests

The compression tests were done with three different strain rates: $7.795 \cdot 10^{-4}$ 1/s, 10^{-2} 1/s and 1 1/s. The different strain rates were used to define the strain rate dependency of the sample in the full range of strain rates. True stress in function of true strain curves for different strain rates are presented in Figures 5.2, 5.3 and 5.4.

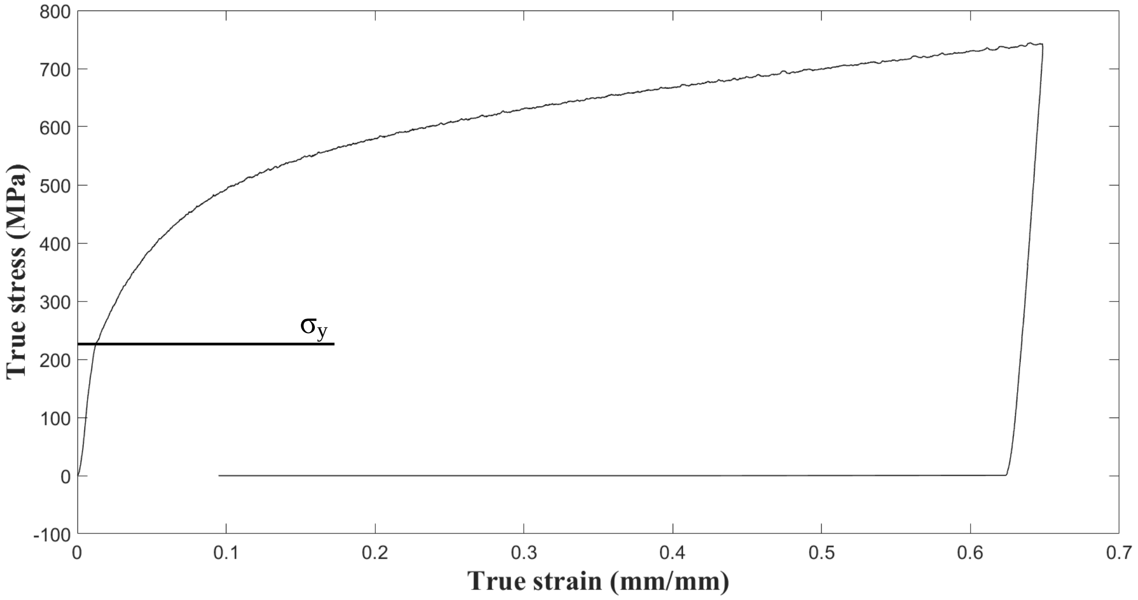

Figure 5.2. *True stress in function of true strain for the strain rate of 7.795·10^{-4} 1/s.*

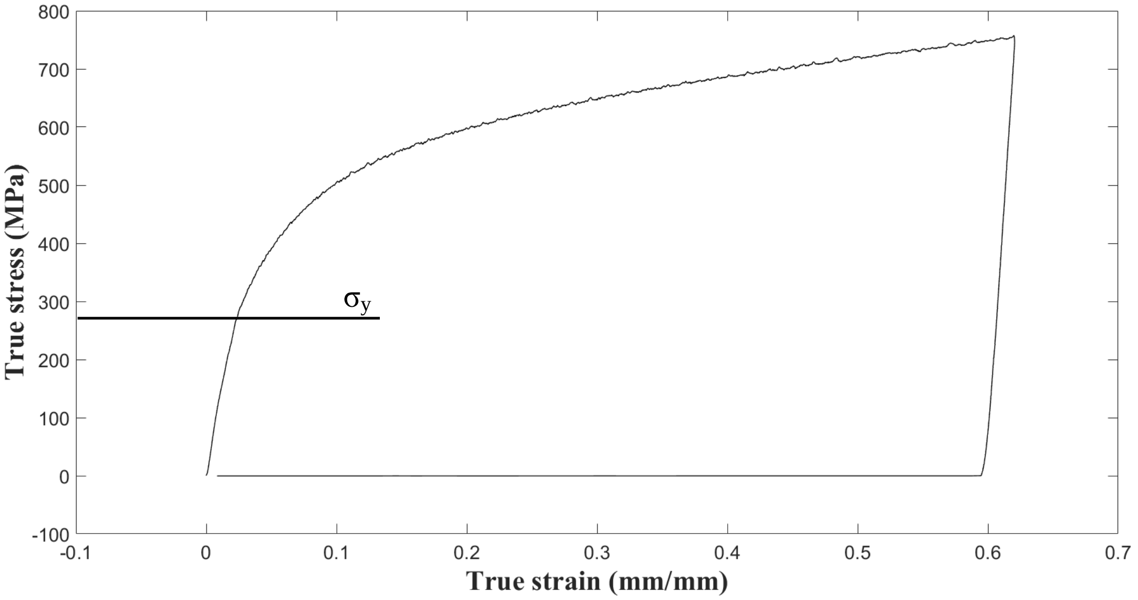

Figure 5.3. *True stress in function of true strain for the strain rate of 1·10^{-2} 1/s.*

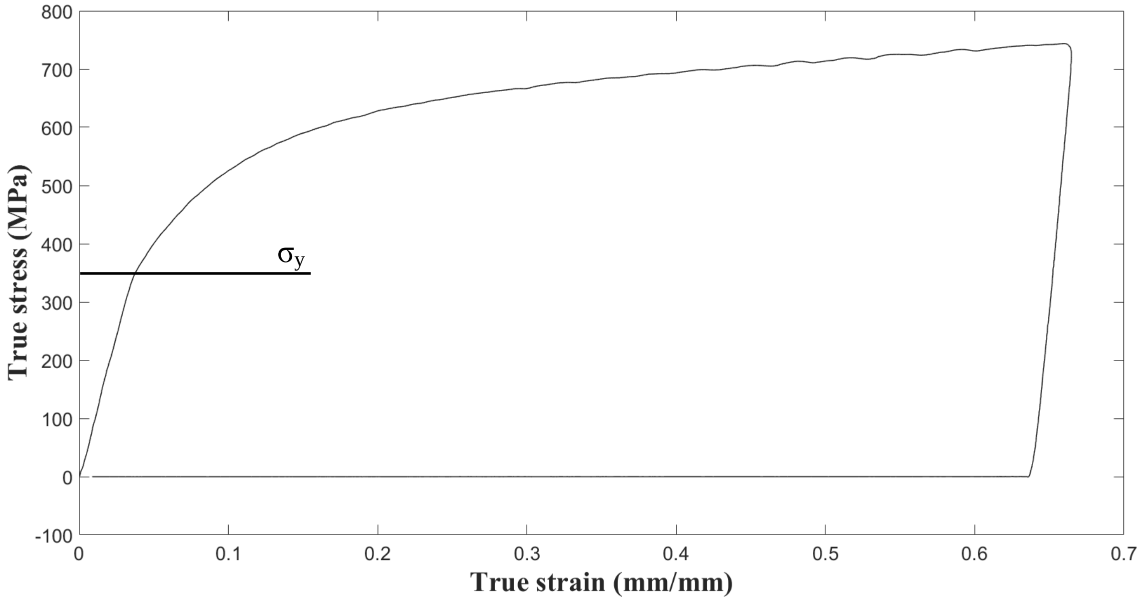

Figure 5.4. *True stress in function of true strain for the strain rate of 1 1/s.*

The values for the Young's moduli were extracted from the slope of the discharge part of the curve. The yield stress was obtained from the point where the linear part ends in the charge part of the curve. Table 5.2 shows the Young's moduli E and the yield stresses σ_Y for the different strain rates.

Table 5.2. *Material characteristics derived from the compression tests.*

Strain rate (1/s)	Young's modulus (GPa)	Yield stress (MPa)
7.795·10^{-4}	36	228
1·10^{-2}	35	288
1	30	346

The results obtained from the stress-strain curves cannot be considered accurate, as they were extracted visually. The yield stress corresponds to values of standard steels for the lowest strain rate. The literature value is 110 to 240 MPa for low alloy steels [112]. The obtained Young's moduli are much smaller than literature values. The typical value for the Young's modulus is around 200 GPa for standard low alloy steels [112].

The results from the compression tests cannot be considered very reliable. They can be used to categorize the material and to create the Johnson-Cook equation for the strain rate sensitivity, presented in Chapter 2.3.2. For further analysis, new compression tests should be done.

5.2.3 Nanoindentation tests

For the nanoindentation tests, the data from the 2 µm indents were used to obtain the Young’s moduli of the two separate surface phases. The microscope pictures taken from the superpolished sample surface show that there are two detectable phases. Figure 5.5 is a microscope picture taken from the sample with a 20 times magnification.

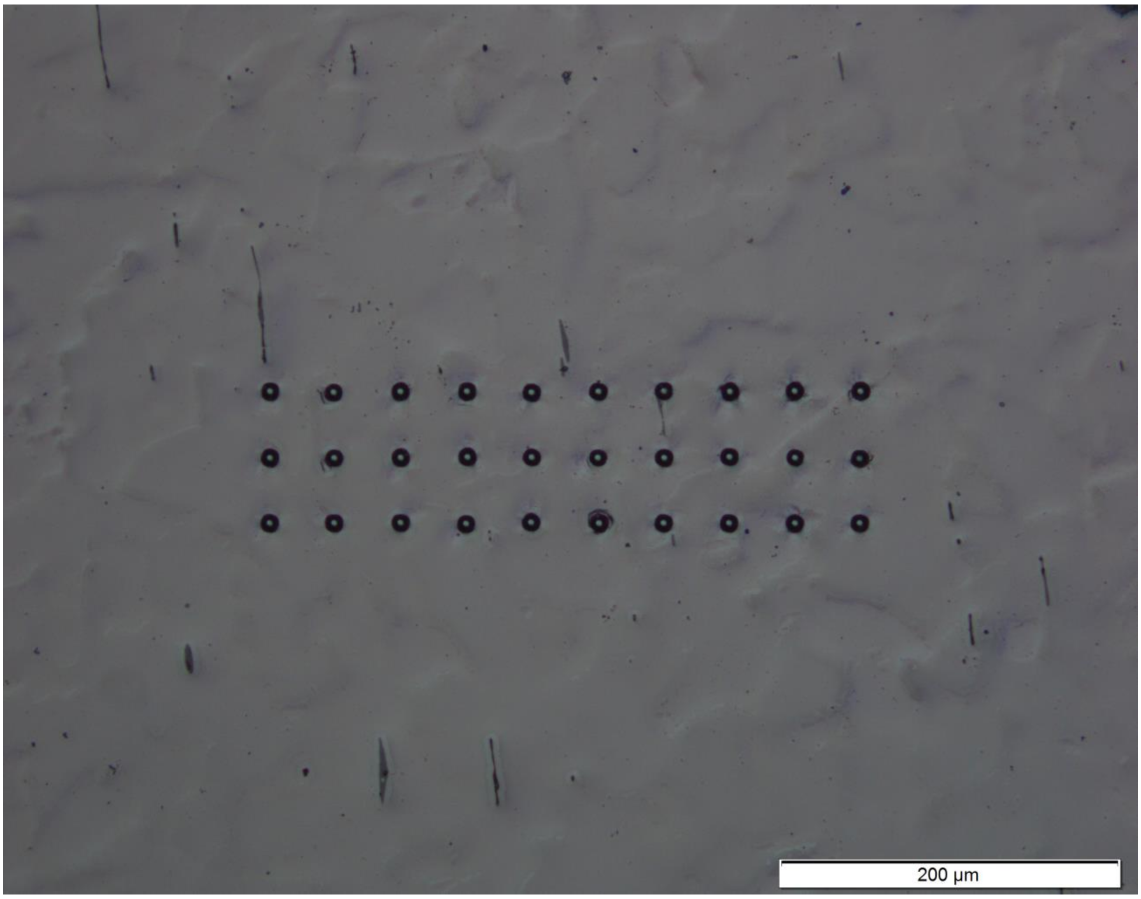

Figure 5.5. *Nanoindentation sample magnified 20 times. Indent depth 2µm, distance between indents 40 µm.*

From Figure 5.5, the two different surface phases may be identified. As some of the indents fall in the boundary of two phases, they are left out in the data handling. As explained in Chapter 4.6.1, the parameter *S* from the discharge slope is obtained. The parameter S had two distinctively different values. Values not falling into this category were excluded from the results. An average of the value *S* for these two datasets was calculated and the two different Young’s moduli were calculated with the perfectly spherical indenter approximation.

In Figures 5.6 and 5.7, two curves from the nanoindentation tests with different values for the slope *S* are presented.

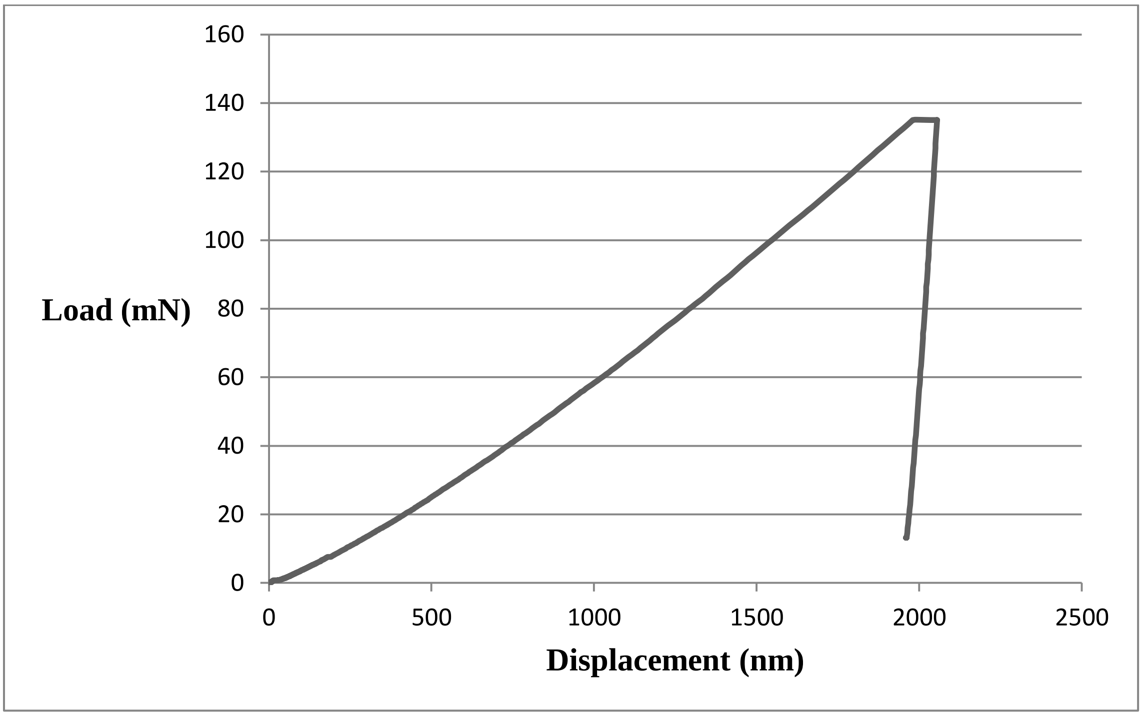

Figure 5.6. *Load in function of displacement for indent number 20. S=1.003 mN/nm.*

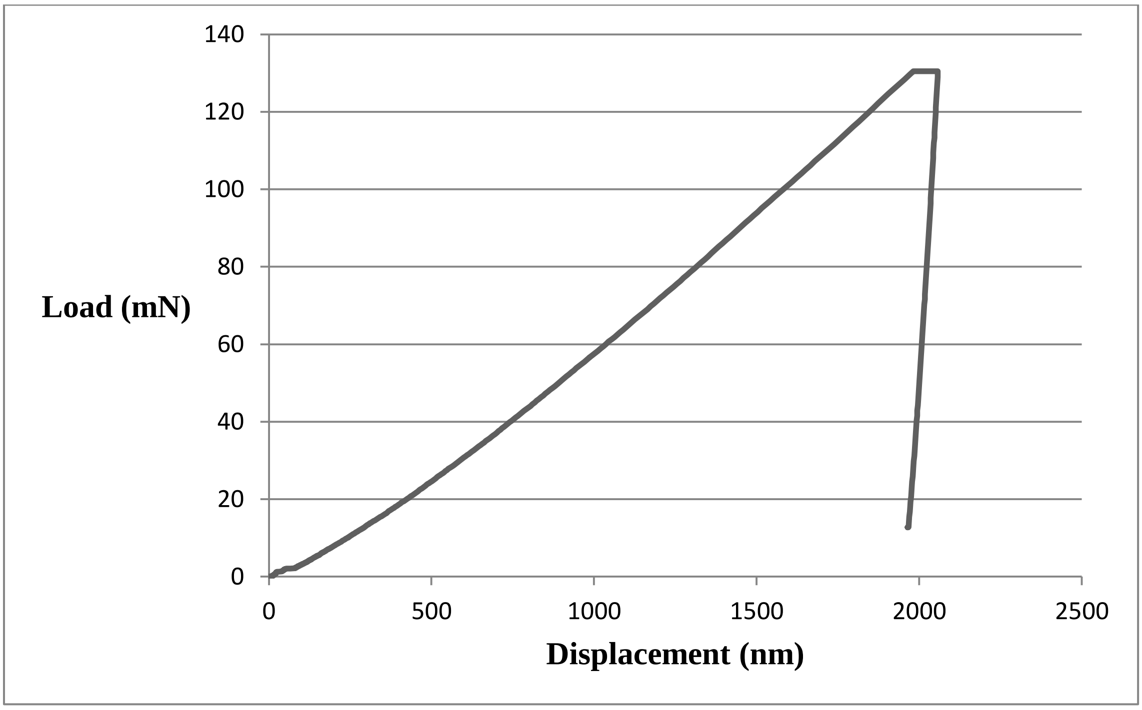

Figure 5.7. *Load in function of displacement for indent number 26. S=1.848 mN/nm.*

The total amount of indents was 30 for the 2 μm indent depth, as described in Chapter 4.6.3. In total, four indents were excluded from the results as they did not fall into the category of their *S*-values being either close to 1 or close to 2. These four indents were assumed to be in the grain boundaries. Observations of the microscope photographs were in agreement with this assumption.

The averaged values for parameter *S* and Young’s modulus *E* for phases number 1 and 2 are presented in Table 5.3.

Table 5.3. *Averaged values of parameter S and Young’s modulus E.*

S_1 (N/m)	S_2 (N/m)	E_1 (GPa)	E_2 (GPa)
1000315	1956200	85	179

To verify the results, E_1 was also calculated with the equation obtained from the relation between S_1 and S_2. The Young’s modulus for the steel was chosen as 0.30, which is a typical value for low alloy steels [112]. With correct values inserted into equation 4.11, the result for E_1 is exactly the same as the results from the approximated value.

This is the expected result, as for both of the methods the contact area is assumed to be constant between measurements in different phases. Equation 4.11 may be used if the Young’s modulus for the other phase is known and the indenter deformation is known to be negligible.

The nanoindentation tests cannot be used directly to define the yield stresses of the two phases. The Young’s moduli from the nanoindentation tests seem to be plausible. The interpretation of the results is that in terms of the Young’s modulus, one phase is about 2.1 times harder than the other phase. Out of 30 indents, 20 indents were in the softer phase, 6 indents were in the harder phase and 4 indents were not categorizable.

5.2.4 Split Hopkinson pressure bar tests

Three samples were used for the split Hopkinson pressure bar tests. The tests were not made by the author, so the results were used as given. The strain rates in the SHPB tests are not constant. One example of the true stress in function of true strain and with the true strain rate in function of true strain is presented in Figures 5.8 and 5.9. The curves for all three tests are similar, but the yield stresses were extracted from each curve separately.

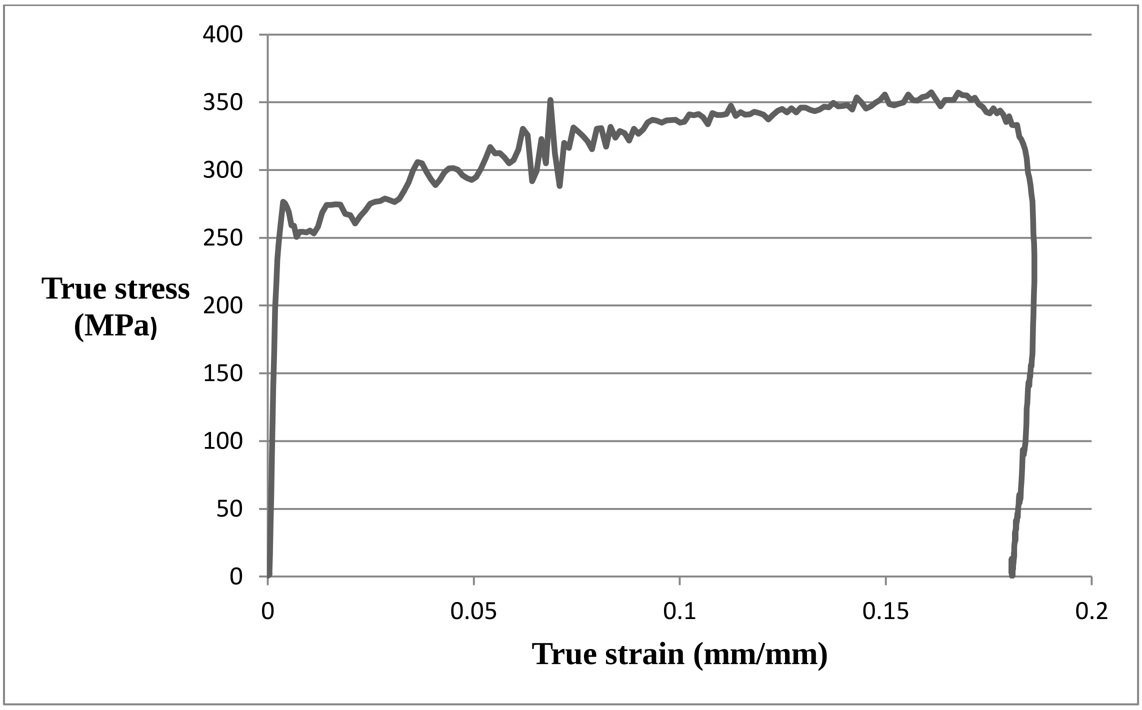

Figure 5.8. *True stress in function of true strain in a SHPB test.*

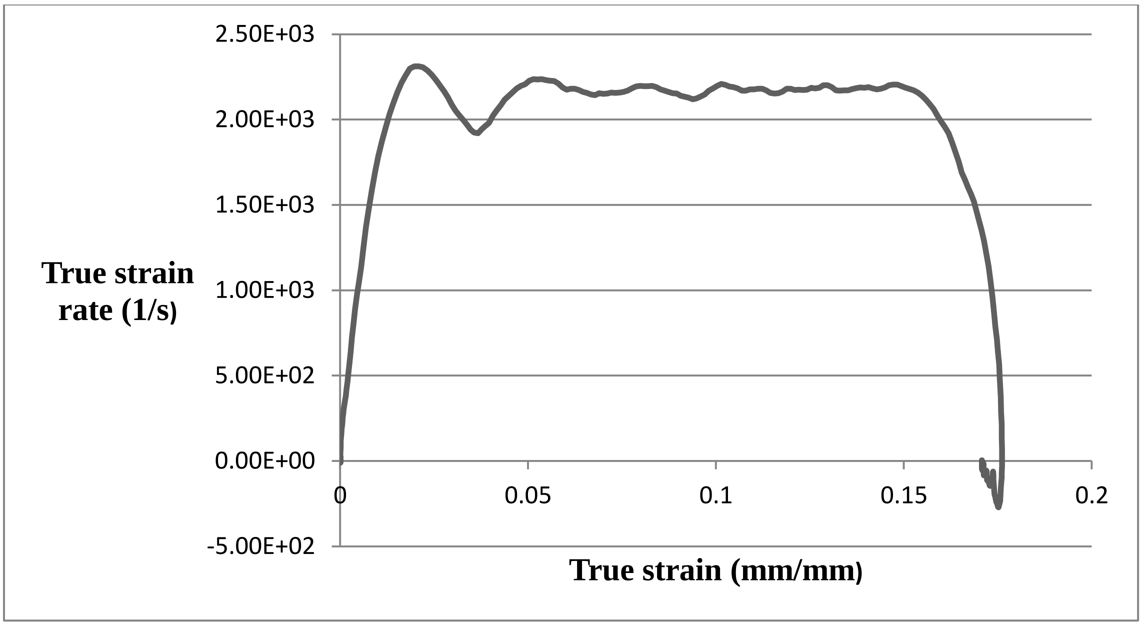

Figure 5.9. *True strain rate in function of true strain in a SHPB test.*

From Figure 5.9, it may be observed that in the beginning and in the end of the SHPB tests, the strain rate is not constant. In the middle part of the test, the strain rate is nearly constant. The strain rate is not constant in the charge and discharge parts of the curve in Figure 5.8. For this reason, the Young’s modulus cannot be extracted from the data. Yield stress is obtained by fitting linear equations in the plastic part of the curve and the elastic part of the curve and by finding the stress value in the intersection of these curves, as described in Chapter 4.6.4. The values for the yield stress are presented in

Table 5.4. Also the average strain rates in the plastic region of the curves are presented in Table 5.4. The plastic region is the part where the strain rate is almost constant.

Table 5.4. *Yield stress values and average strain rate from the SHPB tests.*

Test number	Yield stress (MPA)	Average strain rate (1/s)
1	267	2210
2	260	2070
3	259	2250

The yield stress values between t tests do not differ significantly. The value obtained from the SHPB tests should be larger than that of the conventional compression tests. Only the compression test with the strain rate of $7.795 \cdot 10^{-4}$ 1/s falls into this category. The results from the compression tests are not reliable enough to make conclusions about the material. Using the one compression test result falling into the right category and the three SHPB results, the strain rate dependency of the material may be estimated, though the result is not reliable.

For the Johnson-Cook equation, a reference strain rate needs to be chosen. For this study, the value was chosen to be 1 1/s. The reference yield stress $\sigma_{y,ref}$ was found to be 245.99 MPa with the curve fitting method described in Chapter 2.3.2. The curve fit corresponding to equation 2.24 is presented in Figure 5.10.

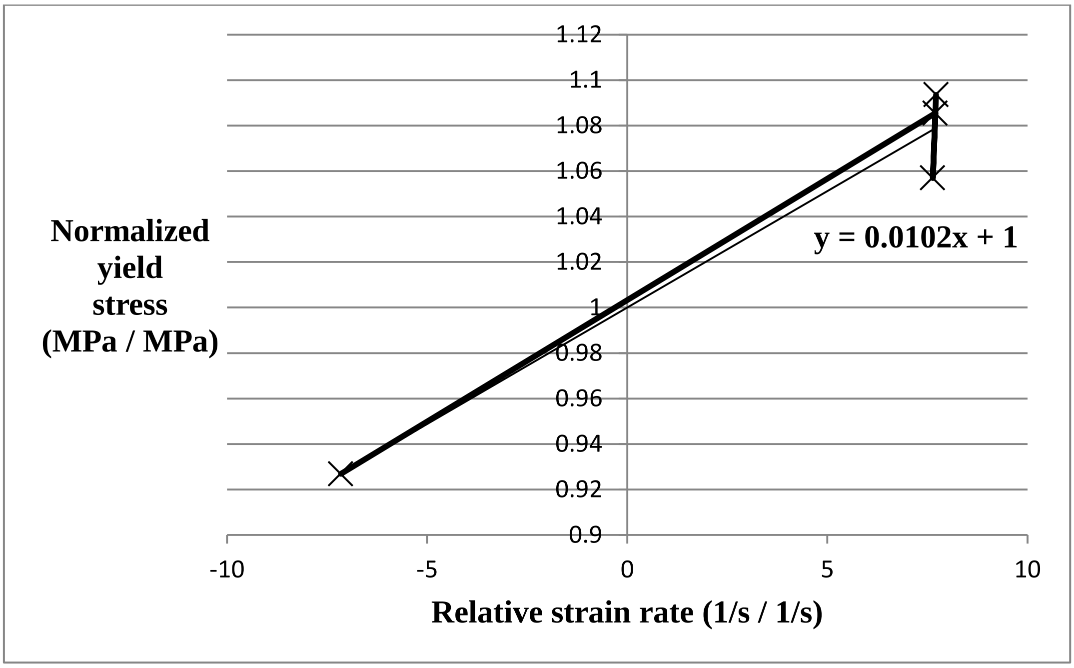

Figure 5.10. *Normalized yield stress in the function of relative strain rate.*

In Figure 5.10, parameter C is the slope of the linear fit. The value of C is 0.0102. With the value of C, the Johnson-Cook equation may be written as:

$$\sigma = (244.99\,MPa + K'{\varepsilon_p}^{n})(1 + 0.0102 ln \frac{\dot{\varepsilon}}{1\frac{1}{s}}) \tag{5.1}$$

Without information of the parameters K' and n, the result may only be used to predict yield stresses with varying strain rates. By extrapolating equation 5.1 to the strain rate of $1 \cdot 10^6$ 1/s, which is the order of magnitude of strain rates in cavitation impacts, the yield stress $\sigma_{y,1e6}$ was found to be 279.5 MPa. The extrapolation is not well justified, as the thermal effects become important in strain rates of this order of magnitude [105]. The result provides an estimate of the increase in yield stress due to the high strain rate of the cavitation impact material deformation.

5.3 Erosion evolution

The erosion evolution results are separated into four chapters: sample photographs and their analysis, erosion evolution in time, volume loss and volume loss rate curves and maximum erosion depth and maximum erosion depth rate curves. In Chapter 6, the results for the sample in this study are compared to those of previously tested materials.

5.3.1 Sample photographs

The zone of maximum erosion remains at the same approximate radial distance for all sample orientations. In the PREVERO cavitation tunnel the cavitation erosion is axisymmetric and if there are any problems with for example nozzle wear, the axisymmetricity is lost. This means that if the cavitation was not axisymmetric, the radial location of the erosion zone would differ significantly. The possible cause for the large difference in erosion behaviour lies in the material composition and work hardening history.

Photographs from the sample were taken between each period of cavitation erosion. In the first photograph, in which the initial sample is, the sample surface has a mirror polishing. As the sample was made from steel, the sample surface was oxidized when it came into contact with water in the test setup. In all the photographs after the initial one, the cavitation erosion zone is visible as it is the only one without rust. In Figures 5.11 and 5.12, the sample photographs are in the order corresponding to erosion evolution in time.

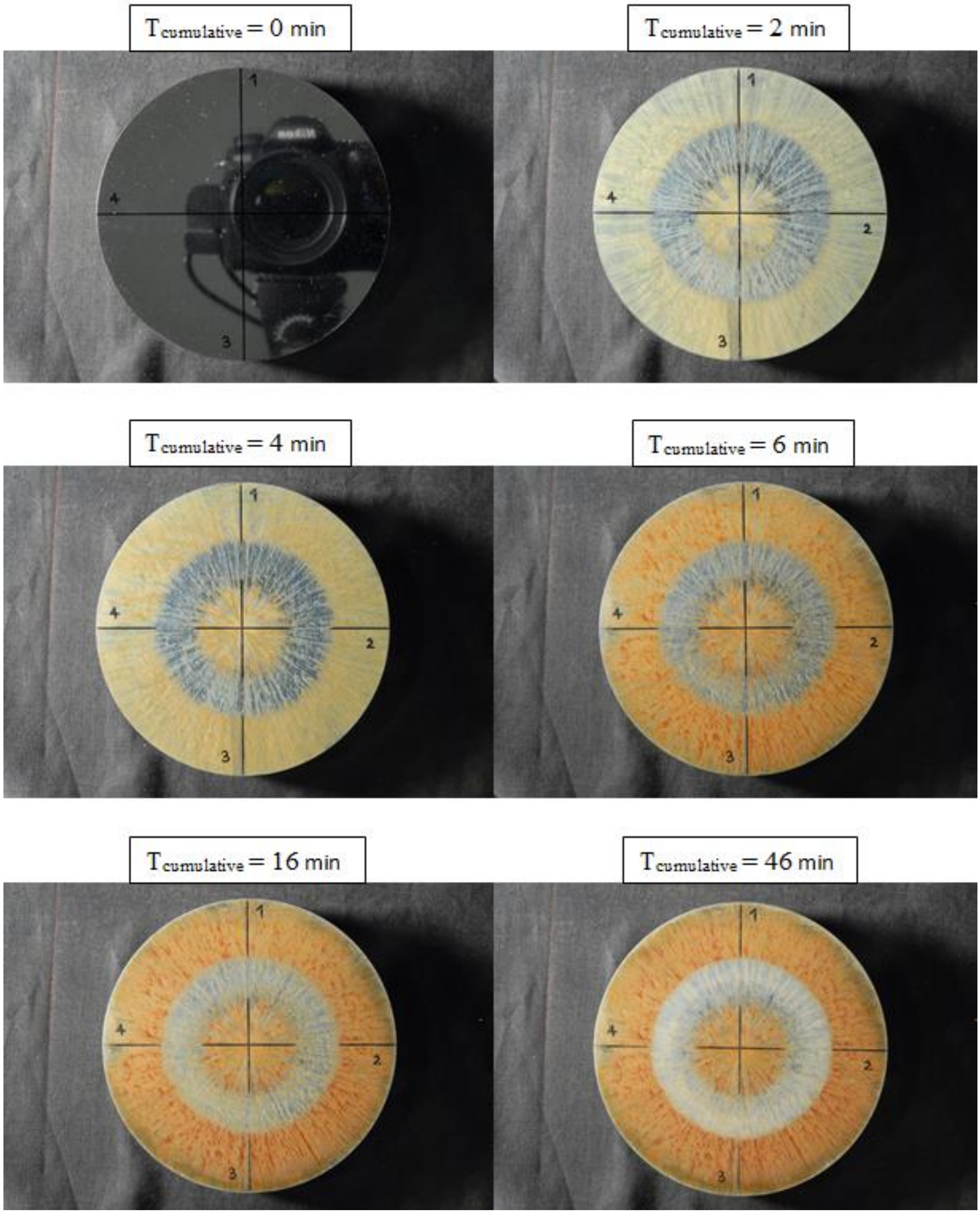

$T_{cumulative} = 0$ min

$T_{cumulative} = 2$ min

$T_{cumulative} = 4$ min

$T_{cumulative} = 6$ min

$T_{cumulative} = 16$ min

$T_{cumulative} = 46$ min

Figure 5.11. *Sample photographs from the incubation period. Increasing amount of pits is observed when the cumulative cavitation erosion time increases.*

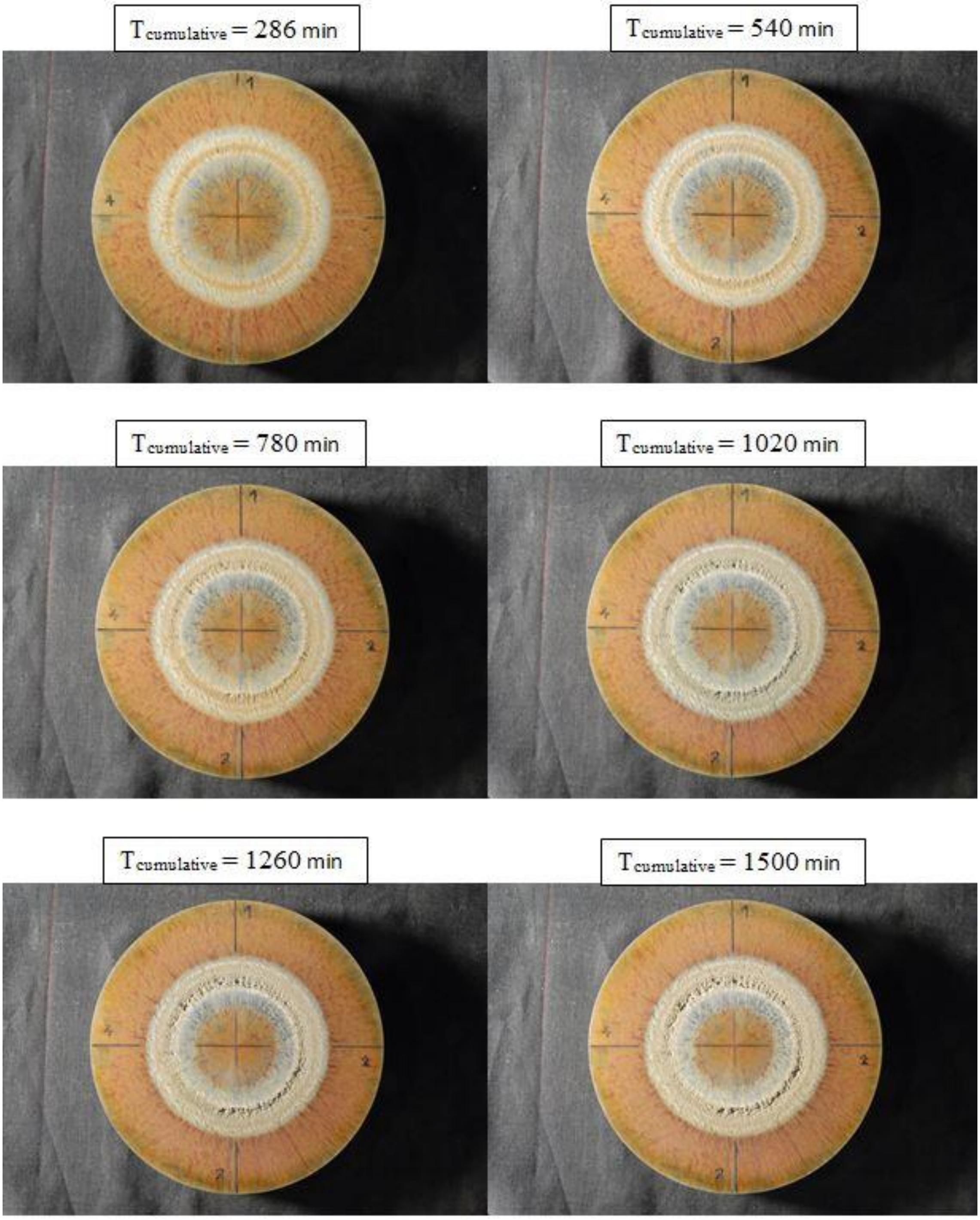

Figure 5.12. *Sample photographs from the advanced erosion periods. In the three photographs with the largest cumulative erosion time, significant material loss is observed.*

Erosion measurement results show approximately the same erosion evolution in all sample orientations in the incubation period. As the erosion advances to the stages with significant mass loss, erosion rates in different sample orientations begin to differ. In sample orientations 1 and 3, large amount of material was removed between cumulative erosion times of 540 minutes and 1020 minutes. At cumulative erosion time of 1500 minutes, the approximate maximum depths of the erosion zones were 400 µm for orientations 2 and 4, 700 µm for orientation 1 and over 1000 µm for orientation 3.

5.3.2 Surface profiles

The sample surface profiles and their evolution in time in all four orientations are traced in Figures 5.13, 5.14, 5.15 and 5.16. All time steps were not included in the profile evolution as too many time steps lead to incomprehensible figures. The four sample orientations are visible in the sample photographs in Chapter 5.3.1.

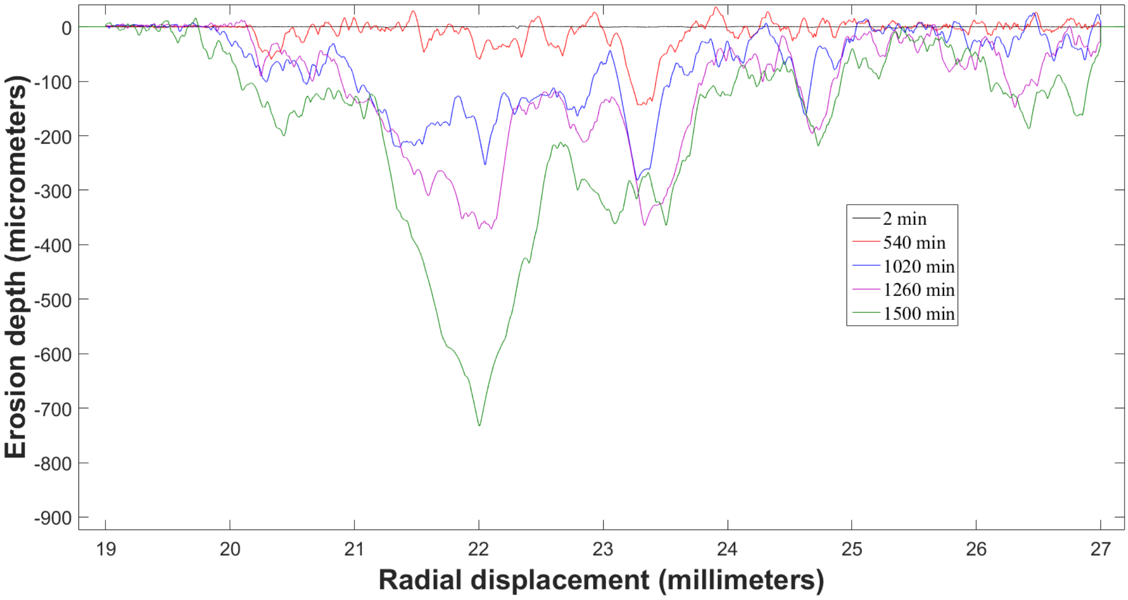

Figure 5.13. *Profile evolution along measurement line 1.*

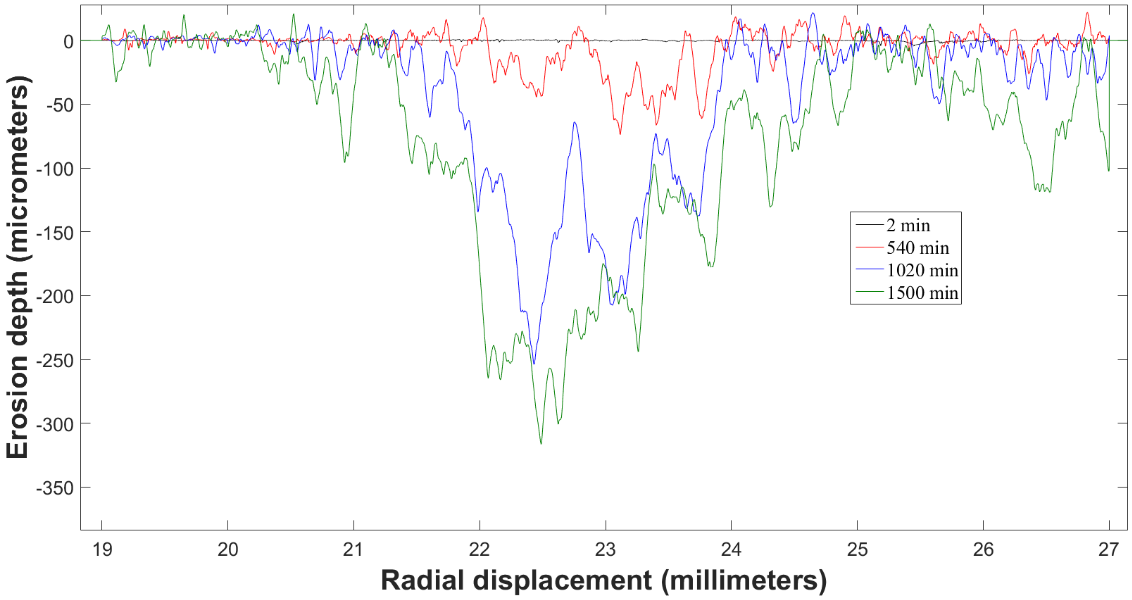

Figure 5.14. *Profile evolution along measurement line 2.*

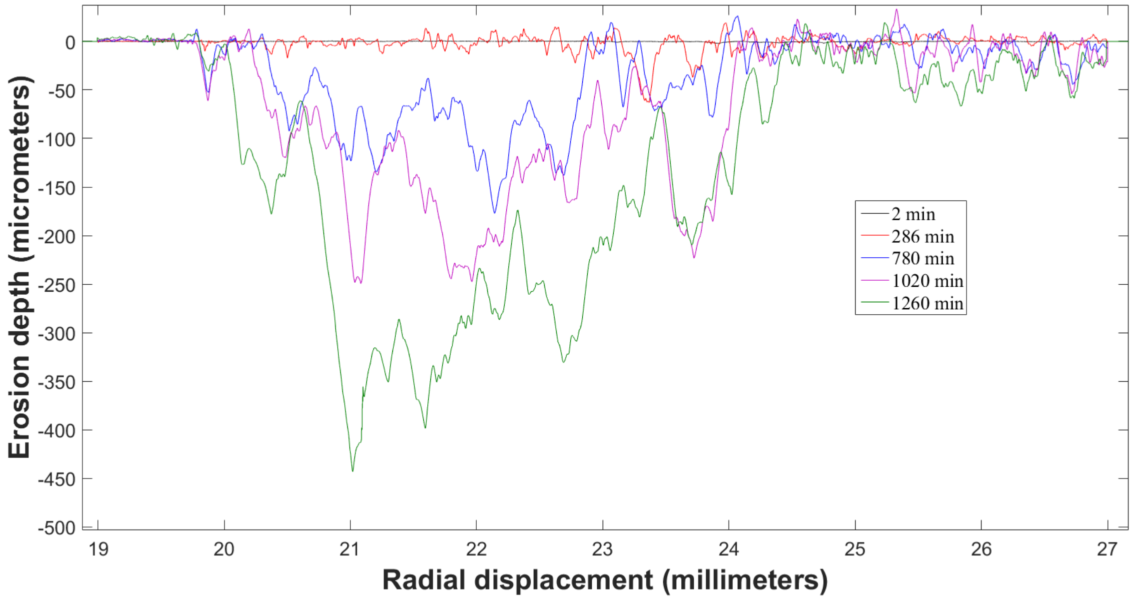

Figure 5.15. *Profile evolution along measurement line 3.*

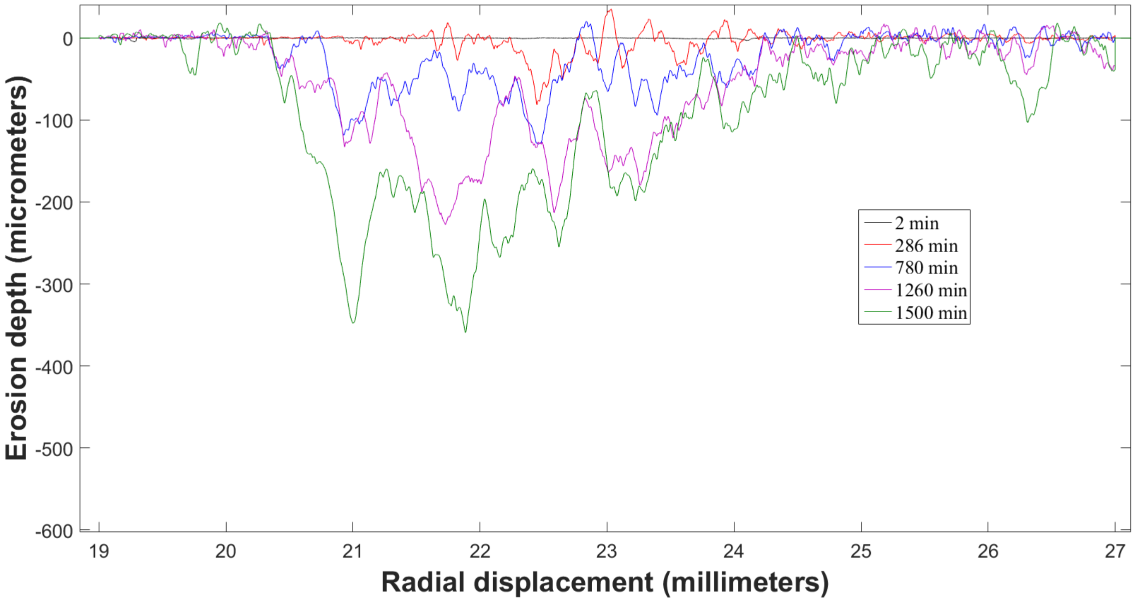

Figure 5.16. *Profile evolution along measurement line 4.*

Figures 5.13 and 5.15 present measurement lines number 1 and 3. Along these lines, the erosion was much faster than along lines number 2 and 4 in Figures 5.14 and 5.16. Line number 3 was measured only up to the cumulative time of 1260 minutes, as after 1500 minutes the maximum erosion depth was over 1000 µm, which is beyond the profilometer measurement limit.

The maximum erosion depths are closer to the beginning of the erosion zones for lines 1 and 3 than those for lines 2 and 4. All the profiles show a certain maximum erosion zone. The radial displacement values differ, but the difference is not significant enough for conclusions that the cavitation field would not have been axisymmetric.

All the profiles contain local minimums and maximums. This is probably because of the materials non-homogenous structure. Cavitation attacks the weaker material phase first, so this type of behaviour is expected. As the weaker phase is removed, at some point large chunks of material is removed in a short duration as the stronger phase is more removed than broken down.

5.3.3 Volume loss

The volume loss and volume loss rate curves are calculated from the surface profiles with the equations presented in Chapter 2.5.3. The volume losses and volume loss rates were calculated with the program MATLAB R2015b. The volume loss evolution of the sample material is presented in Figure 5.17 and the volume loss rate evolution is presented in Figure 5.18.

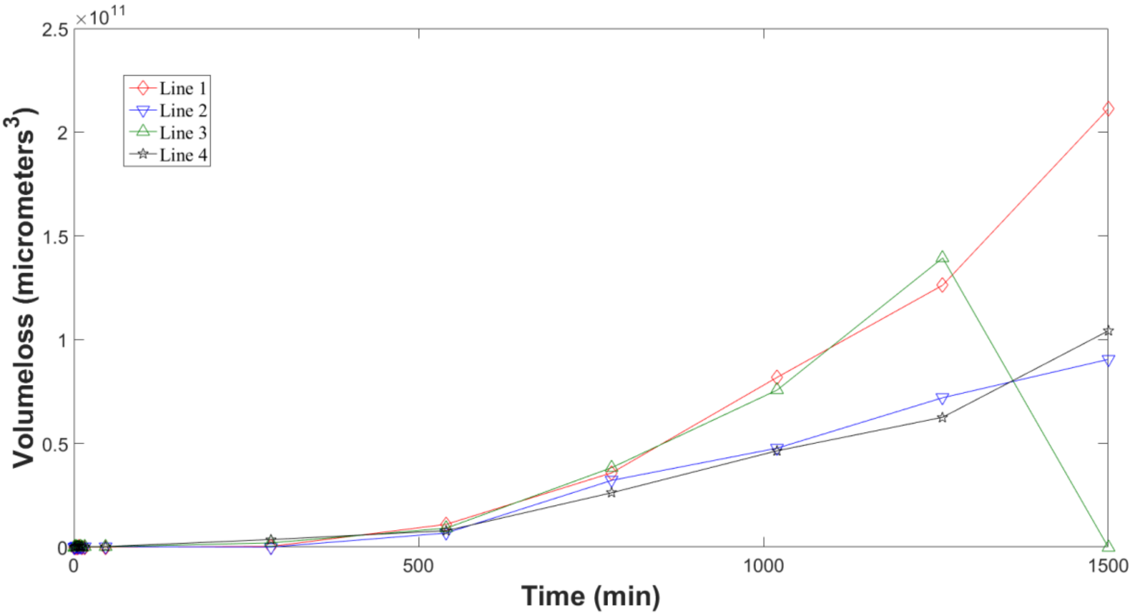

Figure 5.17. *Volume loss in function of time for different measurement lines. Line 3 going to zero value in time of 1500 minutes means that the measurement is out of the range of the profilometer.*

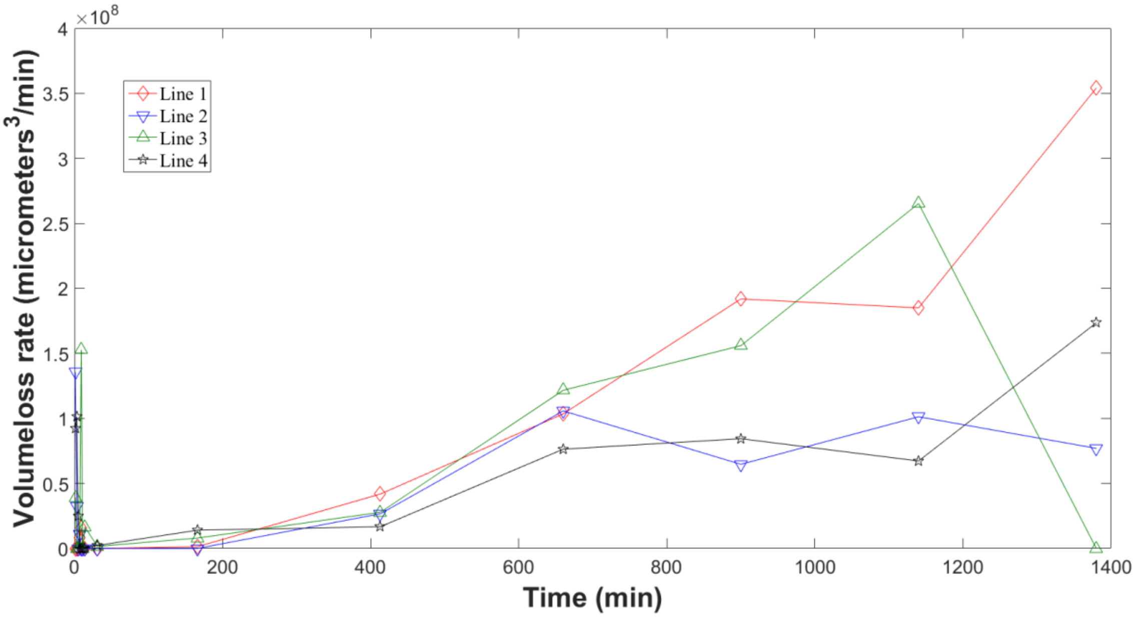

Figure 5.18. *Volume loss rate in function of time for different measurement lines. Line 3 going to zero value in time of 1380 minutes means that the measurement is out of the range of the profilometer.*

In the beginning of the volume loss rate curves in Figure 5.18, spikes of high volume loss rates are visible. These spikes are due to the profilometer inaccuracy and to the short time between the measurements in the beginning of the tests. These spikes should not be taken into account in any analysis of the data. The short measurement time with small errors in the profilometer data leads to the exaggeration of the surface deformation rate in the beginning. Until 200 minutes of cumulative time, the volume loss rate is effectively zero.

Large variation in the volume loss is observed between the different sample orientations. As already seen from the sample photographs in Chapter 5.3.1, the erosion along lines 2 and 4 is slower than the erosion along lines 1 and 3. This behaviour can also be observed in the volume loss rate curves. There are two possible explanations for the difference, either the cavitation field was not axisymmetric or the material composition was not axisymmetric.

The cavitation field should be axisymmetric and the non-axisymmetricity should be possible to identify from the movement of the maximum erosion depth zone. The maximum erosion depth zone differed, but not significantly enough to reliably conclude that there would be disturbances in the axisymmetricity. The problem can be avoided by fixing the sample holder to different orientations between measurements. This was not done in this study because of the potential problems caused in the acoustic emission data analysis.

Material composition was not measured from the sample used in the cavitation erosion tests. The sample material is from an actual used turbine, so the work hardening history of the material may be significant. The work hardening through machining was avoided as well as possible when the sample was cut from the runner blade. The sample surface was also polished to remove hardened surface. The runner blade might have already work hardened non-homogenously before the cutting. Also the grain structure of the material might be heterogeneous through the sample.

For a sample material, average cavitation erosion behaviour can be calculated with a large amount of tests. The average was calculated for the four lines in this study. For improved statistical accuracy, a larger amount of samples could be tested and measured. In Figure 5.19 and 5.20, the average values for the volume loss and volume loss rate in function of cumulative erosion time are presented.

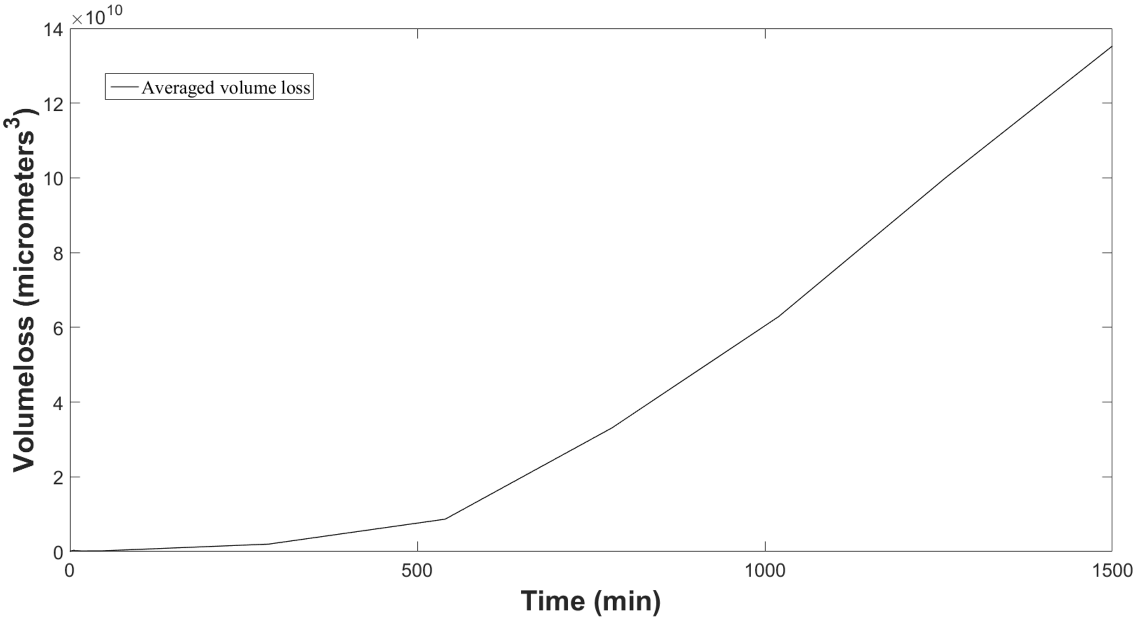

Figure 5.19. *Averaged volume loss in function of cumulative erosion time.*

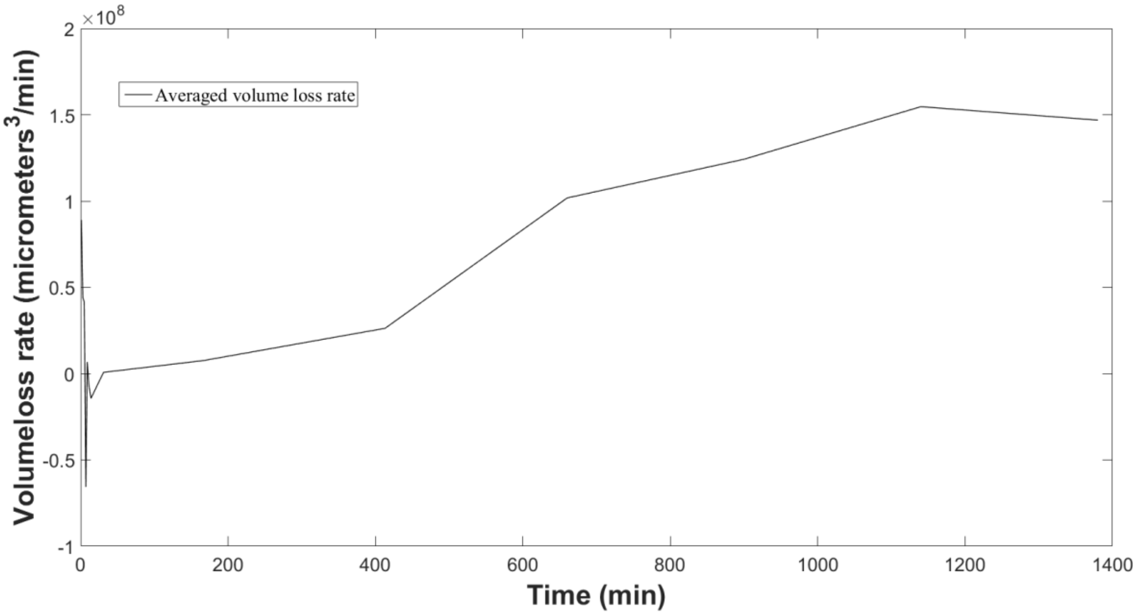

Figure 5.20. *Averaged volume loss rate in function of cumulative erosion time.*

The average volume loss seems to settle in a steady linear slope after 1000 minutes of cumulative erosion time. This corresponds to the almost constant volume loss rate in the end of the volume loss rate curve. The average volume loss rate is calculated from the averaged volume loss data. In Chapter 6.1, the average volume loss and the averaged volume loss rate are compared to equivalent values of other materials studied in the PREVERO cavitation tunnel.

5.3.4 Maximum erosion depth

The maximum erosion depth and maximum erosion curves were calculated from the surface profiles with the equations presented in Chapter 2.5.3. The maximum erosion depths and maximum erosion depth rates were calculated with the program MATLAB R2015b. The maximum erosion depth is the maximum value for a 200 µm length averaged depth along the profile for each values of cumulative erosion time. The maximum erosion depth rate is the speed of the maximum erosion depth evolution in each erosion time interval. The maximum erosion depth evolution is presented in Figure 5.21 and the maximum erosion depth rate evolution is presented in Figure 5.22.

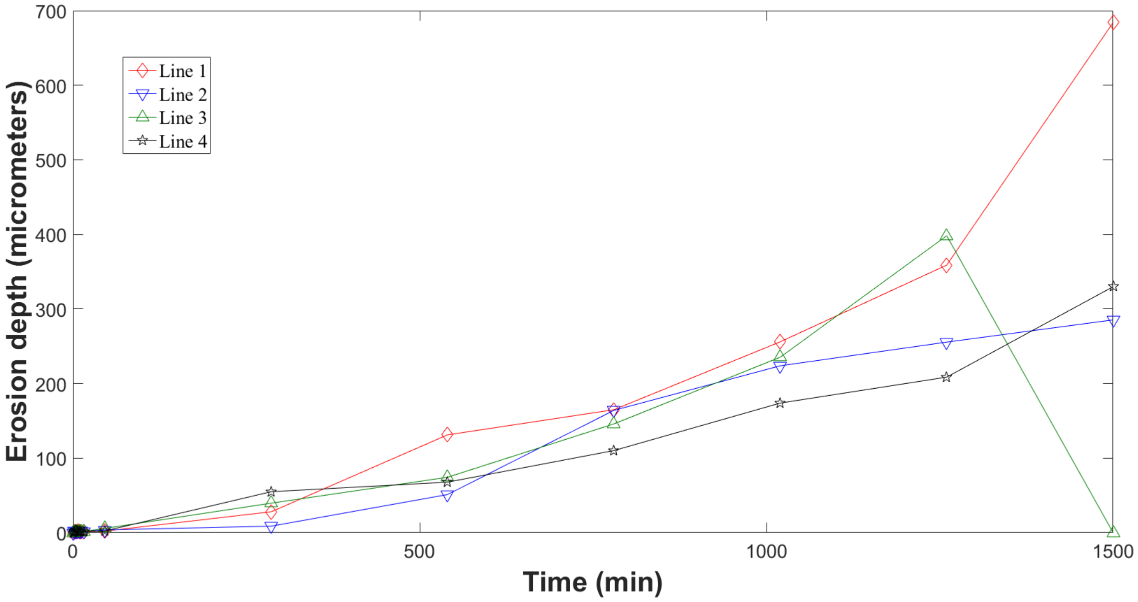

Figure 5.21. *Maximum erosion depth in function of cumulative erosion time for different measurement lines.*

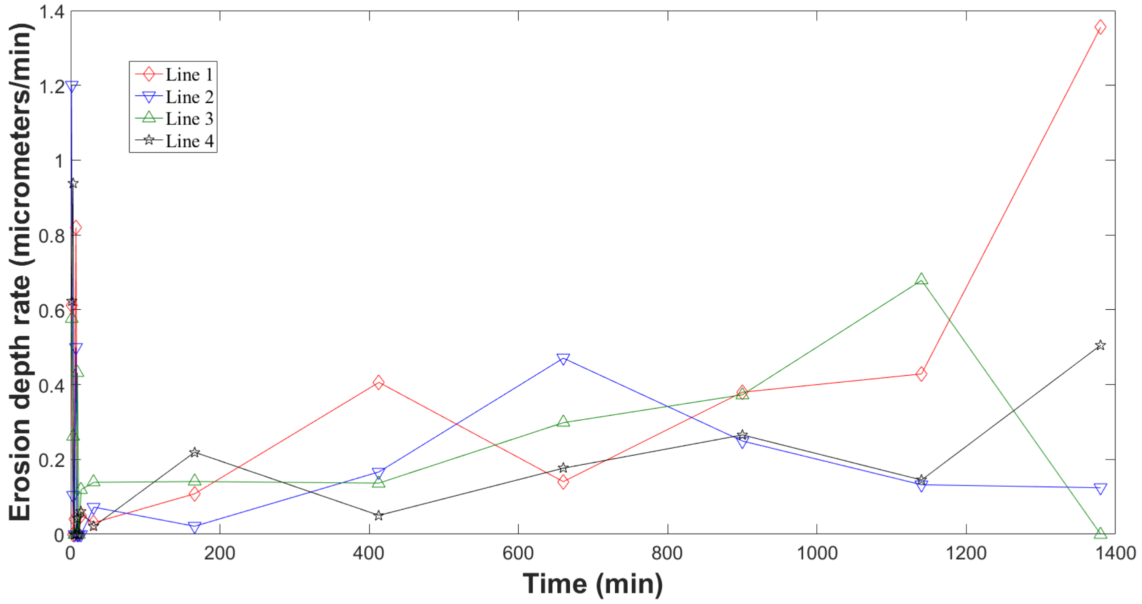

Figure 5.22. *Maximum erosion depth rate in function of cumulative erosion time for different measurement lines.*

The reason to choose an average over a certain distance is that if a single point is chosen, the point may represent a profilometer error, as already described in Chapter 2.5.3. For the maximum erosion depth, the erosion along lines 1 and 3 was faster than along lines 2 and 4. The result is in agreement with the volume loss results and the sample photographs. The erosion depth rate shows similar behaviour as the volume loss rate.

The maximum erosion depth rate shows similar spikes in the beginning of the erosion. This is due to same profilometer errors than the spikes in the volume loss rate. The averaged erosion depth and averaged erosion depth rate in function of cumulative erosion time are presented in Figures 5.24 and 5.25.

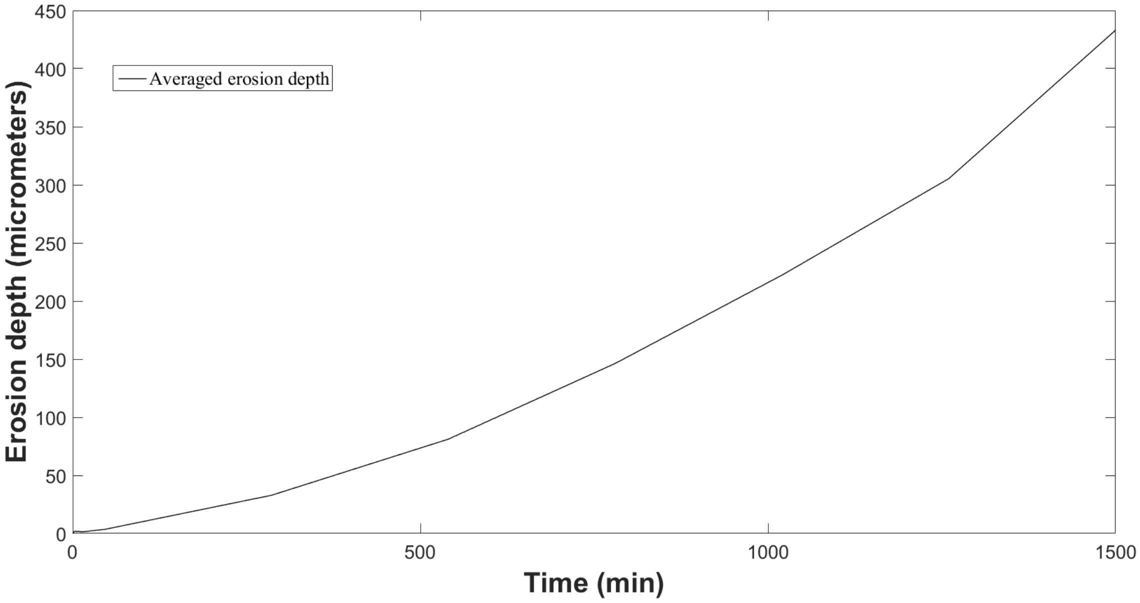

Figure 5.23. *Averaged erosion depth in function of cumulative erosion time.*

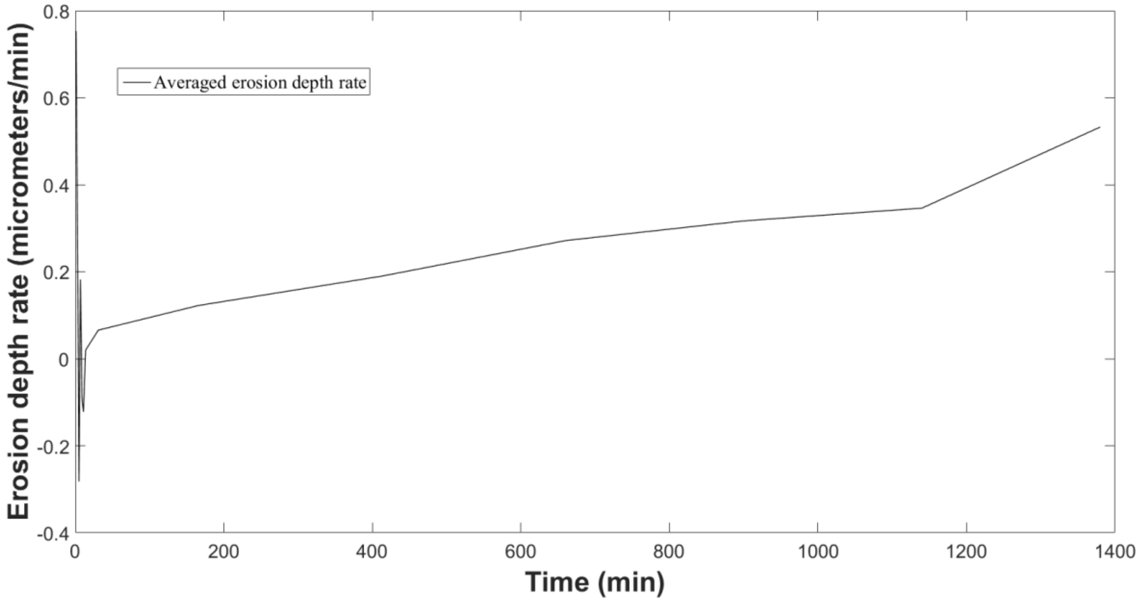

Figure 5.24. *Averaged erosion depth rate in function of cumulative erosion time.*

The averaged erosion depth shows similar linear behaviour after 1000 minutes of cumulative erosion time as the volume loss. An increase in the erosion depth rate shows that the erosion depth evolution accelerates in the last erosion period. The average volume loss settles to a constant value better than the averaged erosion depth. This means that the erosion, in terms of volume loss, is stronger in the zone of maximum erosion than other zones after the cumulative time of 1000 minutes. More analysis of the profile evolution compared to the volume loss and erosion depth data is presented in Chapter 6.1. The averaged values of the erosion depth and erosion depth rate are compared to the equivalent values of other materials studied with the PREVERO cavitation tunnel in Chapters 6.1.1 and 6.1.2.

5.4 Acoustic emission results

Acoustic emission was measured for three types of emission sources. First the pencil lead break signals on the sample with the waveguide installed, second the signal when the cavitation tunnel is operated in non-cavitating region and third the signal when the cavitation tunnel is operated in the cavitating region. The non-cavitating region was not measured for each erosion period.

The non-cavitating region represents lower flow velocities in the test section than those of the cavitating region. This is why the signal from the non-cavitating region may not be interpreted as a signal that is from a liquid flow with cavitation excluded. The signal evolution in the non-cavitating region can however be used as an indicator for the changes in the liquid flow noise reaching the acoustic emission sensor.

The frequency contents from the cavitating and the non-cavitating regions were filtered with a high-pass filter. Filters with different limits were used. The filter excludes all frequencies under the limit frequency from the signal. The non-filtered frequency contents are not presented, as the low frequency signals have high amplitude and they represent unwanted signal noise. The signals have a varying y-axis scale because of the varying signal amplitude.

The signal amplitude is presented in a 10-base logarithmic scale. One non-cavitating region signal and four cavitating region signals are presented in each figure. In Figures 5.25, 5.26 and 5.27, the 5 kHz, 25 kHz and 100 kHz filtered signals from the cavitating region and the non-cavitating region are presented. The non-cavitating region signal is the signal with the lowest overall amplitude and for the cavitating region signals, the overall amplitude decreases with increasing cumulative erosion time. The values in the y-axis correspond to the signal strength.

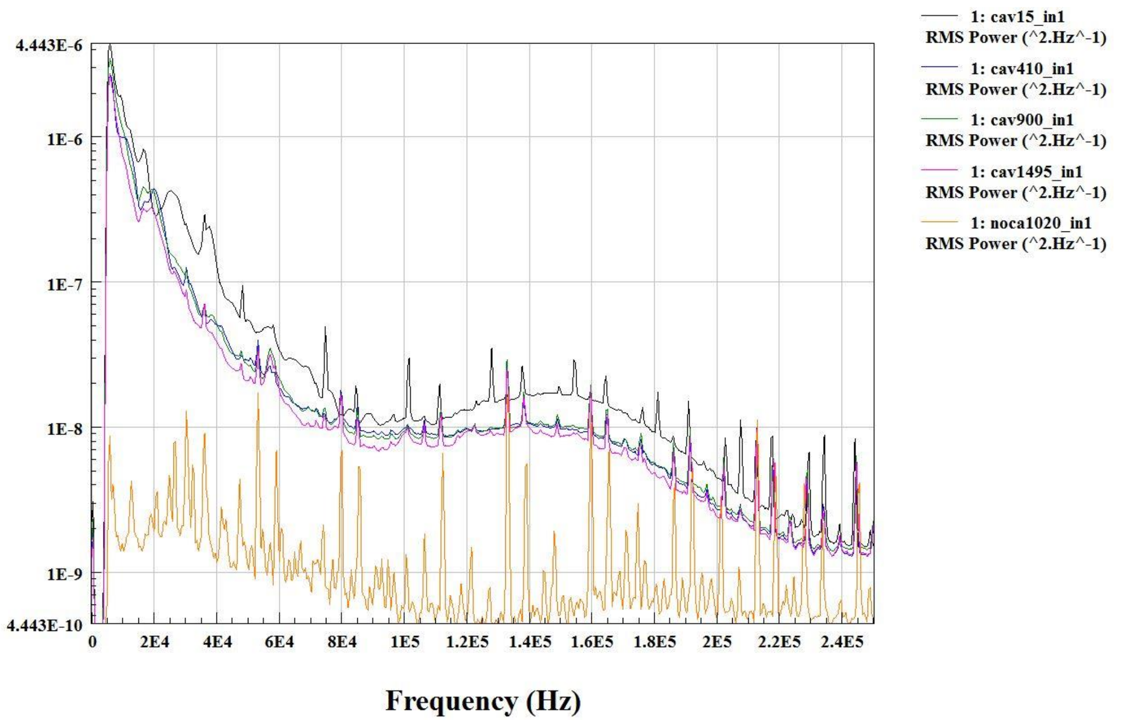

Figure 5.25. *5 kHz high-pass filtered AE signals y-axis is presented in 10-base logarithmic scale.*

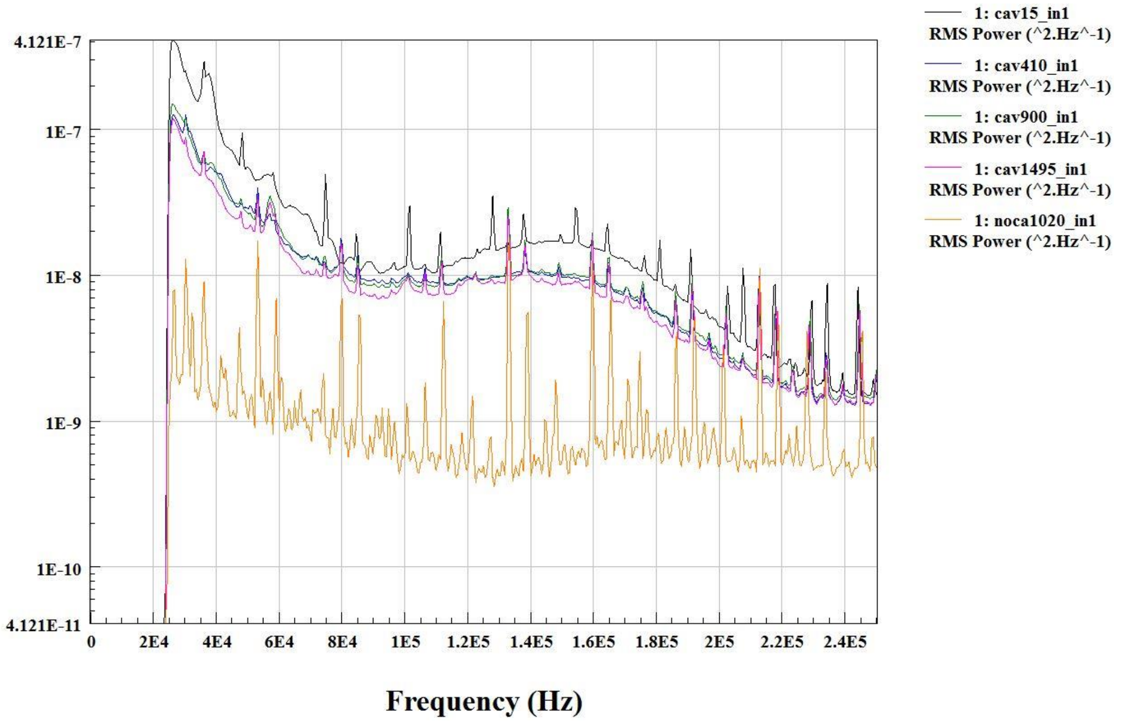

Figure 5.26. *25 kHz high-pass filtered AE signals. y-axis is presented in 10-base logarithmic scale.*

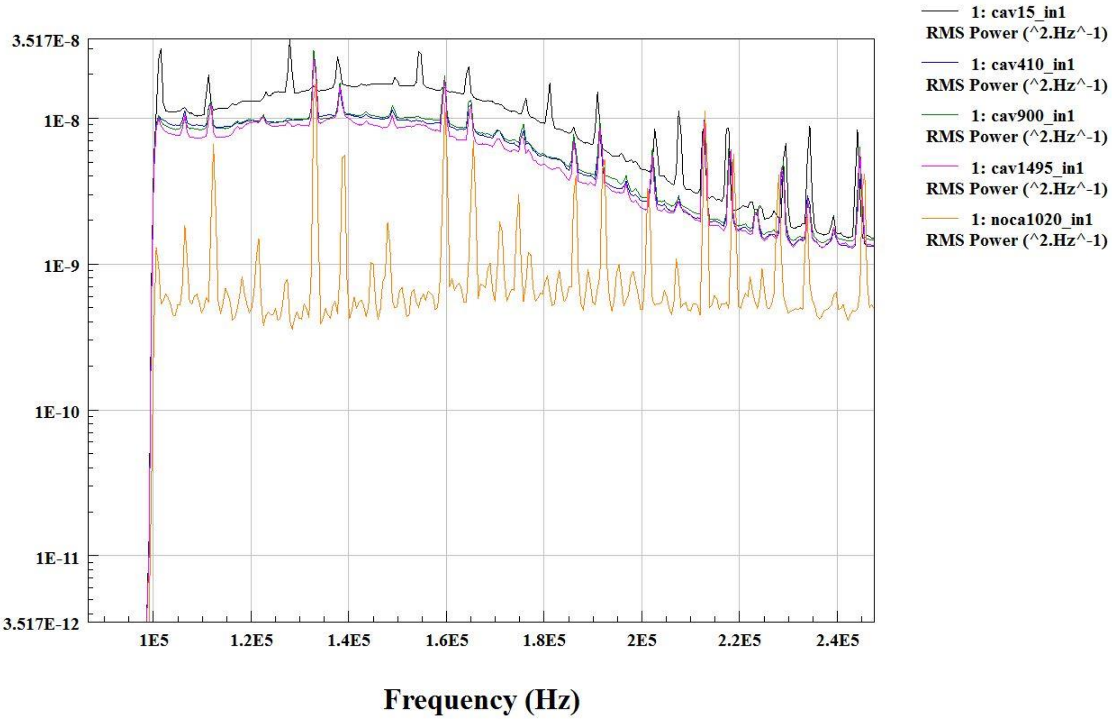

Figure 5.27. *100 kHz high-pass filtered AE signals. y-axis is presented in 10-base logarithmic scale.*

The signal strength in the cavitating region is at least two orders of magnitude higher than the signal strength in the non-cavitating region for lower frequencies. Most of the measured signals were left out from Figures 5.25, 5.26 and 5.27 for clarity. The highest amplitudes are observed in low frequencies. The non-cavitating region signal seems to approach the cavitating region signal in higher frequencies. The difference is still significant as the *y*-axis is logarithmic.

Figures 5.25, 5.26 and 5.27 show that the overall signal strength has a decreasing trend with increasing cumulative erosion time for most of the frequencies measured. The frequency contents for the cumulative erosion time of 15 minutes show some amplitude peaks that are not observable from the other measurements. For example, the amplitude peak at 37 kHz frequency visible in Figure 5.27 is not found in measurements after the incubation period.

With the 100 kHz filter, all the cavitating region signals show quite similar shape, though there are changes at some frequencies. Generally the high amplitude peaks seem to reduce in quantity when the cavitation erosion develops in time. The overall signal root mean square (RMS) value was calculated using a 10 kHz and a 100 kHz filter. The results were plotted with the erosion evolution. The maximum erosion depth was chosen as the parameter of comparison. The maximum erosion depth and the acoustic emission signal RMS-value are presented in Figures 5.28 and 5.29 with the 10 kHz and the 100 kHz filter, respectively.

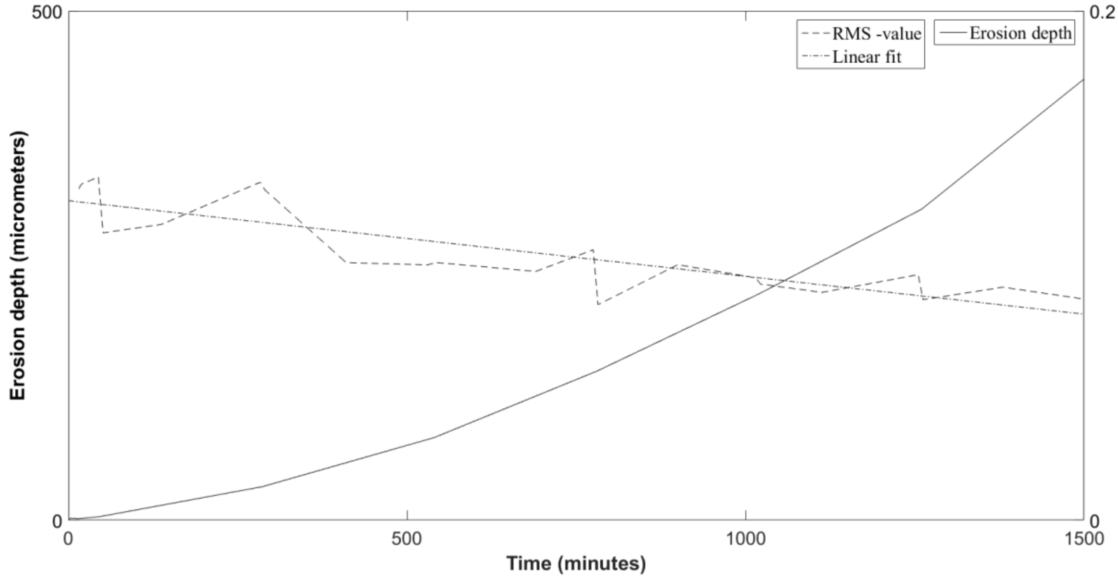

Figure 5.28. *Maximum erosion depth and cavitating region acoustic emission signal RMS-value with 10 kHz filter in function of cumulative erosion time.*

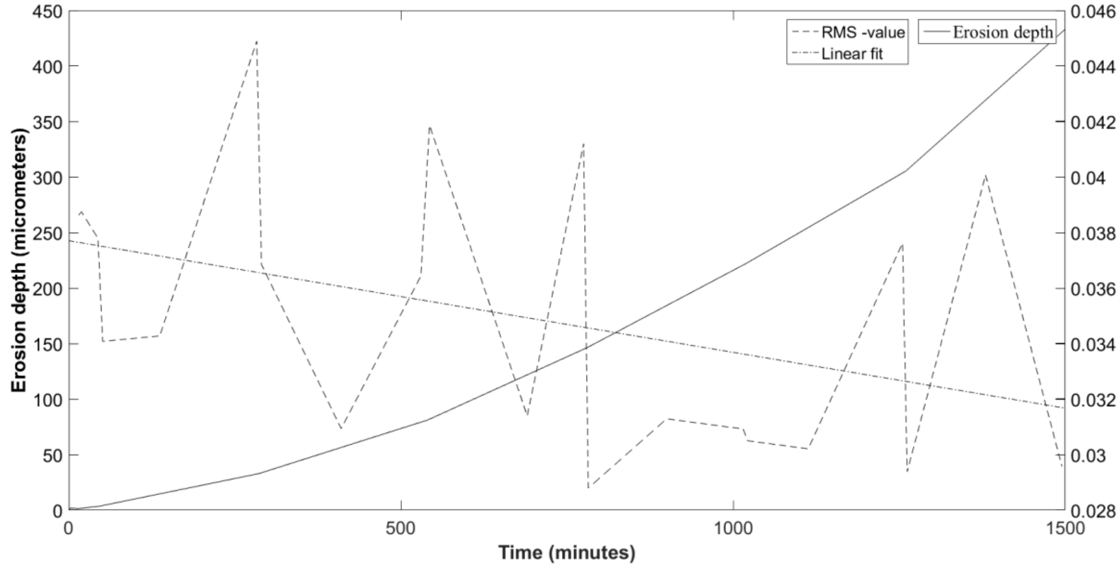

Figure 5.29. *Maximum erosion depth and cavitating region acoustic emission signal RMS-value with 100 kHz filter in function of cumulative erosion time.*

The signal overall RMS-value decreases as the cavitation erosion evolution develops in time. The RMS-value with the 100 kHz filter has a chaotic behaviour, but the overall level still seems to reduce with increasing erosion time. The filtered non-cavitating region signal strength also decreases with time, as seen in Figure 5.31.

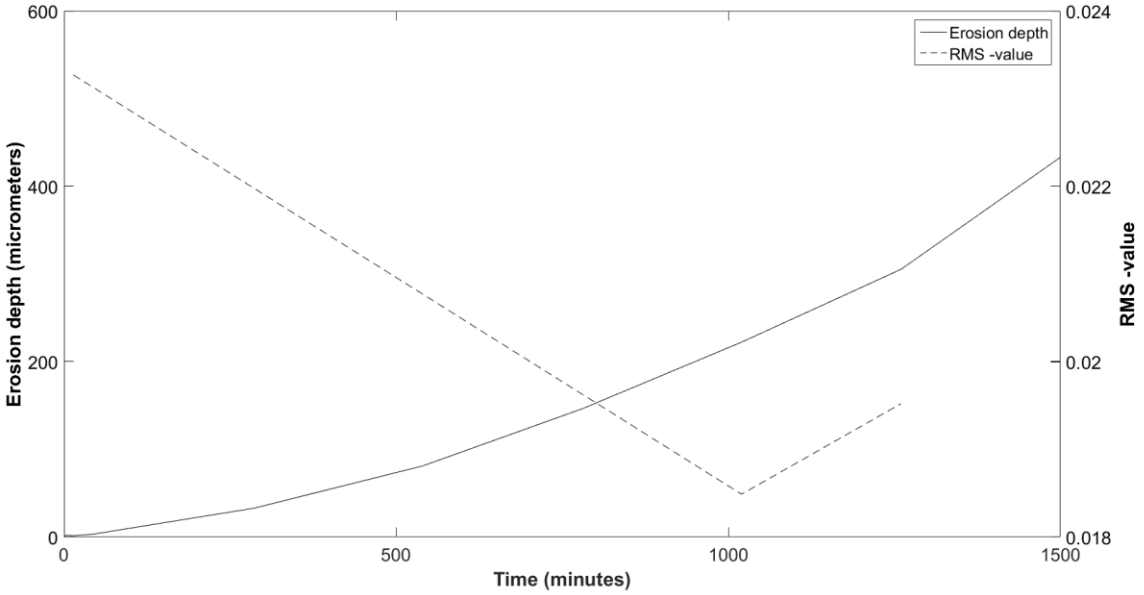

Figure 5.30. *Maximum erosion depth and non-cavitating region acoustic emission signal RMS-value with 10 kHz filter in function of cumulative erosion time.*

The RMS-value in Figure 5.30 has a less chaotic nature than the signals in Figures 5.28 and 5.29 because the non-cavitating region was measured less often than the cavitating region. The 100 kHz filtered signal has a smaller difference in magnitude than the 10 kHz filtered signal, when the cavitating and non-cavitating signals are compared. However, with the 10 kHz filter the cavitating signal RMS-value is at all points about 5 times stronger than that of the non-cavitating signal. For the 100 kHz filter, the factor is about 3. The 100 kHz filtered non-cavitating signal is not presented as it has similar shape as the 10 kHz filtered signal, but a different magnitude.

The reason for the reduction of the signal strength with increasing erosion time may have two reasons: either the signal becomes more damped or the material response of the sample changes with increasing erosion time. The material response and the signal strength could also be linked to the Kaiser effect described in Chapter 3.2. The signal strength reduction is analysed in Chapter 6.3.

6. ANALYSIS

6.1 Erosion evolution and volume loss

In Chapter 6.2.1, the volume losses and erosion depths in function of cumulative erosion time for different materials are presented. In Chapter 6.2.2, the rates of both these two parameters are compared. The cavitation erosion resistances are compared and the materials are classified using the resistance information. The mass loss curves for all the materials could be obtained by multiplying the volume loss curves with respective densities. This was not done, as the volume loss and erosion depth behaviour correspond better to the goals of cavitation erosion research. The erosion research, especially in hydraulic machinery, is focused on the structural qualities of the materials and these qualities are related to geometric parameters, not to the mass.

6.1.1 Volume loss and erosion depth

The volume loss and erosion depth curves for the four comparison materials were plotted similarly as for the steel sample of this study. The comparisons of the volume loss and erosion depth evolutions are presented in Figures 6.1 and 6.2. SS A2205 is stainless steel A2205, SS304L is stainless steel 304L, NAB C95400 is nickel aluminium bronze alloy, ALU 7075 is the aluminium alloy 7075 and SteelAVG is the averaged profile of the Francis turbine runner blade steel in the figures.

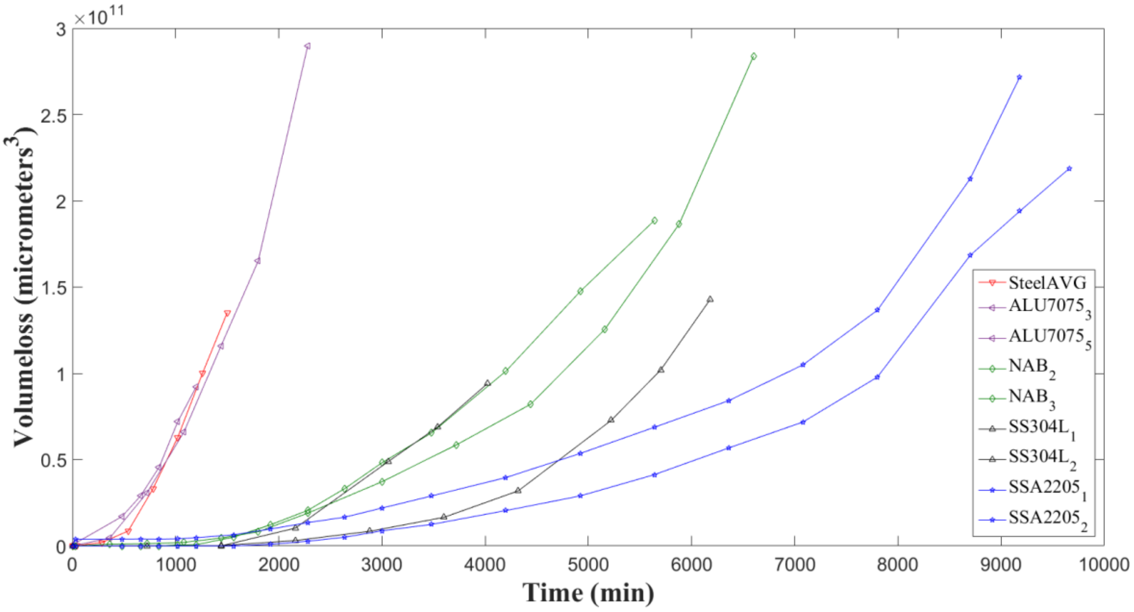

Figure 6.1. *Volume losses of different materials in function of erosion time.*

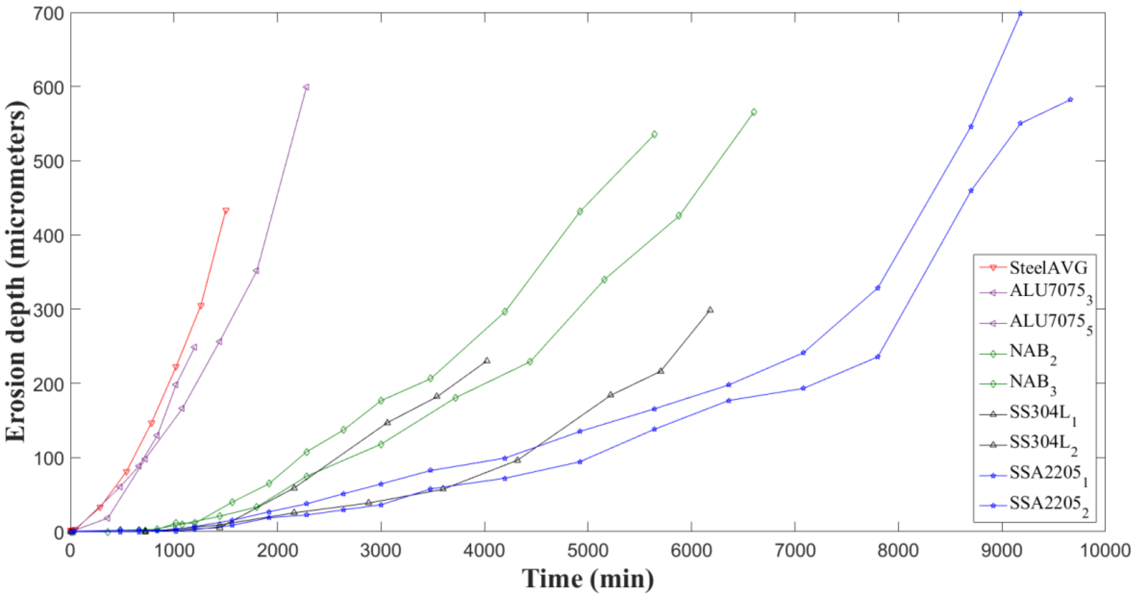

Figure 6.2. *Erosion depths of different materials in function of erosion time.*

In Figures 6.1 and 6.2, the subscripts in the material description correspond to sample numbers. This means that for example, $SS304L_1$ and $SS304L_2$ present the same stainless steel but two different samples. In both figures, a steep curve corresponds to fast erosion of the sample. The volume loss and the erosion depth curves give an idea of the erosion behaviour of the materials. However, the rates for both these parameters are more important in the comparison of the materials. The rates are compared in Chapter 6.2.2.

For other materials than the runner blade steel, two samples are studied. For all four comparison materials, the curves are similar in shape, but they may follow a different path. This is particularly observable for stainless steel 304L. The reason for this behaviour is the difference in the incubation period length. The incubation period length is connected to the work hardening history of the sample surface, as described in Chapter 2.5.1.

The incubation period is not simple to define from the volume loss or the erosion depth curves. In this study, the incubation period was defined as the value of cumulative time when the erosion depth was 25 µm. This value corresponds to a value with which the erosion depth is larger than the pits that are identified as the plastic deformation pits. This definition is not very accurate, but for material comparison, it is sufficient. The pitting tests described in Chapters 2.5.1 and 4.4 would provide a better definition, but for this study, the erosion depth was considered accurate enough. The incubation times with the 25 µm erosion depth definition are listed in Table 6.1.

Table 6.1. *The incubation times of different materials the with 25 µm erosion depth definition.*

Material	**Incubation time (minutes)**
ALU 7075_3	214
Steel	222
ALU 7075_5	390
NAB $C95400_2$	1374
NAB $C95400_3$	1559
SS $304L_2$	1702
SS $A2205_2$	1860
SS $304L_1$	2140
SS $A2205_1$	2270

In Table 6.1, the materials are classified by increasing incubation period length. The incubation time was calculated by a linear interpolation of the erosion depth values around the value of 25 µm. The incubation time of the steel in this study falls into the same category as the incubation times of aluminium alloy 7075. The stainless steel $304L_2$ is in the same order of magnitude as the nickel aluminium bronze alloy. As the shape of the curve for SS $304L_2$ is the same as for SS $304L_1$, it is concluded that the sample number 2 had more initial hardening.

The incubation time analysis shows the relation between the materials tendencies to show observable cavitation damage. The erosion depth of 25 µm is well distinguishable by visual observation if the initial surface has a mirror polishing. A long incubation period means that the material may experience cavitation for a long duration with no significant damage but the work hardening of the material. The erosion rates are used to determine the actual erosion rate when the cavitation erosion is developed further than the incubation period.

6.1.2 Volume loss and erosion depth rates

The volume loss and erosion depth rates are presented in Figures 6.3 and 6.4. The colour coding of the materials is the same as in the figures in Chapter 6.2.1. In both figures, the beginnings of the curves show large values for the rates. This is due to the profilometer errors and short measurement interval in the beginning of the measurements as described in Chapters 5.3.3 and 5.3.4.

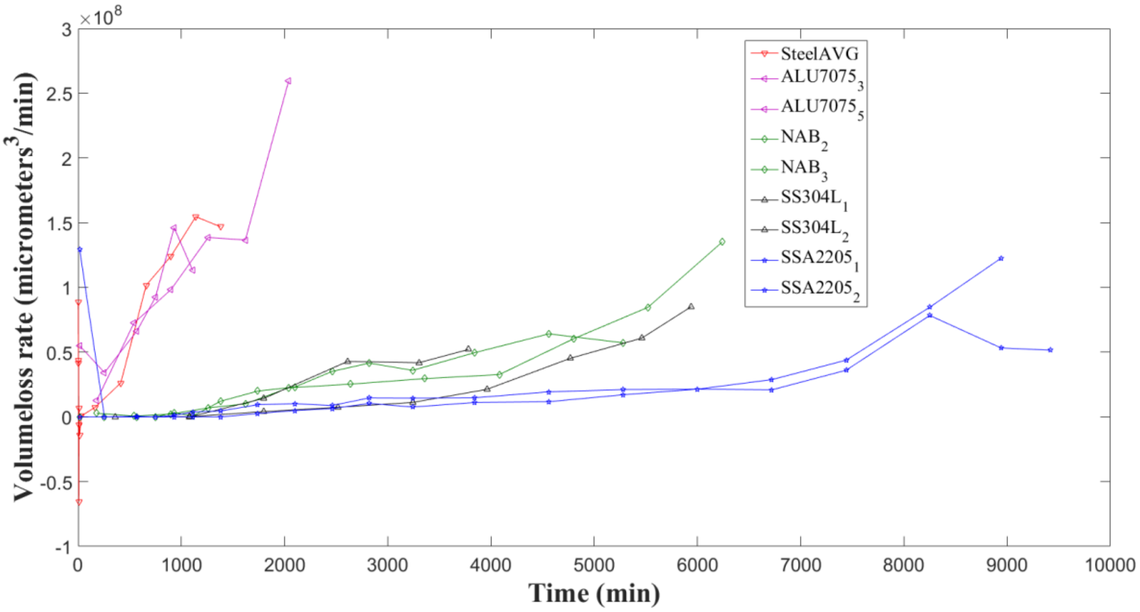

Figure 6.3. *Volume loss rates of different materials in function of erosion time.*

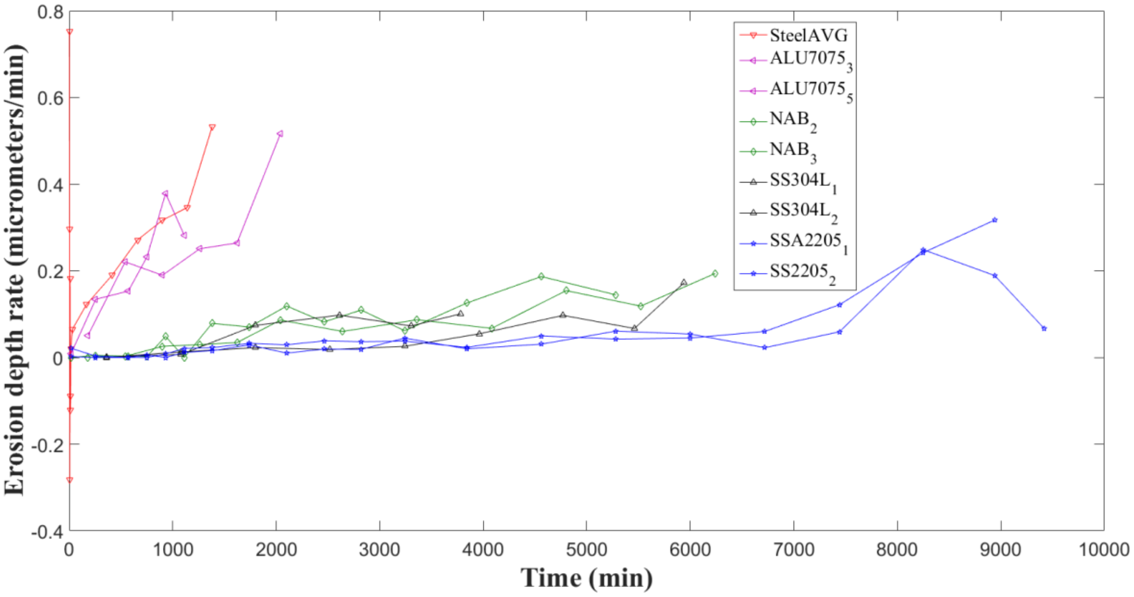

Figure 6.4. *Erosion depth rates of different materials in function of erosion time.*

Both the Figures 6.3 and 6.4 can be used to compare the cavitation erosion resistances of materials. They should correspond to each other fairly well, as faster erosion depth rate means faster volume loss in the zone of maximum erosion. If the erosion depth rate of a material is high in comparison to the other materials, but for the same material the volume loss rate is lower in comparison to the other materials, the material has a steep erosion pit. The materials may have different types of erosion profiles, as there are differences in material responses to cavitation fields of varying intensities.

The final values of the rates are the values that correspond best to the erosion rate of long term cavitation erosion. If cavitation appears in hydraulic machinery, the exposure times are typically long. The developments of the rates in the beginning correspond to the evolution of detectable cavitation erosion of a material surface. A long exposure time before the acceleration of the rates is due to large capability of the material to absorb cavitation impacts.

A large impact absorption capability does not always correspond to low final erosion rate. This is why the cavitation erosion resistance can be classified in two different ways. The first way was to calculate the incubation times of the materials, presented in Chapter 6.2.2. The volume loss rate and the erosion depth rate final values are compared in Table 6.2. The materials are classified by lowering rates of the averaged final values.

Table 6.2. *Materials classified by the final and averaged final volume loss and erosion depth rates.*

Material	**Final volume loss rate (10^6 μm^3/min)**	**Volume loss rate, last 3 values averaged (10^6 μm^3/min)**	**Material**	**Final erosion depth rate (μ/min)**	**Erosion depth rate, last 3 values averaged (μ/min)**
ALU 7075$_5$	259.69	178.3	Steel	0.5325	0.40
Steel	146.88	141.9	ALU 7075$_5$	0.5163	0.34
ALU 7075$_3$	113.16	117.3	ALU 7075$_3$	0.2820	0.30
NAB$_3$	135.18	93.4	SS A2205$_2$	0.3170	0.23
SS A2205$_2$	122.58	83.7	SS A2205$_1$	0.0665	0.17
SS 304L$_1$	85.216	63.8	NAB$_3$	0.1939	0.16
SS A2205$_1$	51.549	61.1	NAB$_2$	0.1445	0.15
NAB$_2$	57.254	57.0	SS 304L$_1$	0.1726	0.11
SS 304L$_2$	52.103	45.6	SS 304L$_2$	0.1005	0.09

The averaged final rates were calculated from the last three values of the rates. This was done for two reasons. The first reason is that the average value indicates if the erosion with each material was in the steady state period or another period. The erosion periods are discussed in Chapters 2.5.1 and 2.5.2. The second reason is that some of the final rate values, such as for ALU 7075$_5$, had large deviation from the previous values. This can either result from measurement error or from large chunks of material removed in a short period.

If the final value for either the volume loss rate or the erosion depth rate is significantly smaller than the average, the erosion should be in its deceleration period. If the value is significantly higher, the erosion should be in its acceleration period. If the values are close to each other, the erosion should be in its steady state period. The erosion rates obtained from this study do not easily fall into the S-shaped curve, as in Figure 2.6 in Chapter 2.5.2.

Cavitation erosion in the PREVERO cavitation tunnel is carried on until the erosion depth is around 0.5 mm. Advancing further with the erosion has a risk that the erosion profile begins to significantly affect the flow field in the test section. For all materials, the steady state period may not be reached. The steady state period also has fluctuations in the erosion rates, as the material is not removed with a constant rate. The erosion may have a relatively long period of small volume loss rate and suddenly the rate may increase as large chunks of material are removed instantly.

Both the volume loss and the erosion depth rates and the incubation time length show that the studied Francis turbine runner blade steel has a similar cavitation erosion resistance as the aluminium alloy 7075 and a much lower cavitation erosion resistance than the nickel aluminium bronze C95400 or the stainless steels A2205 and 304L. In terms of the sample surviving the longest time in the cavitation tunnel, stainless steel A2205 has the highest cavitation erosion resistance. This conclusion alone is not enough, as the total erosion time does not take into account the different definitions of erosion resistance, such as the incubation time and the final erosion rate.

Pure aluminium would probably have worse resistance to cavitation erosion than the aluminium alloy or the runner blade steel. For metals, the mechanical strength corresponds relatively well to the cavitation erosion resistance. The stainless steels in the study have a higher quality in terms of mechanical properties than the runner blade steel. This is one probable reason to their superior resistance. The other possible explanation is the corrosion of the runner blade steel during the cavitation exposure.

The corrosion potential is increased with cavitation, as the cavitation removes the oxidized layer and exposes the pure metal surface to water. Cavitation also increases the oxygen supply near the material surface. This was studied for mild steels by Ryl et al. [113] and by Kwok et al. [114]. They studied the electric potential of the material surface before, during and after cavitation exposure.

Their materials were similar to the runner blade steel in this study, so it can be concluded that corrosion has an effect. The significance of the effect was not studied. According to Ryl et al. [113], the effect is particularly strong in the incubation period. The corrosion could also affect the cavitation field's ability to remove material, as a corroded surface may be less resistant to cavitation impacts than a virgin surface. This effect was not studied.

6.2 Material characteristic comparison

The cavitation erosion resistance of the material in this study was compared to four other materials that have been previously studied in the LEGI laboratory. These four materials are: aluminium alloy 7075, nickel aluminium bronze alloy C95400, stainless steel A2205 and stainless steel 304L. The exact compositions and details of these four materials were not available for this study, but some of the material characteristics are compared in this chapter. The material mechanical properties are listed in Table 6.3.

Table 6.3. *Mechanical properties of compared materials.*

Material	Density (kg/m^3)	Young's modulus (GPa)	Yield stress (MPa)	Source
Steel (test value / literature value)	7800 / 7500 -8080	85 and 179 / 183-213	228 / 110-240	[112]
Aluminium 7075	2810	72	103 – 145	[115]
Nickel aluminium bronze C95400	7450	110	205	[116]
Stainless steel A2205	7820	190	448	[117]
Stainless steel 304L	8000	193 - 200	210	[118]

The literature values for the mechanical properties of the studied steel have large deviations, because the exact composition of the steel was unknown. The values are general values for low alloy steels. For the other materials, the values are also not exact, as the accurate composition and type was unknown. The yield stresses are for low strain rates and the Young's moduli are macroscopic values except the two test values for the studied steel.

Aluminium alloy 7075 has the lowest and stainless steel A2205 the highest yield stresses. A high yield stress seems to correspond to good cavitation erosion resistance, except for the studied runner blade steel. One possible explanation would be that the corrosion interacts with cavitation so much that the erosion resistance of the steel is hindered by it. The yield stress, however, is not the only factor in cavitation erosion. A low yield stress means that the material experiences plastic strain with low stress, so it should have a large effect on the level of cavitation impacts that damage the material. Comparing yield stresses of standard metals may give an insight on the probable cavitation erosion performances.

6.3 Acoustic emission and erosion stages

As the cavitation erosion is developing, the material work hardening level is increasing. The acoustic emission signal strength also decreases when the erosion develops. The cavitation erosion incubation period is dominated by plastic deformation. As the erosion develops, the distance between cavitation impacts and material surface may increase. The surface of the sample becomes coarser and the impact directions may be affected.

The amplitude peaks that are not observed in the advanced stages of cavitation could be used as means to identify the cavitation period as incubation period. However, the origin of the different frequencies was not addressed in this study. To make justified conclusions, more research should be conducted. From the results in this study, it may be observed that most of the signal peaks in the frequency domain change only in amplitude and that there are some peaks in the early stages of erosion that disappear as the erosion develops.

The signal overall strength could decrease because of the increased amount of water between cavitation bubble collapses and the sample material. The maximum erosion depth is about 0.5 mm in the end of the testing procedure and the test section channel width is 2.5 mm. The channel width with the eroded sample is therefore 20 percent larger in the point of maximum erosion depth in the end of the measurements than the width in the beginning of the erosion. A large difference could affect the flow field and it could result to the situation that less bubble collapses happen near the material surface in the end of the tests than in their beginning. The sample surface is also highly uneven in the end of the tests, which could also cause signal attenuation.

The material response to cavitation impulses may also cause differences in the signal strength. The acoustic emission signal from the crack propagation dominated erosion period is different than the acoustic emission signal from the plastic deformation dominated period. It is possible that the cavitation noise is too high to identify this difference in practical measurements. This aspect was not addressed in this study in detail.

The material response and the link to the signal strength may also be connected to the Kaiser effect, described in Chapter 3.2. In the beginning of the erosion, no loadings have been applied to the sample. The cavitation collapses provide short duration loadings that may or may not exceed material deformation limits. This is why the magnitude of acoustic emission could reduce when there are less virgin loadings and more advanced erosion period loadings. A virgin loading may emit more acoustic signal, as acoustic signal is emitted from the full range of the loading. A loading in the advanced erosion periods may only emit acoustic signals in the part where it exceeds the stress limits where plastic deformation or rupture occurs.

The reason why the signal strength reduces with increasing erosion time was not found. It is unlikely that the trend of reducing signal strength would be caused by changes in the measurement setup. For verification, further studies should be made. If the signal strength is verified to always decrease with increasing erosion time, it could be used as means to monitor the stage of cavitation erosion.

The acoustic emission signal was measured with the sampling frequency of 500 kHz, which means that signal frequencies up to 250 kHz could be detected. As described in Chapter 3.2, acoustic emission may be detected up to 1 MHz frequency. The sensor used in this study could measure frequencies up to this value, but the data acquisition unit limited the sampling frequency. This could be avoided by using a unit that would have a sampling rate of 2 MHz’s

7. CONCLUSIONS

One steel type used in Francis turbine runner blades was studied. The material characteristics such as density, elemental composition, Young’s modulus, yield stress and the strain rate dependency were defined. A cylindrical material sample was exposed to cavitation erosion in the PREVERO cavitation tunnel in the LEGI laboratory in Saint Martin d’Hères, France. The sample surface profiles were measured between cavitation erosion periods and the erosion evolution was calculated from the profiles. The erosion evolution was compared to that of other materials. Acoustic emission was measured from the sample during the cavitation erosion testing.

The material characteristics were determined by elemental analysis, by macroscopic compression, by nanoindentation and by split Hopkinson pressure bar tests. The nanoindentation tests showed that the material had two distinct phases in its surface, the other one having a smaller Young’s modulus than the other. The macroscopic compression test combined with the split Hopkinson pressure bar test were used to create an approximation of the strain rate dependency of the stress experienced by the material. The elemental analysis was used to classify the steel quality. The material testing results are summarized in Table 7.1.

Table 7.1. *Summary of the material characterization tests.*

Testing method	**Result**	**Remarks**
Elemental analysis	Sample material is a low alloy steel.	
Density measurement	Material density is 7800 kg/m^3.	
Compression tests	Yield stresses for different strain rates are: 7.795·10-4 1/s: 228 MPa 10-2 1/s: 288 MPa 1 1/s: 346 MPa	Only the value for the strain rate of 7.795·10-4 1/s was used as the others were not considered as reliable.
Nanoindentation tests	Young’s moduli for the two different phases are 85 GPa and 179 GPa.	The values were calculated with the assumption of a perfectly spherical indenter with constant shape, leading to some error.
Split Hopkinson pressure bar tests	The strain rate dependency was: $\sigma = \left(244.99\ MPa + K'\varepsilon_p{}^n\right) \cdot (1 + 0.0102 ln \frac{\dot{\varepsilon}}{1\ \frac{1}{s}})$	The equation is only applicable to the yield stresses with variable strain rates, as the parameters K’ and n were not studied.

The cavitation erosion evolution was measured with a contact profilometer and the profilometer data was used to calculate the volume loss and the maximum erosion depth evolutions. The surface profile was measured along four sample orientations and the volume loss was calculated for all the orientations. There was a large difference in the erosion evolution in the four different orientations. The reason was either sample heterogeneous work hardening history or material composition or possibly the non-axisymmetricity of the cavitation field.

An average was calculated for both the volume loss and the maximum erosion depth evolutions. The averaged erosion evolution curves were compared to equivalent curves from materials previously studied with the PREVERO cavitation tunnel. The previous materials were aluminium alloy 7075 (ALU7075), nickel aluminium bronze alloy C95400 (NAB) and stainless steels (SS) A2205 and 304L. For all the comparison materials, results from two samples were used.

The runner blade steel sample was found to be as resistant to cavitation as the aluminium alloy 7075 and to be much weaker than the nickel aluminium bronze alloy C95400 or the stainless steels. The materials, their mechanical properties and their cavitation erosion characteristics are listed in table 7.2.

Table 7.2. *Summary of the cavitation erosion evolution and the material properties for all materials.*

Material	**Young’s moduli, soft/hard phase (GPa)**	**Yield stress, low/high strain rate (MPa)**	**Incubation period length (minutes)**	**Final volume loss rate, averaged over 3 values (μm^3/min)**	**Final erosion depth rate, averaged over 3 values (μm/min)**
Steel	85 / 179	228 / 259	222	141.9	0.34
ALU7075$_3$			214	117.3	0.30
ALU7075$_5$	72	103-145	390	178.3	0.40
NAB $_2$			1374	57.0	0.11
NAB$_3$	110	205	1559	93.4	0.23
SS A2205$_1$			2270	61.1	0.15
SS A2205$_2$	190	448	1860	83.7	0.17
SS 304L$_1$			2140	63.8	0.16
SS 304L$_2$	193-200	210	1702	45.6	0.09

A high value of incubation period length corresponds to high amount of cavitation impacts absorbed before significant volume loss occurs. The value may be affected by initial work hardening history of a material. A high value of final volume loss rate or erosion depth rate corresponds to fast loss of material in the advanced erosion periods.

The values for both these parameters are similar for the runner blade steel and the aluminium alloy 7075. Nickel aluminium bronze C95400 alloy seems to be weaker than the stainless steel samples in terms of incubation time and the final erosion depth rate, but not in terms of final volume loss rate. High value of yield stress seems to correspond to high cavitation erosion resistance, if the runner blade steel is excluded. Steel sample corrosion is a possible explanation for its weaker resistance. Yield stress is not the only factor in cavitation erosion, so the only conclusion is that it seems to have some correlation with cavitation erosion resistance.

Acoustic emission was measured from the runner blade steel sample when it was subjected to cavitation erosion. Measurements were done throughout the cavitation erosion testing in three one minute intervals during each four hour erosion period. Acoustic emission was also measured several times during the tests with a lower flow velocity in the cavitation tunnel, corresponding to higher cavitation number. With the cavitation number high enough, no cavitation occurred.

The acoustic emission signal was high-pass filtered with frequencies of 10 kHz, 25 kHz and 100 kHz. Acoustic emission signal overall strength reduced with all filters as the cavitation erosion developed. The incubation period signal frequency content had some high amplitude peaks that were not observed in the advanced erosion period signal frequency contents. The largest amplitude peak having this behaviour was in the 37 kHz frequency.

The reduction in the signal strength as the erosion develops may be from two reasons: either the signal damping increases as the sample surface deforms or the sample material response changes as the material work hardening profile develops. The signal damping could be caused by the increased amount of water between the material surface and the cavitation field or by the attenuation of the signal in the increasingly rough surface. The work hardening has an impact on the acoustic emission signal. However, it was not studied if the impact or the change could be significant enough to be observed through the cavitation noise. The difference in the acoustic emission could also be linked to the Kaiser effect.

The corrosion behaviour was not studied, but it could be significant in cavitation erosion. For further research, this could be studied for example by measuring the electric potential of the sample surface. The material was studied with only one sample. A larger amount of samples could be studied with different operating parameters in the PREVERO cavitation tunnel. With different operating parameters, the erosion evolution and the acoustic emission signal could be classified in terms of cavitation field aggressiveness. An optical profilometer would be more accurate in defining the erosion profiles as the contact profilometer proved to be inaccurate with small depth values.

For the acoustic emission measurements, a data acquisition unit with a higher sampling rate should be used to find all possible frequencies that could be used in the erosion stage identification. In this study, the unit had a sampling frequency of 500 kHz and for further study, a unit with 2 MHz sampling frequency is recommended. Acoustic emission from cavitation erosion should be measured with varying operating parameters and using different materials.

The material used in this study was found to have a small resistance to cavitation erosion when compared to stainless steels, which are the option as a turbine material. The difference could be caused by corrosion or by lower quality or by both. Either way, the stainless steels seem to be a better option as a turbine material if cavitation is considered.

Acoustic emission could be used as a method to detect cavitation erosion development. In a running turbine, this would probably require turbine specific analysis to find out the acoustic emission levels in each erosion stage. Some plastic deformation specific frequencies could also be used as indicators, but the source mechanisms need to be studied and more research has to be made to verify the results.

REFERENCES

[1] F. Avellan, Introduction to Cavitation in Hydraulic Machinery, The 6th International Conference on Hydraulic Machinery and Hydrodynamics, .

[2] P. Kumar, R.P. Saini, Study of cavitation in hydro turbines—A review, Renewable and Sustainable Energy Reviews, Vol. 14, No. 1, 2010, pp. 374-383.

[3] P. Bourbon, M. Farhat, R. Simoneau, F. Pereira, P. Dupont, F. Avellan, J.-. Dorey, Cavitation Erosion Prediction on Francis Turbines - Part 1 Measurements on the Prototype, Hydraulic Machinery and Cavitation, 1996, pp. 534-543.

[4] X. Escaler, E. Egusquiza, M. Farhat, F. Avellan, M. Coussirat, Detection of cavitation in hydraulic turbines, Mechanical Systems and Signal Processing, Vol. 20, No. 4, 2006, pp. 983-1007.

[5] Y. Guo, C. Kato, K. Miyagawa, Large-Eddy Simulation of Non-Cavitating and Cavitating Flows in the Draft Tube of a Francis Turbine, Seisan Kenkyu, Vol. 59, No. 1, 2007, pp. 83-88.

[6] J. Franc, Incubation Time and Cavitation Erosion Rate of Work-Hardening Materials, Journal Of Fluids Engineering, Vol. 131, No. 2, 2009, pp. 021303.

[7] J. Franc, M. Riondet, A. Karimi, G.L. Chahine, Material and velocity effects on cavitation erosion pitting, Wear, Vol. 274–275, 2012, pp. 248-259.

[8] S.C. Roy, J. Franc, M. Fivel, Cavitation erosion: Using the material as a pressure sensor, Journal of Applied Physics, Vol. 118, No. 16, 2015, pp. 164905.

[9] S.C. Roy, Modeling and analysis of material behavior during cavitation erosion, Doctoral Thesis, 2015, .

[10] T. Deplancke, O. Lame, J. Cavaille, M. Fivel, M. Riondet, J. Franc, Outstanding cavitation erosion resistance of Ultra High Molecular Weight Polyethylene (UHMWPE) coatings, Wear, Vol. 328–329, 2015, pp. 301-308.

[11] S. Hattori, E. Nakao, Cavitation erosion mechanisms and quantitative evaluation based on erosion particles, Wear, Vol. 249, No. 10–11, 2002, pp. 839-845.

[12] S. Hattori, R. Ishikura, Q. Zhang, Construction of database on cavitation erosion and analyses of carbon steel data, Wear, Vol. 257, No. 9–10, 2004, pp. 1022-1029.

[13] S. Hattori, T. Kitagawa, Analysis of cavitation erosion resistance of cast iron and nonferrous metals based on database and comparison with carbon steel data, Wear, Vol. 269, No. 5–6, 2010, pp. 443-448.

[14] S. Hattori, R. Ishikura, Revision of cavitation erosion database and analysis of stainless steel data, Wear, Vol. 268, No. 1–2, 2010, pp. 109-116.

[15] J. Choi, A. Jayaprakash, G.L. Chahine, Scaling of cavitation erosion progression with cavitation intensity and cavitation source, Wear, Vol. 278–279, 2012, pp. 53-61.

[16] H. Soyama, M. Futakawa, Estimation of Incubation Time of Cavitation Erosion for Various Cavitating Conditions, Tribology Letters, Vol. 17, No. 1, 2004, pp. 27-30.

[17] H. Soyama, Effect of nozzle geometry on a standard cavitation erosion test using a cavitating jet, Wear, Vol. 297, No. 1–2, 2013, pp. 895-902.

[18] A. Karimi, F. Avellan, Comparison of erosion mechanisms in different types of cavitation, Wear, Vol. 113, No. 3, 1986, pp. 305-322.

[19] A. Boorsma, P. Fitzsimmons, Quantification of Cavitation Impacts With Acoustic Emissions Techniques, Proceedings of the 7th International Symposium on Cavitation, .

[20] A. Boorsma, S. Whitworth, Understanding the Details of Cavitation, Second International Symposium on Marine Propulsors, .

[21] H. Schmidt, O. Kirschner, S. Riedelbauch, Cavitation measurements on a pump-turbine model, Journal of Physics: Conference Series, Vol. 656, No. 1, 2015, .

[22] P. Courbiere, Acoustic Method for Characterizing the Onset of Cavitation in Nozzles and Pumps, ASME. Symposium on flow induced vibration, .

[23] H. Yongyong, S. Zaiyang, Experimental Research on Cavitation Erosion Detection Based on Acoustic Emission Technique, 30th European Conference on Acoustic Emission Testing & 7th International Conference on Acoustic Emission, 2012, pp. 1-8.

[24] P.J. Wolff, K.R. Jones, P. March, Evaluation of Results from Acoustic Emissions-Based Cavitation Monitor, Grand Coulee Unit G-24, Cavitation Monitoring System Comparison Tests, Grand Coulee Project, .

[25] A.f. Mills, Basic Heat & Mass Transfer, 2nd ed. Prentice Hall, 1999, .

[26] J. Franc, J. Michel, Fundamentals of Cavitation, 1st ed. Springer Science + Business Media, Inc., 2005, .

[27] C.E. Brennen, Cavitation and Bubble Dynamics, 1st ed. Oxford University Press, 1995, .

[28] P. Dörfler, M. Sick, A. Coutu, Flow-Induced Pulsation and Vibration in Hydroelectric Machinery, 1st ed. Springer-Verlag London, 2013, .

[29] G.L. Chahine, J. Franc, A. Karimi, Cavitation and Cavitation Erosion, in: K. Kim, G.L. Chahine, J. Franc, A. Karimi (ed.), Advanced Experimental and Numerical Techniques for Cavitation Erosion Prediction, Springer Dordrecht Heidelberg, 2014, pp. 3-20.

[30] F.M. White, Fluid Mechanics, 4th ed. McGraw-Hill, 1998, .

[31] Z. Husain, M.Z. Abdullah, Z. Alimuddin, Basic Fluid Mechanics and Hydraulic Machines, BS Publications, Hyderabad, IND, 2008, .

[32] M. Berthelot, Sur quelques phénomènes de dilation forcée de liquides, 1849-1858, .

[33] C.E. Brennen, Cavitation and bubble dynamics, 2014, .

[34] F. Caupin, E. Herbert, Cavitation in water: a review, Comptes Rendus Physique, Vol. 7, No. 9–10, 2006, pp. 1000-1017.

[35] D.M. Heyes, Liquids at positive and negative pressure, physica status solidi (b), Vol. 245, No. 3, 2008, pp. 530-538.

[36] H. Vehkamäki, Classical Nucleation Theory in Multicomponent Systems, 1st ed. Springer Berlin Heidelberg, 2006, .

[37] J.G. Auret, O.F.R.A. Damm, G.J. Wright, F.P.A. Robinson, The influence of water air content on cavitation erosion in distilled water, Tribology International, Vol. 26, No. 6, 1993, pp. 431-433.

[38] ASTM G134-95(2010)e1, Standard Test Method for Erosion of Solid Materials by a Cavitating Liquid Jet, 2010.

[39] G.L. Chahine, J. Franc, A. Karimi, Laboratory Testing Methods of Cavitation Erosion, in: K. Kim, G.L. Chahine, J. Franc, A. Karimi (ed.), 10.1007/978-94-017-8539-6, Springer Dordrecht Heidelberg, 2014, pp. 21-35.

[40] S.G. Zhang, J.H. Duncan, G.L. Chahine, The Final Stage of the Collapse of a Cavitation Bubble Near a Rigid Wall, Journal of Fluid Mechanics, Vol. 257, 1993, pp. 147-181.

[41] E.A. Brujan, G.S. Keen, A. Vogel, J.R. Blake, The final stage of the collapse of a cavitation bubble close to a rigid boundary, Physics of Fluids, Vol. 14, No. 1, 2002, pp. 85.

[42] M.S. Plesset, R.P. Chapman, Collapse of an initially spherical vapour cavity in the neighbourhood of a solid boundary, Journal of Fluid Mechanics, Vol. 47, No. 2, 1971, pp. 283-290.

[43] G.L. Chahine, Collapse of a Cavitating Vortex Ring, Journal Of Fluids Engineering, Vol. 105, No. 4, 1983, pp. 400.

[44] G.L. Chahine, J. Franc, A. Karimi, Mass Loss and Advanced Periods of Erosion, in: K. Kim, G.L. Chahine, J. Franc, A. Karimi (ed.), 10.1007/978-94-017-8539-6, Springer Dordrecht Heidelberg, 2014, pp. 97-121.

[45] J. Steller, A. Krella, J. Koronowicz, W. Janicki, Towards quantitative assessment of material resistance to cavitation erosion, Wear, Vol. 258, No. 1–4, 2005, pp. 604-613.

[46] A. Karimi, J. Franc, Modeling of Material Response, in: K. Kim, G.L. Chahine, J. Franc, A. Karimi (ed.), Advanced Experimental and Numerical Techniques for Cavitation Erosion Prediction, Springer Dordrecht Heidelberg, 2014, pp. 163-181.

[47] P.J. Ferreira, Microstructure development during high-velocity deformation, Metallurgical And Materials Transactions A, Vol. 35, No. 10, 2004, pp. 3091-3101.

[48] K.M. Kalumuck, R. Duraiswami, G.L. Chahine, Bubble Dynamics Fluid-Structure Interaction Simulation by Coupling Fluid Bem and Structural Fem Codes, Journal of Fluids and Structures, Vol. 9, No. 8, 1995, pp. 861-883.

[49] G.L. Chahine, K.M. Kalumuck, The Influence of Structural Deformation on Water Jet Impact Loading, Journal of Fluids and Structures, Vol. 12, No. 1, 1998, pp. 103-121.

[50] G.L. Chahine, Modeling of Cavitation Dynamics and interaction with Material, in: K. Kim, G.L. Chahine, J. Franc, A. Karimi (ed.), Advanced Experimental and Numerical Techniques for Cavitation Erosion Prediction, Springer Dordrecht Heidelberg, 2014, pp. 123-161.

[51] G.L. Chahine, J. Franc, A. Karimi, Cavitation Impulsive Pressures, in: K. Kim, G.L. Chahine, J. Franc, A. Karimi (ed.), 10.1007/978-94-017-8539-6, Springer Dordrecht Heidelberg, 2014, pp. 71-95.

[52] C. Hsiao, G.L. Chahine, Development of Compressible-Incompressible Link to Efficiently Model Bubble Dynamics Near Floating Body Flow Stage Fluid Code Interface Structure Code, Beteq 2013 XIV International Conference on Boundary Element & Meshless Techniquies, .

[53] C. Hsiao, A. Jayaprakash, A. Kapahi, J.-. Choi, G.L. Chahine, Modelling of material pitting from cavitation bubble collapse, Journal of Fluid Mechanics, Vol. 755, 2014, pp. 142-175.

[54] J.-. Choi, G.L. Chahine, Quantitative evaluation of erosive cavitation pressure field from pits in material: fact or myth? 9th International Symposium on Cavitation (CAV2015), pp. 1-4.

[55] T.G. Liu, B.C. Khoo, K.S. Yeo, Ghost fluid method for strong shock impacting on material interface, Journal of Computational Physics, Vol. 190, No. 2, 2003, pp. 651-681.

[56] T.G. Liu, W.F. Xie, B.C. Khoo, The Modified Ghost Fluid Method for Coupling of Fluid and Structure Constituted with Hydro-Elasto-Plastic Equation of State, SIAM Journal on Scientific Computing, Vol. 30, No. 3, 2008, pp. 1105-26.

[57] W.F. Xie, Y.L. Young, T.G. Liu, Multiphase modeling of dynamic fluid?structure interaction during close-in explosion, International Journal for Numerical Methods in Engineering, Vol. 74, No. 6, 2008, pp. 1019-1043.

[58] R.P. Fedkiw, T. Aslam, B. Merriman, S. Osher, A Non-oscillatory Eulerian Approach to Interfaces in Multimaterial Flows (the Ghost Fluid Method), Journal of Computational Physics, Vol. 152, No. 2, 1999, pp. 457-492.

[59] R.P. Fedkiw, T. Aslam, S. Xu, The Ghost Fluid Method for Deflagration and Detonation Discontinuities, Journal of Computational Physics, Vol. 154, No. 2, 1999, pp. 393-427.

[60] S. Zhang, J.H. Duncan, G.L. Chahine, The behavior of a cavitation bubble near a rigid wall, Fluid Mechanics and Its Applications, Vol. 23, 1994, pp. 429-436.

[61] E. Madadi-Kandjani, Q. Xiong, Validity of the spring-backed membrane model for bubble–wall interactions with compliant walls, Computers & Fluids, Vol. 96, 2014, pp. 116-121.

[62] E. Klaseboer, C.K. Turangan, B.C. Khoo, Dynamic behaviour of a bubble near an elastic infinite interface, International Journal of Multiphase Flow, Vol. 32, No. 9, 2006, pp. 1110-1122.

[63] S. Yang, S. Jaw, K. Yeh, Single cavitation bubble generation and observation of the bubble collapse flow induced by a pressure wave, Experiments in Fluids, Vol. 47, No. 2, 2009, pp. 343-355.

[64] S. Yang, S. Jaw, K. Yeh, Cinematographic Analysis of Counter Jet Formation in a Single Cavitation Bubble Collapse Flow, Journal of Mechanics, Vol. 27, No. 2, 2011, pp. 253-266.

[65] H.G. Lee, J. Kim, Two-dimensional Kelvin–Helmholtz instabilities of multi-component fluids, European Journal of Mechanics - B/Fluids, Vol. 49, Part A, 2015, pp. 77-88.

[66] J.W. Grove, R. Holmes, D.H. Sharp, Y. Yang, Q. Zhang, Quantitative theory of Richtmyer-Meshkov instability, Physical Review Letters, Vol. 71, No. 21, 1993, pp. 3473-3476.

[67] R.T. Knapp, J.W. Daily, F.G. Hammitt, Cavitation, McGraw-Hill, 1970, .

[68] F. Pereira, F. Avellan, P. Dupont, Prediction of Cavitation Erosion: An Energy Approach, Journal of Fluids Engineering, Transactions of the ASME, Vol. 120, No. 4, 1998, pp. 719-727.

[69] F.G. Hammitt, Cavitation Erosion: the State of Art and Predicting Capability, University of Michigan, 1979, .

[70] J. Franc, G.L. Chahine, A. Karimi, Pitting and Incubation period, in: K. Kim, G.L. Chahine, J. Franc, A. Karimi (ed.), 10.1007/978-94-017-8539-6, Springer Dordrecht Heidelberg, 2014, pp. 37-69.

[71] A. Karimi, W.R. Leo, Phenomenological model for cavitation erosion rate computation, Materials Science and Engineering, Vol. 95, 1987, pp. 1-14.

[72] N. Berchiche, J.-. Franc, J.-. Michel, A Cavitation Erosion Model for Ductile Materials, .

[73] H. Kleemola J., M.A. Nieminen, On the strain-hardening parameters of metals, Metallurgical Transactions, Vol. 5, No. 8, 1974, pp. 1863-1866.

[74] Y. Zhou, F.G. Hammitt, Cavitation erosion incubation period, Wear, Vol. 86, 1983, pp. 299-313.

[75] G.L. Chahine, Numerical simulation of bubble flow interactions, Journal of Hydrodynamics, Ser.B, Vol. 21, No. 3, 2009, pp. 316-332.

[76] M. Dular, B. Bachert, B. Stoffel, B. Širok, Relationship between cavitation structures and cavitation damage, Wear, Vol. 257, No. 11, 2004, pp. 1176-1184.

[77] Cavitation, Encyclopaedia Britannica Educational Corp., Chicago, 1969, .

[78] J. Leroux, J.A. Astolfi, J.Y. Billard, An Experimental Study of Unsteady Partial Cavitation, Journal of Fluids Engineering, Vol. 126, No. 1, 2004, pp. 94-101.

[79] M. Dreyer, Mind The Gap: Tip Leakage Vortex Dynamics and Cavitation in Axial Turbines, PhD, 2015, .

[80] D. Frunzăverde, S. Muntean, G. Mărginean, V. Câmpian, L. Marşavina, R. Terzi, V. Şerban, Failure analysis of a Francis turbine runner, IOP Conference Series: Earth and Environmental Science, Vol. 12, No. 1, 2010, pp. 1-10.

[81] M. Ohtsu, History and Fundamentals, in: C. Grosse (ed.), Acoustic emission testing, Springer Berlin Heidelberg, 2008, pp. 11-18.

[82] T.F. Drouillard, Introduction to Acoustic Emission Technology, in: R.K. Miller, P. Mcintire (ed.), Nondestructive Testing Handbook Volume 6: Acoustic Emission Testing, 1 ed., ASNT, 1987, pp. 1-10.

[83] H.M. Tensi, The Kaiser-effect and its Scientific Background, Journal of Acoustic Emission, Vol. 22, 2004, .

[84] C. Grosse, Introduction, in: C. Grosse, M. Ohtsu (ed.), Acoustic emission testing, Springer Berlin Heidelberg, 2008, pp. 3-10.

[85] D.E. Bray, R.K. Stanley, Nondestructive Evaluation: A Tool in Design, Manufacturing and Service, CRC Press, 1997, .

[86] K. Máthis, F. Chmelík, Exploring Plastic Deformation of Metallic Materials by the Acoustic Emission Technique, in: W. Sikorski (ed.), Acoustic emission, 1 ed., InTech, 2012, pp. 23-48.

[87] J.C. Spanner, A. Brown, R.D. Hay, V. Mustafa, K. Notvest, A. Pollock, Fundamentals of Acoustic Emission Testing, in: R.K. Miller, P. Mcintire (ed.), Nondestructive Testing Handbook Volume 6: Acoustic Emission Testing, 1 ed., ASNT, 1987, pp. 11-44.

[88] T. Holroyd, Acoustic Emission and Ultrasonics Handbook (Coxmoor's Machine & System Condition Monitoring), Coxmoor Publishing Co., 2000, .

[89] D. Egle, Wave Propagation, in: R.K. Miller, P. Mcintire (ed.), Nondestructive Testing Handbook Volume 6: Acoustic Emission Testing, 1 ed., ASNT, 1987, pp. 1-10.

[90] NDT Resource Center: Wave propagation, web page. Available (accessed 2/22): https://www.nde-ed.org/EducationResources/CommunityCollege/Ultrasonics/Physics/wavepropagation.htm.

[91] J.D. Achenbach, Wave Propagation in Elastic Solids, 1st ed. North Holland Publishing, 1975, .

[92] T. Shiotani, Parameter Analysis, in: C. Grosse (ed.), Acoustic emission testing, Springer Berlin Heidelberg, 2008, pp. 11-18.

[93] NDT Resource Center: AE equipment, web page. Available (accessed 2/22): https://www.nde-ed.org/EducationResources/CommunityCollege/Other%20Methods/AE/AE_Equipment.php.

[94] M. Ohtsu, Sensor and Instrument, in: C. Grosse, M. Ohtsu (ed.), Acoustic emission testing, Springer Berlin Heidelberg, 2008, pp. 19-40.

[95] M.G.R. Sause, Investigation of Pencil-Lead Breaks as Acoustic Emission sources, Journal of Acoustic Emission, 2011, pp. 184-196.

[96] M. Riondet, Disk: "PREVERO" cavitation erosion facility, 2015, .

[97] Instruction Manual for the acoustic emission broadband transducer type 8312, the acoustic emission resonance transducers type 8313 and type 8314 and the acoustic emission preamplifier type 2637, Brüel & Kjær, 1984, .

[98] Brüel & Kjær sensor calibration charts for sensor types 8313 and 8314, .

[99] Fuji Ceramics Corporation product catalog, web page. Available (accessed 2/19): http://www.fujicera.co.jp/product/e/05/07.html.

[100] D. Carnelli, A. Karimi, J. Franc, Application of spherical nanoindentation to determine the pressure of cavitation impacts from pitting tests, Journal of Materials Research, Vol. 27, No. 1, 2012, pp. 91-99.

[101] F. Pöhl, S. Mottyll, R. Skoda, S. Huth, Evaluation of cavitation-induced pressure loads applied to material surfaces by finite-element-assisted pit analysis and numerical investigation of the elasto-plastic deformation of metallic materials, Wear, Vol. 330–331, 2015, pp. 618-628.

[102] M. Fivel, Les effets de taille en nanoindentation : expériences et modélisation à diverses échelles, Proceeding du colloque National de MECAMAT, pp. 63-70.

[103] A.C. Fischer-Cripps, Introduction to Contact Mechanics, 2nd ed. Springer US, 2007, .

[104] G.T. Gray III, Classic Split-Hopkinson Pressure Bar Testing, ASM Handbook, Mechanical Testing and Evaluation, Vol. 8, 2000, pp. 462-476.

[105] X. Wang, C. Huang, B. Zou, H. Liu, H. Zhu, J. Wang, Dynamic behavior and a modified Johnson–Cook constitutive model of Inconel 718 at high strain rate and elevated temperature, Materials Science and Engineering: A, Vol. 580, 2013, pp. 385-390.

[106] T. Okada, Y. Iwai, S. Hattori, N. Tanimura, Relation between impact load and the damage produced by cavitation bubble collapse, Wear, Vol. 184, No. 2, 1995, pp. 231-239.

[107] A. Karabenciov, A.D. Jurchela, I. Bordeasu, M. Popoviciu, N. Birau, A. Lustyan, Considerations Upon the Cavitation Erosion Resistance of Stainless Steel With Variable Chromium and Nickel Content, IOP Conference Series: Earth and Environmental Science, Vol. 12, No. 1, 2010, pp. 1-8.

[108] H. Kendrick, M.S. Light, V. Caccese, Development of a Cavitation Erosion Resistant Advanced Material System, 2005, .

[109] A. Karimi, Cavitation erosion of a duplex stainless steel, Materials Science and Engineering, Vol. 86, 1987, pp. 191-203.

[110] S. Hattori, T. Hirose, K. Sugiyama, Prediction method for cavitation erosion based on measurement of bubble collapse impact loads, Wear, Vol. 269, No. 7–8, 2010, pp. 507-514.

[111] A. Osterman, B. Bachert, B. Sirok, M. Dular, Time dependant measurements of cavitation damage, Wear, Vol. 266, No. 9–10, 2009, pp. 945-951.

[112] Matweb material property data, low alloy steels, web page. Available (accessed 2/18):
http://www.matweb.com/search/DataSheet.aspx?MatGUID=d1bdbccde4da4da4a9dbb8918d783b29&ckck=1.

[113] J. Ryl, K. Darowicki, P. Slepski, Evaluation of cavitation erosion–corrosion degradation of mild steel by means of dynamic impedance spectroscopy in galvanostatic mode, Corrosion Science, Vol. 53, No. 5, 2011, pp. 1873-1879.

[114] C.T. Kwok, F.T. Cheng, H.C. Man, Cavitation erosion and corrosion behaviors of laser-aluminized mild steel, Surface and Coatings Technology, Vol. 200, No. 11, 2006, pp. 3544-3552.

[115] Matweb material property data, aluminum 7075-O, web page. Available (accessed 2/18): http://www.matweb.com/search/DataSheet.aspx?MatGUID=da98aea5e9de44138a7d28782f60a836&ckck=1.

[116] Matweb material property data, aluminum bronze UNS C95400, web page. Available (accessed 2/18): http://www.matweb.com/search/DataSheet.aspx?MatGUID=b950d0d72b5b467689f2d9c5d9030ae8.

[117] Matweb material property data, Stainless steel UNS S32205, web page. Available (accessed 2/18): http://www.matweb.com/search/DataSheet.aspx?MatGUID=086d8b05d09c4963b95253bd278dc4f4.

[118] Matweb material property data, AISI Type 304L Stainless Steel, web page. Available (accessed 2/18): http://www.matweb.com/search/DataSheet.aspx?MatGUID=e2147b8f727343b0b0d51efe02a6127e.

Appendix 1. PREVERO cavitation tunnel measurement log. Page 1/2

N° Test	Date	Psetting	Pup	Dp	Pdown	s	V cav	Q		V mean	Test Duration	Cumulative Duration
		(bars)	(bars)	(bars)	(bars)	(-)	(m/s)	(l/s)	(m^3/h)	(m/s)		
1a	16.11.15	17.36	**22.22**	**3.70**	18.52	**5.005**	66.7	**3.94**	14.18	31.4		
1b	16.11.15	17.36	**40.24**	**21.58**	18.66	**0.865**	89.7	**8.29**	29.84	66.0	2 min	2 min
2a	24.11.15	17.36	**22.27**	**3.70**	18.57	**5.019**	66.7	**3.95**	14.22	31.4		
2b	24.11.15	17.36	**40.32**	**21.60**	18.72	**0.867**	89.8	**8.29**	29.84	66.0	2 min	4 min
3	27.11.15	17.36	**40.24**	**21.55**	18.69	**0.867**	89.7	**8.30**	29.88	66.1	2 min	6 min
4a	04.12.15	17.36	**22.28**	**3.70**	18.58	**5.022**	66.8	**3.96**	14.26	31.5		
4b	04.12.15	17.36	**40.26**	**21.54**	18.72	**0.869**	89.7	**8.33**	29.99	66.3	2 min	8 min
5a	11.01.16	17.36	**22.28**	**3.71**	18.57	**5.005**	66.8	**3.92**	14.11	31.2		
5b	11.01.16	17.36	**40.19**	**21.53**	18.66	**0.867**	89.7	**8.29**	29.84	66.0	2 min	10 min
6a	11.01.16	17.36	**22.31**	**3.71**	18.60	**5.013**	66.8	**3.96**	14.26	31.5		
6b	11.01.16	17.36	**40.23**	**21.54**	18.69	**0.868**	89.7	**8.32**	29.95	66.2	2 min	12 min
7a	20.1.2016	17.36	**22.30**	**3.71**	18.59	**5.011**	66.8	**3.98**	14.33	31.7		
7b	20.1.2016	17.36	**40.28**	**21.60**	18.68	**0.865**	89.8	**8.32**	29.95	66.2	2 min	14 min
7c	20.1.2016	17.36	**22.26**	**3.70**	18.56	**5.016**	66.7	**3.96**	14.26	31.5		
7d	20.1.2016	17.36	**40.18**	**21.53**	18.65	**0.866**	89.6	**8.31**	29.92	66.1	2 min	16 min
8	25.1.2016	17.36	**40.26**	**21.58**	18.68	**0.866**	89.7	**8.30**	29.88	66.1	30 min	46 min
9	26.1.2016	17.36	**40.16**	**21.52**	18.64	**0.866**	89.6	**8.31**	29.92	66.1	240 min	286 min
10	27.1.2016	17.36	**40.12**	**21.52**	18.60	**0.864**	89.6	**8.28**	29.81	65.9	254 min	540 min
11	28.1.2016	17.36	**40.12**	**21.50**	18.62	**0.866**	89.6	**8.26**	29.74	65.7	240 min	780 min
12	1.2.2016	17.36	**40.15**	**21.51**	18.64	**0.867**	89.6	**8.29**	29.84	66.0	240 min	1020 min
13a	2.2.2016	17.36	**22.21**	**3.69**	18.52	**5.019**	66.6	**3.96**	14.26	31.5		
13b	2.2.2016	17.36	**40.15**	**21.49**	18.66	**0.868**	89.6	**8.28**	29.81	65.9	240 min	1260 min
14a	3.2.2016	17.36	**22.21**	**3.69**	18.52	**5.019**	66.6	**3.95**	14.22	31.4	240 min	1500 min
14b	3.2.2016	17.36	**40.15**	**21.49**	18.66	**0.868**	89.6	**8.31**	29.92	66.1	240 min	1500 min

Appendix 1. PREVERO cavitation tunnel measurement log. Page 2/2

N° Test	Tstart (°C)	Tend (°C)	Pot.	Comments
1a	19.1	19.1	**3.00**	Non-cavitating region. Acoustic emission sensor: Brüel & Kjær 8313
1b	19.4	19.6	**7.10**	Cavitating region. Acoustic emission sensor: Brüel & Kjær 8313
2a	17.3	17.3	**3.00**	Non-cavitating region. Acoustic emission sensor: Fujicera 1045S
2b	17.3	18.4	**7.10**	Cavitating region. Acoustic emission sensor: Fujicera 1045S
3	18.2	18.4	**7.10**	Cavitating region. Acoustic emission sensor: Fujicera 1045S
4a	17.2	17.2	**3.00**	Non-cavitating region. Acoustic emission sensor: Fujicera 1045S, external resistance 18 kohm
4b	17.4	18.1	**7.10**	Cavitating region. Acoustic emission sensor: Fujicera 1045S, external resistance 18 kohm
5a	16.8	16.3	**3.00**	Non-cavitating region. Acoustic emission sensor: Fujicera 1045S, external resistance 67 kohm
5b	16.7	16.9	**7.10**	Cavitating region. Acoustic emission sensor: Fujicera 1045S, external resistance 67 kohm
6a	16.8	16.5	**3.00**	Non-cavitating region. Acoustic emission sensor: Fujicera 1045S, external resistance 118 kohm
6b	16.7	17.4	**7.10**	Cavitating region. Acoustic emission sensor: Fujicera 1045S, external resistance 118 kohm
7a	16.6	16.4	**3.00**	Non-cavitating region. Acoustic emission sensor: Fujicera 1045S, external resistance 550 kohm
7b	16.3	17.0	**7.10**	Cavitating region. Acoustic emission sensor: Fujicera 1045S, external resistance 550 kohm
7c	16.6	16.6	**3.00**	Non-cavitating region. Acoustic emission sensor: Fujicera 1045S. Test of another preamplifier.
7d	17.0	17.1	**7.10**	Cavitating region. Acoustic emission sensor: Fujicera 1045S. Test of another preamplifier.
8	18.6	21.7	**7.10**	Cavitating region. Acoustic emission sensor: Fujicera 1045S, external resistance 550 kohm
9	19.9	24.3	**7.10**	Cavitating region. Acoustic emission sensor: Fujicera 1045S, external resistance 550 kohm
10	22.2	25.1	**7.10**	Cavitating region. Acoustic emission sensor: Fujicera 1045S, external resistance 550 kohm
11	22.6	25.9	**7.10**	Cavitating region. Acoustic emission sensor: Fujicera 1045S, external resistance 550 kohm
12	21.7	26.3	**7.10**	Cavitating region. Acoustic emission sensor: Fujicera 1045S, external resistance 550 kohm
13a	23.1	23.1	**3.00**	Non-cavitating region. Acoustic emission sensor: Fujicera 1045S, external resistance 550 kohm
13b	23.4	27.1	**7.10**	Cavitating region. Acoustic emission sensor: Fujicera 1045S, external resistance 550 kohm
14a	23.7	23.7	**3.00**	Non-cavitating region. Acoustic emission sensor: Fujicera 1045S, external resistance 550 kohm
14b	24.2	27.7	**7.10**	Cavitating region. Acoustic emission sensor: Fujicera 1045S, external resistance 550 kohm